

COSMOLOGICAL IMPLICATIONS OF LOW SURFACE BRIGHTNESS
GALAXIES

by
David Sprayberry

A Dissertation Submitted to the Faculty of the
DEPARTMENT OF ASTRONOMY
In Partial Fulfillment of the Requirements
For the Degree of
DOCTOR OF PHILOSOPHY
In the Graduate College
THE UNIVERSITY OF ARIZONA

1 9 9 4

INFORMATION TO USERS

This manuscript has been reproduced from the microfilm master. UMI films the text directly from the original or copy submitted. Thus, some thesis and dissertation copies are in typewriter face, while others may be from any type of computer printer.

The quality of this reproduction is dependent upon the quality of the copy submitted. Broken or indistinct print, colored or poor quality illustrations and photographs, print bleedthrough, substandard margins, and improper alignment can adversely affect reproduction.

In the unlikely event that the author did not send UMI a complete manuscript and there are missing pages, these will be noted. Also, if unauthorized copyright material had to be removed, a note will indicate the deletion.

Oversize materials (e.g., maps, drawings, charts) are reproduced by sectioning the original, beginning at the upper left-hand corner and continuing from left to right in equal sections with small overlaps. Each original is also photographed in one exposure and is included in reduced form at the back of the book.

Photographs included in the original manuscript have been reproduced xerographically in this copy. Higher quality 6" x 9" black and white photographic prints are available for any photographs or illustrations appearing in this copy for an additional charge. Contact UMI directly to order.

UMI

A Bell & Howell Information Company
300 North Zeeb Road, Ann Arbor, MI 48106-1346 USA
313/761-4700 800/521-0600

COSMOLOGICAL IMPLICATIONS OF LOW SURFACE BRIGHTNESS
GALAXIES

by
David Sprayberry

A Dissertation Submitted to the Faculty of the
DEPARTMENT OF ASTRONOMY
In Partial Fulfillment of the Requirements
For the Degree of
DOCTOR OF PHILOSOPHY
In the Graduate College
THE UNIVERSITY OF ARIZONA

1 9 9 4

UMI Number: 9527985

UMI Microform 9527985

Copyright 1995, by UMI Company. All rights reserved.

This microform edition is protected against unauthorized
copying under Title 17, United States Code.

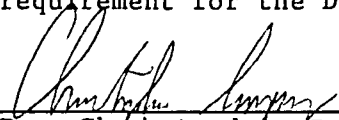
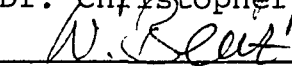
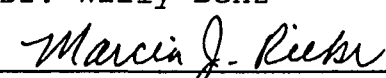
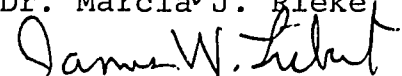
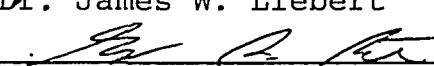
UMI

300 North Zeeb Road
Ann Arbor, MI 48103

THE UNIVERSITY OF ARIZONA
GRADUATE COLLEGE

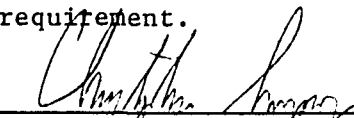
As members of the Final Examination Committee, we certify that we have
read the dissertation prepared by David Sprayberry
entitled Cosmological Implications of Low Surface Brightness
Galaxies

and recommend that it be accepted as fulfilling the dissertation
requirement for the Degree of Doctor of Philosophy

 _____ Dr. Christopher D. Impey	<u>11/4/94</u> _____ Date
 _____ Dr. Willy Benz	<u>11/4/94</u> _____ Date
 _____ Dr. Marcia J. Rieke	<u>11/4/94</u> _____ Date
 _____ Dr. James W. Liebert	<u>11/14/94</u> _____ Date
 _____ Dr. Gregory D. Bothun	<u>11/4/94</u> _____ Date

Final approval and acceptance of this dissertation is contingent upon
the candidate's submission of the final copy of the dissertation to the
Graduate College.

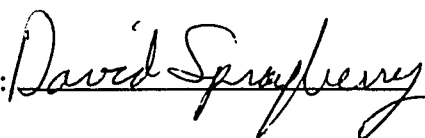
I hereby certify that I have read this dissertation prepared under my
direction and recommend that it be accepted as fulfilling the dissertation
requirement.

 _____ Dissertation Director	<u>11/4/94</u> _____ Date
Dr. Christopher D. Impey	

STATEMENT BY AUTHOR

This dissertation has been submitted in partial fulfillment of requirements for an advanced degree at The University of Arizona and is deposited in the University Library to be made available to borrowers under rules of the Library.

Brief quotations from this dissertation are allowable without special permission, provided that accurate acknowledgment of source is made. Requests for permission for extended quotation from or reproduction of this manuscript in whole or in part may be granted by the head of the major department or the Dean of the Graduate College when in his or her judgment the proposed use of the material is in the interests of scholarship. In all other instances, however, permission must be obtained from the author.

SIGNED: 

ACKNOWLEDGMENTS

So many people to thank, so little time. First and most obviously, I am deeply grateful to all my collaborators: Chris Impey, my advisor, for starting me on an interesting project, and for providing the resources to carry it out; Mike Irwin for his endless patience in helping me with so many of the details of the survey; Greg Bothun for sharing the insight and experience to put all this into some larger perspective; and Gary Bernstein for his particular help with the Tully-Fisher chapter and helpful comments on other aspects of science and life.

Second, I thank all the scientific and technical support staffs at the Multiple Mirror Telescope, the Steward Observatory Kitt Peak Station, and the Arecibo Observatory for their tireless help with the data collection. There is an awful lot of data needed for a survey like this one, and not one photon of it would have been worth a damn without the help of a lot of talented people. There are way too many of them to name individually, but special thanks are due to Craig Foltz of the MMT for continuing help with my questions about instruments, observing procedures, and broad science matters, and to JoAnn Eder of Arecibo for guidance that ensured productive runs there.

Third, I am indebted to all my fellow graduate students at Steward. They've all taught me a lot about a lot of things, and in doing so made the last five years immensely more fun. Special thanks are due to: Doug Williams, my office mate, for his infinite patience, good humor and store of Unix wisdom; Kim McLeod for her \LaTeX macros, which made formatting this beast almost painless; Brian McLeod for invaluable help with the first Arecibo run and for an early copy of his thesis; Tim Pickering for help with SM and other fun programs; and to future Steward professor Hans-Walter Rix for unlimited scientific advice, coffee chat, good times, and great hikes (despite the lost toenails). Thanks also go to Cathy Petry and Katy Flint for helping me navigate the NASA ADS.

Finally, I owe more thanks than words can express to Sonja Petersen, my lady wife. Her love and support have kept me alive and moving throughout the long pull to get this thesis done. It is with deep and abiding love that I dedicate this work to her.

Contents

LIST OF FIGURES	8
LIST OF TABLES	10
ABSTRACT	11
1 INTRODUCTION	13
1.1 Selection Effects in Galaxy Surveys	14
1.2 Motivations for the Present Work	20
2 SELECTION EFFECTS AND COMPLETENESS OF THE APM SURVEY	24
2.1 Introduction	25
2.2 The Selection Process	27
2.3 Photometric Calibration	30
2.4 Completeness	37
2.5 Implications	43
2.6 Conclusions	47
3 LOW SURFACE BRIGHTNESS GALAXIES AND THE FIELD GALAXY LUMINOSITY FUNCTION	48
3.1 Introduction	49
3.2 Samples Used	51
3.3 Methods	59
3.4 Results	66

3.4.1	Effects of the Corrections	66
3.4.2	Comparisons with Other Studies	68
3.4.3	Number and Luminosity Density of LSB Galaxies	74
3.4.4	Luminosity Functions by Morphological Type	79
3.5	Implications	82
3.5.1	Faint Galaxies	82
3.5.2	Bright Galaxies	86
3.6	Conclusions	87
4	THE MASS-TO-LIGHT RATIOS OF FIELD LOW SURFACE BRIGHTNESS SPIRAL GALAXIES: CLUES FROM THE TULLY-FISHER RELATION	89
4.1	Introduction	90
4.2	Data Reduction And Analysis	92
4.2.1	Galaxy Selection and Data Reduction	92
4.2.2	Selection of HSB Comparison Sets	95
4.3	Comparison Of Tully-Fisher Relations	100
4.3.1	Luminosity—Profile Width Correlations	100
4.3.2	Slopes of the Luminosity—Profile Width Relations	102
4.3.3	Scatter in the LSB Luminosity — Profile Width Relation . . .	106
4.4	Discussion	108
4.4.1	Intrinsic Scatter and Half-Light Radius	109
4.4.2	Intrinsic Scatter and Galaxy Evolution	112
4.5	Conclusions	118
5	PROPERTIES OF THE CLASS OF GIANT LOW SURFACE BRIGHTNESS SPIRAL GALAXIES	120
5.1	Introduction	121
5.2	Discovery and Selection	123

5.3	Photometric Properties	125
5.3.1	Observations and Data Reduction	125
5.3.2	Disk and Bulge Parameters	126
5.3.3	Colors	137
5.4	Neutral Hydrogen Properties	141
5.5	Spectroscopic Properties	144
5.5.1	Emission Lines and Active Nuclei	145
5.5.2	Absorption Lines and Metallicities	149
5.6	Small Scale Environments	152
5.6.1	Qualitative Commentary	153
5.6.2	Quantitative Measures of Isolation	156
5.7	Conclusion	159
6	CONCLUSIONS AND FUTURE WORK	161
6.1	Summary of Findings	161
6.2	Some Ideas for Further Investigations	164
A	GALAXIES FROM THE LSB SURVEY: BASIC DATA	169

List of Figures

1.1	Apparent radius versus central surface brightness	17
2.1	Sample characteristic curves for individual APM scans	34
2.2	Average characteristic curves for representative UKST plates	35
2.3	APM completeness as a function of galaxy parameters	41
2.4	Distribution of large galaxy central surface brightnesses	44
3.1	Structural properties of complete LSB sample and subset with velocities	53
3.2	Distribution of absolute magnitudes	55
3.3	Distribution of galaxy velocities	57
3.4	Luminosity functions for LSB galaxies with and without completeness corrections	66
3.5	Luminosity functions for LSB galaxies without and with magnitude corrections	68
3.6	Luminosity functions for LSB, ZCAT and Combined samples	69
3.7	Error contours for Schechter parameters	71
3.8	Luminosity functions plotted linearly against $\text{Log } L$	74
3.9	Cumulative luminosity functions plotted linearly against $\text{Log } L$	75
3.10	Luminosity densities plotted linearly against $\text{Log } L$	77
3.11	Cumulative luminosity densities plotted linearly against $\text{Log } L$	78
3.12	Luminosity functions for LSB galaxies by morphological type	80
3.13	Comparison of luminosity functions for irregular galaxies	85

4.1	TF relations for LSB and UMa galaxies	100
4.2	TF relations for LSB and Coma galaxies	102
4.3	TF residuals versus half-light radius	109
4.4	TF residuals versus gas richness	112
4.5	Log M_{HI} versus profile width	114
4.6	TF residuals versus total color	116
4.7	$B-R$ color versus H I profile width	118
5.1	Grayscale reproductions of B CCD images of giant LSB spirals	127
5.2	Radial surface brightness profiles for giant LSB spirals	130
5.3	Central surface brightness versus scale length	134
5.4	$B-V$ color vs diffuseness index	139
5.5	HI profiles of 3 giant LSB spirals	143
5.6	B luminosity versus total gas mass	144
5.7	Optical spectra of giant LSB spirals	146
5.8	Mg_b index versus bulge absolute magnitude	151
5.9	CN 39 index versus Mg_b index	152

List of Tables

2.1	UKST Fields: Photometric Calibrations	32
3.1	Effects of Completeness and Magnitude Corrections	67
3.2	Luminosity Functions for LSB, ZCAT and Combined Samples	70
3.3	Integrated Number and Luminosity Densities	76
3.4	Luminosity Functions for LSB Galaxies by Morphology	81
4.1	Low Surface Brightness Galaxies Used For Tully-Fisher Analysis . .	96
4.2	Tully–Fisher Correlation Coefficients	101
4.3	Tully-Fisher Fit Parameters	104
4.4	M_{HI} vs Log W Fit Parameters	115
5.1	Giant LSB Disk Galaxies	124
5.2	Disk Model Parameters	132
5.3	Bulge Model Parameters	132
5.4	Giant LSB Spiral Galaxies From Other Studies	136
5.5	Average Colors and Surface Brightness Parameters	138
5.6	HI Properties of Giant LSB Disk Galaxies	142
5.7	Emission Line Equivalent Widths and Fluxes	148
5.8	Absorption Line Equivalent Widths and Indices	150
5.9	Average Number of Neighbors	158
A.1	Basic Data for APM Survey Galaxies	172

ABSTRACT

This dissertation briefly presents the results of a survey for galaxies that have been overlooked by previous surveys because their surface brightness, or brightness per unit area on the night sky, is too low. This dissertation they makes use of the survey results to estimate the density of these galaxies and to delineate some of their properties.

Chapter 1 describes the selection bias against finding galaxies of low surface brightness and outlines the importance of these galaxies for a more complete knowledge of the true local galaxy population.

Chapter 2 discusses the techniques employed for identifying low surface brightness (LSB) galaxies for the survey, calibrating the photometry, and estimating the survey incompleteness as a function of galaxy parameters.

Chapter 3 presents luminosity functions for the low surface brightness galaxies identified in the present survey, and for a combined sample of low surface brightness and high surface brightness galaxies. The overall space density of low surface brightness galaxies is about one-fourth to one-third as great as the density determined from standard field galaxy luminosity functions, and that the total luminosity density due to these low surface brightness galaxies is about one-third to one-half the level derived from other surveys.

Chapter 4 presents 21 cm profiles and CCD surface photometry for a subset of the low surface brightness spiral galaxies found by the survey. The general trend of the LSB galaxies in the Tully-Fisher relation, relative to the trend of higher surface brightness galaxies, forms the basis of the conclusion that LSB spirals generally have mass-to-light ratios comparable to that of higher surface brightness spirals but with

a much larger scatter. Various possible reasons for the higher scatter are explored.

Chapter 5 presents CCD surface photometry and optical spectroscopy for a sample of eight low surface brightness spiral galaxies that are extraordinary because of their large physical sizes and high total luminosities. The properties of these galaxies are analyzed and compared to those of more normal spirals.

Chapter 6 summarizes the findings of the preceding chapters and presents some ideas for future investigations.

Chapter 1

INTRODUCTION

Almost 70 years ago Edwin Hubble estimated distances to the nearby “spiral nebulae” NGC 6822 and M 33 by measuring the apparent magnitudes and periods of Cepheid variables in those systems, thus demonstrating that these “spiral nebulae” were independent galaxies at great distances from our own Milky Way (Hubble 1925 and Hubble 1926). With this result, the science of observational cosmology was born. Galaxies were now seen as the basic building blocks of the universe. Hubble recognized the importance of understanding the formation and evolution of galaxies and proposed his famous classification sequence based on galactic appearance as a first step towards bringing order to the “realm of the nebulae.” Unfortunately, later generations of astronomers have had difficulty translating Hubble’s morphological sequence into a more quantitative understanding of the population of galaxies. While a few galactic properties such as total gas content (Roberts 1975) have been found to correlate roughly with morphological type, other quantifiable measures such as gas richness (M_{HI}/L_B) and color have not (Bothun 1982). A recent review by Roberts & Haynes (1994) concluded that, although later Hubble types are generally associated with physical indications of increasing star formation activity, for any

given parameter and any given Hubble type the range of parameter values is much broader than even pessimistic estimates of the measurement uncertainties.

To complicate matters further, the galaxy archetypes defined by the Hubble sequence are based solely a few prominent nearby galaxies and so may not be representative of the full range of galaxy properties. As the study of galaxies has expanded, so has the need for a broader vocabulary with which to describe the subjects. de Vaucouleurs (1959) extended the Hubble sequence to include various classes of irregular objects and introduced sub-classifications of the spiral classes to describe ring and S-shaped features. Further additional classes have been needed to cover the “peculiar” galaxies of Arp (1966), the dwarf elliptical and dwarf irregular galaxies first cataloged in the RC2 by de Vaucouleurs et al. (1976), and others recently summarized by Buta (1990).

1.1 Selection Effects in Galaxy Surveys

With this expansion of the extragalactic bestiary has come the recognition that the properties of the galaxies one sees depend in part on how one looks for them, and on how hard one looks. The light from galaxies is spread out upon the foreground of the night sky, which itself has an emissivity that varies with wavelength, time, location on the sky, and location of the observatory on the Earth. All of these issues, together with the characteristics of the detection system, will conspire to determine which galaxies will be detected and what their measured properties will be. Disney (1980) put it best: “We are like prisoners in a lighted cell trying to discern our whereabouts by peering out through a small casement into the darkness outside. We can see the street lamps easily enough, and the lighted windows, but can we see,

or correctly infer, the houses and the trees?”

Arp (1965), describing the discovery of a small, condensed galaxy that was almost indistinguishable from a star, noted that the known galaxies fill a narrow band in the absolute magnitude–log diameter plane. Because some galaxies such as the Local Group dwarf spheroidals fall outside this band (they are known only because their individual stars can be seen), he speculated that perhaps this was a selection effect due to surface brightness, and that perhaps the true population of galaxies filled a much broader region of the parameter space. Disney (1976) first quantified the possible effects of this illuminated foreground on the selection of galaxies for study. Most galaxy surface luminosity distributions can be fairly well described as

$$I(r) = I_0 e^{-(r/\alpha)^{1/\beta}} \quad (1.1)$$

with $\beta = 1$ for disk (*i.e.*, exponential profile) galaxies and $\beta = 4$ for elliptical (*i.e.*, $r^{1/4}$ profile) galaxies. Images have some limiting surface luminosity I_{lim} for the detection of a diffuse signal, which is determined by the sky brightness and the noise and flatfielding characteristics of the detector. Converting the surface luminosities to the more common surface brightnesses as $\mu = -2.5 \log I$ allows Equation 1.1 to be rewritten as

$$\mu_{lim} - \mu_0 = 1.086 \left(\frac{r_{app}}{\alpha} \right)^{1/\beta} \quad (1.2)$$

where r_{app} is the apparent radius of a galaxy with central surface brightness μ_0 in mag arcsec^{-2} as seen on an image with limiting surface brightness μ_{lim} . Integrating Equation 1.1 to infinity and using the resulting total luminosity to substitute for α yields the following expression for the apparent diameter of a galaxy of fixed total luminosity, as a function of central surface brightness:

$$r_{app} \propto 0.4 \ln 10 (\mu_{lim} - \mu_0)^\beta e^{0.46\mu_0} \quad (1.3)$$

which is Equation 4 of Disney (1976). Galaxy surveys will identify those objects which have the largest apparent sizes in the images used. For a given image, the surface brightness limit μ_{lim} is fixed, so at a given galaxy luminosity the apparent size will be determined largely by the central surface brightness μ_0 . Figure 1.1 presents Equation 1.3 graphically, showing there is a peak in apparent size for each profile type. Apparent size falls off rapidly for galaxies with μ_0 fainter than the value at the maximum, implying that a great many of these galaxies will be missed by the surveys. Galaxies with $\mu_0 > \mu_{lim}$ will of course never be detected. Thus, in order to have a more representative sampling of the true population of galaxies, it is necessary to locate and measure galaxies that have been missed by other studies because their surface brightnesses are outside the narrow range that gives maximum apparent size.

The first attempts to redress this selection bias came a few years later. Longmore et al. (1982) identified a sample of 151 low surface brightness (LSB) galaxies from visual inspection of United Kingdom Schmidt Telescope (UKST) survey plates. They conducted followup observations at optical and radio (21 cm H I) wavelengths and concluded that their sample showed the same overall trends of global properties with morphological type as do higher surface brightness (HSB) galaxies. They also found their data consistent with LSB galaxies having lower total masses than HSB galaxies.

Other early studies of LSB galaxies adopted a different approach. They took advantage of the small (1 arcmin) limit and high completeness of the angular-diameter limited Uppsala General Catalog of Galaxies (UGC, Nilson 1973). These properties allow the UGC to contain some galaxies of lower surface brightness than the “standards” that define the Hubble sequence. Romanishin et al. (1982) examined

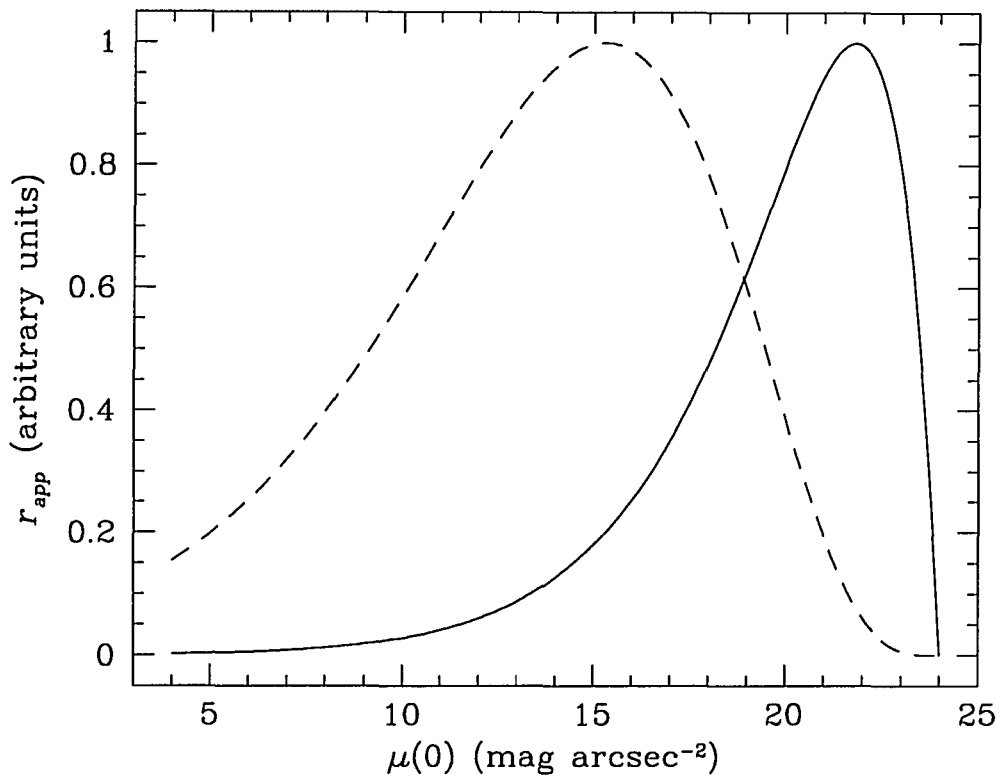


Figure 1.1: Apparent radius of a galaxy as a function of its central surface brightness, for a fixed total galaxy luminosity and assuming a limiting surface brightness of 24 B mag arcsec $^{-2}$. The solid line shows the function for galaxies with exponential profiles, and the dashed line shows the profile for galaxies with $r^{1/4}$ profiles.

a sample of such UGC galaxies and concluded that their sample was systematically underluminous in the H band Tully-Fisher (Tully & Fisher 1977) relation; they concluded from this that LSB galaxies have higher mass-to-light ratios than HSB galaxies. Romanishin et al. (1983) also performed optical surface photometry on this same sample, and found that their LSB galaxies were of comparable scale length to HSB galaxies, and that they were generally bluer. Bothun et al. (1985b) and Bothun et al. (1986) conducted a redshift survey of LSB galaxies identified from the UGC in much the same manner as the sample of Romanishin et al. (1982). They concluded that LSB galaxies generally trace the same large-scale structures defined

by HSB galaxies.

A fainter limiting isophote will both improve the chances of finding LSB galaxies, and extend the range of detectable central surface brightnesses, as Equation 1.3 makes clear. Detection systems more sensitive than standard Schmidt telescope survey plates typically cover much smaller angular regions of sky, so the LSB galaxy searches that have employed more sensitive techniques are generally directed at dense clusters. This effort began with the monumental survey of the Virgo cluster by Binggeli et al. (1985), which used deep photographs ($\mu_{lim} = 25.5 \text{ mag arcsec}^{-2}$) taken with the Las Campanas 100 inch telescope. They detected a large number of previously unseen dwarf galaxies, some with central surface brightnesses $\mu_B(0) \approx 24.5 \text{ mag arcsec}^{-2}$. Impey et al. (1988) used photographically amplified deep images of the Virgo cluster to push the limiting isophote to $\mu_{lim} = 27.2 \text{ mag arcsec}^{-2}$. They found LSB dwarf elliptical galaxies that extended the range of known central surface brightnesses down to $\mu_B(0) \approx 26 \text{ mag arcsec}^{-2}$. They determined that these LSB dwarfs steepened the low-luminosity tail of the luminosity function so much that a slope representing divergent total luminosity could not formally be ruled out, although the corrections for incompleteness were limited by small number statistics. Other studies of the Fornax cluster using the same technique (Bothun et al. 1991), using automated scans of UKST plates (Irwin et al. 1990), using deep photographs taken specifically for identifying faint galaxies (Ferguson & Sandage 1988) and using CCDs (Davies et al. 1990 and Cellone et al. 1994) have found similar results there. Also, two of these cluster studies (Impey et al. 1988 and Bothun et al. 1991) concluded that these LSB dwarfs must have high mass-to-light ratios to avoid being disrupted by tidal forces as they move through the deep potential wells of these dense clusters.

As in all new fields of research, some discoveries come by accident. Malin 1, the largest spiral galaxy yet found, was discovered by Bothun et al. (1987) in the course of the Virgo cluster survey reported by Impey et al. (1988). Malin 1 happens to lie directly behind the Virgo cluster at a recessional velocity of $\sim 25000 \text{ km s}^{-1}$. Its bulge was first believed to be a dwarf elliptical in the Virgo cluster, but the amplified photographs revealed a large, very LSB disk that had previously escaped detection. Followup observations revealed a very blue disk ($B-V = 0.5$) with a very long scale length ($r_{\text{sl}} = 55 h_{100}^{-1} \text{ kpc}$), and a very low central surface brightness ($\mu_B(0) = 26.5 \text{ mag arcsec}^{-2}$). Despite the low luminosity density, Malin 1 has a high total luminosity, with $M_B = -21.5$, a very high H I mass, with $M_{\text{HI}} = 1.1 \times 10^{11} M_{\odot}$, and a high ratio of hydrogen mass to blue luminosity (Impey & Bothun 1989). Another spiral galaxy with an even lower central surface brightness ($\mu_R(0) = 26.5 \text{ mag arcsec}^{-2}$) was accidentally discovered by Davies et al. (1988). They were looking for LSB galaxies in the Abell cluster A1367 with deep CCD images, and they found this galaxy, designated GP 1444, on one of their adjacent “blank sky” fields that had been taken for flatfielding the other images. The intrinsic size of GP 1444 is still unknown because no velocity is available for it yet. Two other examples of “Malin 1 cousins” have also been described in detail by Bothun et al. (1990) and Sprayberry et al. (1993). These unusual galaxies forcefully illustrate the power of selection effects in limiting our knowledge of the true range of galaxy properties.

In surveys for LSB galaxies in the general field, Binggeli et al. (1990) identified several hundred mostly LSB dE and dI galaxies on deep Palomar Schmidt plates taken for that purpose. They determined that dwarf galaxies follow a morphology-density relation in that dE’s are almost always found in clusters or as companions to giants, while dI’s are more likely to be found as isolated field galaxies. Schombert

& Bothun (1988) and Schombert et al. (1992) have made visual searches on the Second Sky Survey plates of the Palomar Observatory (POSS-II), which have a limiting isophote about $1 \text{ mag arcsec}^{-2}$ fainter than the original POSS plates. They identified over 300 LSB galaxies in almost 1000 square degrees of sky. Followup studies of these galaxies have revealed a great deal about the properties of LSB field galaxies. Schombert et al. (1990) and Knezek (1993) found that these galaxies were generally lacking in detectable molecular gas, suggesting that the star formation mechanisms at work there were different from those in HSB spirals. McGaugh & Bothun (1994) analyzed the colors and metallicities of a subset of these galaxies and concluded that their blue colors and modestly reduced metallicities were best explained by star formation that had begun only recently and that proceeded slowly and uniformly. Bothun et al. (1993) performed a statistical analysis of the number of near neighbors (within a projected radius of $2.5 h_{100}^{-1} \text{ Mpc}$ and 500 km s^{-1} in velocity) around these LSB galaxies (as well as some from the survey described here), and concluded that LSB galaxies are less likely to have near neighbors than are their HSB counterparts; Zaritsky & Lorrimer (1993) reasoned that this deficit implied a correspondingly low rate of tidal interactions, which in turn could explain the low rates of star formation usually inferred for the LSB galaxies.

1.2 Motivations for the Present Work

These prior surveys for LSB galaxies in the field all suffered from one serious drawback: they were based on visual searches of photographs which were carried out under circumstances that did not allow for any quantitative estimates of their completeness. Schombert & Bothun (1988) and Schombert et al. (1992) specifically

noted that their lists were incomplete. A complete sample, or at least one whose incompleteness is understood and correctable, is needed to ensure that full range of galaxy properties has been sampled. Incomplete samples can enlarge the range of known properties but cannot hope to define the limits of that range. Also, completeness is necessary for a variety of statistical studies of the galaxy population, including the estimate of a luminosity function corrected for the effects of surface brightness selection.

The galaxy luminosity function is a fundamental input to observational cosmology (Binggeli et al. 1988, Schechter 1976). Among other purposes, it is used: to calculate a luminosity density over cosmological volumes; in conjunction with estimates of galaxy mass-to-light ratios, to estimate mass densities over cosmological volumes; to determine selection effects in magnitude limited samples; to estimate the cross section of absorbers in quasar spectra; and to relate the excess of faint blue galaxies observed at $z \sim 0.4$ (Tyson 1988, Colless, et al. 1990) to the population observed locally. The shape of the luminosity function is a major constraint on theories of galaxy evolution, and work in the Virgo (Impey et al. 1988) and Fornax (Bothun et al. 1991) has demonstrated that the profusion of LSB dwarfs there steepens the exponential tail of the luminosity function considerably. A similar inclusion of LSB galaxies in the field luminosity function is needed to ensure that the field luminosity function properly represents the full range of morphologies present in the field.

To fill this need for a complete census, a survey has been undertaken for LSB galaxies that combines visual search techniques with automated scanning of plates. The visual search allows the identification of a wide variety of interesting morphologies, and the automated scanning ensures completeness to objective and

well-defined limits of angular size and surface brightness. This survey and a few of its results are the subjects of this dissertation. For the remainder of this dissertation, we adopt as a working definition of “low surface brightness” the criterion used in the automated scanning process of this survey: an extrapolated central surface brightness of $\mu_B(0) \gtrsim 22 \text{ mag arcsec}^{-2}$. This criterion will be explained in more detail in Chapter 2. The survey was conducted on 24 sky survey plates from the UKST, in the region of the sky defined by $-3^\circ \leq \delta \leq +3^\circ$ and $|b| \geq 30^\circ$. The angular extent of the survey was 786 square degrees. The UKST survey plates have a limiting isophote $\mu_{lim} = 25.9 \pm 0.7 \text{ mag arcsec}^{-2}$, deeper than the POSS-II, thus allowing the detection of lower surface brightness objects. The survey identified 693 previously uncataloged galaxies, mostly of low central surface brightness and all with extended low surface brightness features. Followup observations provided CCD surface photometry of 112 galaxies, low-resolution optical spectroscopy of 264 galaxies, and 21 cm H I detections of 190 galaxies.

Chapter 2 reviews the details of the survey and analyzes its completeness. A program of simulations is described that allows the quantification of the detection efficiency of the survey, as a function of galaxy size and surface brightness. This selection function can then be used to determine the completeness limits of the survey and to correct for incompleteness in the range where the survey is only partially complete. This chapter also details the photometric calibrations that allow magnitude estimates to be made for all the newly discovered galaxies.

Chapter 3 reviews the techniques for estimating a field galaxy luminosity function and describes the incorporation of incompleteness corrections in these techniques. The selection function of Chapter 2 is then used to develop a corrected luminosity function for the survey LSB galaxies, and a corrected luminosity function

for both LSB and HSB galaxies. The chapter concludes with a discussion of the implications of this corrected luminosity function for the study of the copious number of faint blue galaxies seen at moderate redshifts (*e.g.*, Tyson 1988).

Chapter 4 presents a Tully-Fisher analysis of a subset of the survey LSB galaxies, and compares the results to those obtained with the Tully-Fisher method on samples of HSB galaxies. Unlike most applications of the Tully-Fisher method, the goal here is not to estimate distances but rather to compare the luminosity and dynamical properties of LSB and HSB galaxies. In particular, the analysis is aimed at finding differences, if they exist, in the mass-to-light ratios of LSB and HSB spiral galaxies.

Chapter 5 examines a different subset of the LSB galaxies from the survey. This subset consists of spirals with very low central surface brightnesses and very long disk scale lengths: the “Malin 1 cousins.” Their properties as a class are systematically studied and compared to those of normal HSB spirals. Existing galaxy redshift catalogs are also searched for neighbors to these giant LSB spirals, to look for relationships between their unusual appearance and their immediate environments.

Chapter 6 summarizes the conclusions of Chapters 2 through 5 and draws the connections among their results. Several avenues of future research are also explored. Finally, Appendix A presents a table of basic data for the entire set of survey galaxies.

Chapter 2

SELECTION EFFECTS AND COMPLETENESS OF THE APM SURVEY

We discuss the techniques employed for identifying low surface brightness (LSB) galaxies for the APM survey. We present the method of calibrating the photometry performed from the APM scans, and discuss the uncertainties associated with the calibrations. We also review the possible sources of incompleteness in the survey, and we present the results of a program of simulations to estimate the completeness as a function of galaxy parameters. Finally, we discuss the implications of the survey results and show in particular that the observed distribution of central surface brightnesses is inconsistent with the notion that spiral galaxies have a gaussian distribution of central surface brightness with $\langle \mu_B(0) \rangle = 21.65 \pm 0.4$.

2.1 Introduction

The intrinsic brightness and color of the night sky limit our ability to measure the properties of galaxies. Galaxy detection involves measuring a diffuse signal in the presence of this filter of sky noise. Galaxies are detected and selected not by their total luminosity, but rather by their angular size above a limiting isophote level (Disney 1976). For a given total luminosity, both high surface brightness (HSB) and low surface brightness (LSB) galaxies will be excluded, HSB galaxies because they become indistinguishable from stars and LSB galaxies because their signals are buried under the sky noise. By limiting the detected galaxies to a narrow range of surface brightness, this filter also limits our knowledge of the true distributions of galaxy surface brightness, luminosity and physical size.

The best way to determine the effects of this filter is to locate and analyze a population of galaxies that the filter has excluded from existing catalogs. One approach to locating such a population uses observational techniques with much fainter limiting isophotes than is conventional with standard Schmidt telescope survey plates, such as amplified photographs (*e.g.*, Impey et al. 1988), matched detection filters optimised for finding large low surface brightness objects (*e.g.*, Irwin et al. 1990) which are equivalent in performance to amplified photographs, or CCD surveys (*e.g.*, Davies et al. 1994). These techniques can sample a relatively large range of the surface brightness distribution (whatever it may be), but at present they have only been applied to modest regions of sky. The other approach is to examine normal Schmidt telescope survey plates *very* carefully. This does not provide the extremely faint limiting isophotes available from other techniques, but does make wide field surveys possible. Schombert & Bothun (1988) and Schombert et al. (1992) have developed a list of over 300 LSB galaxies by visually searching plates from the

second Palomar Observatory Sky Survey. The analysis of galaxies from their lists (*e.g.*, McGaugh & Bothun 1994) has provided valuable insight into the properties of LSB galaxies, but the impossibility of judging the completeness of visual surveys has limited the statistical use of them.

We have also adopted the technique of careful examination of existing survey plates, but we have chosen to combine visual searches with automated scanning. The use of automated scanning allows the completeness of the resulting galaxy list to be estimated objectively, thus making the survey results useful for statistical analyses such as estimation of a luminosity function. A further advantage of machine-based measures that we have not exploited here, is that automated classification algorithms are extremely effective at detecting HSB galaxies which are only marginally distinguishable from stellar objects. Disney and coworkers (personal communication) have used this technique to search for putative HSB galaxies belonging to the Fornax cluster. Although a few previously unknown HSB cluster members were found here was clear evidence that a large hidden HSB population is not present in the Fornax cluster (cf. Allen & Shu 1979). In this paper, we discuss the process of identifying LSB galaxies from UK Schmidt Telescope survey plates (Section 2.2), and describe the photometric calibrations that make possible magnitude estimates of the identified galaxies (Section 2.3). We also analyze the completeness of the resulting galaxy list, and obtain through simulations an objective estimate of the survey completeness as a function of galaxy parameters (Section 2.4). Finally, we discuss the implications of our survey results for the question of whether there exists a typical value of central surface brightness for spiral galaxies (Section 2.5). The list of LSB galaxies appears in Appendix A.

2.2 The Selection Process

Target LSB galaxies were identified using a combination of both automated and eyeball searches of glass copies of UK Schmidt Telescope (UKST) IIIaJ survey plates. Twenty four equatorial fields covering an area of 786 deg^2 of sky were surveyed, with the candidate LSB galaxies selected from a total of well over 10 million images in the strip.

The Automated Plate Measuring (APM) facility at Cambridge¹ was used to locate all objects on a plate meeting certain criteria (for a general description of the APM facility, see Kibblewhite et al. 1984). To be included as a candidate LSB galaxy, an object must have a minimum area of $2.5 \log N = 6.5$, where N is the number of connected pixels at or above the detection threshold. The detection threshold is set at 2σ above the modal value of the background, where σ is the pixel noise level of the background. This detection threshold corresponds to a typical surface brightness of $\mu_B = 24.5 \pm 0.5 \text{ mag arcsec}^{-2}$ as determined from the photometric calibrations described in Section 2.3. The uncertainty in this number reflects both the uncertainty in the photometric calibration and the scatter from plate to plate. Images are defined as groups of contiguous pixels above the detection threshold. The plates were measured at a resolution of $15 \mu\text{m}$ with a pixel sampling of $7.5 \mu\text{m}$, or $0.51 \text{ arcsec/pixel}$ given the 67.14 arcsec/mm scale of the UKST plates. The minimum image area defined previously is thus $\approx 100 \text{ arcsec}^2$ on the sky. A radial exponential model was fitted to the unsaturated part of the areal profile (pixel intensity vs. number of pixels at that intensity), and a candidate object was also required to have an extrapolated model central surface brightness of

¹The APM is a National Astronomy Facility, at the Institute of Astronomy, operated by the Royal Greenwich Observatory.

$\mu_B(0) \gtrsim 22 \text{ mag arcsec}^{-2}$. This second criterion eliminates virtually all the so-called 'normal' galaxies from the sample. The objects revealed by these scans were then reviewed by eye to eliminate as many previously cataloged galaxies, plate flaws, Galactic cirrus clouds, and other interlopers as possible. Finally, each detected object that passed the visual review was digitized in a raster scan of 512×512 pixels (for objects $\gtrsim 30 \text{ arcsec}$ in diameter) or 256×256 pixels (for objects $\lesssim 30 \text{ arcsec}$ in diameter).

The visual search was carried out independently of the automatic scan using a combination of low power ($\times 5$) binocular microscope and direct eye search. A similar visual search in the Fornax cluster (Irwin et al. 1990) had shown that direct visual examination of UKST glass copy survey plates could detect LSB galaxies with central SB as low as $26 \text{ mag arcsec}^{-2}$ but that the success rate was a strong function of the image scale size and was difficult to quantify. Each plate was searched in lanes $\sim 5 \text{ cm}$ wide and any LSB feature or galaxy with unusual extended morphology noted. Straightforward use of a 40 cm graduated rule sufficed to locate the candidates to within $1/2 \text{ mm}$ with respect to the plate edges. Knowledge of the plate center, scale and orientation enabled these 'x-y' coordinates to be translated into celestial coordinates with an accuracy of better than 1 arcmin . These celestial coordinates were sufficiently accurate that the images could then be automatically measured (in the form of 2D pixel maps) using the APM. Subsequent centroiding from the 2D maps enabled accurate ($\sim 1 \text{ arcsec}$) coordinates to be obtained. We note that both the visual and machine search used glass copies rather than original UKST survey plates because: (a) the background density is adjusted during copying to be roughly constant ($\sim 0.6D$) irrespective of the original plate background density; (b) a modest amount of contrast enhancement around sky background is also folded in, which in conjunction with (a) makes LSB features easier to see; (c) exhaustive

tests have shown that the information content of original plates is not noticeably degraded by good quality contact copying; (d) the copy plates are readily available and the originals are not.

Objects selected by eye are then combined with the machine-selected sample in a master list of candidates for followup CCD photometry, optical spectroscopy and 21 cm radio observation. The eyeball search is a necessary adjunct to the automated scanning because the global parametric requirements of the automatic search cannot be guaranteed to pick out all galaxies of manifestly unusual morphology. The Malin 1 type galaxies (see Bothun et al. 1987 and Sprayberry et al. 1993) provide excellent illustrations of this problem. The prominent nuclear components of these galaxies outweigh the contribution of the LSB disk detected at the detection threshold ($\sim 24.5 \text{ mag arcsec}^{-2}$), causing the apparent surface brightness to lie below the surface brightness selection boundary. Although given the benefit of hindsight it is possible to generalize the automatic selection criteria to cope with cases like this, eventually the selection criteria become too complicated to readily interpret in terms of easily measurable galactic properties and there is no guarantee of picking all interesting types. It is more logical to rely on the machine search to ensure completeness to some simple well-defined selection boundaries and to use the visual search to include a wider variety of interesting morphologies.

This two-part process resulted in a final list of 693 previously uncataloged target galaxies. Because of various practical constraints on the completion of the survey, the complete list was assembled from two components. The large angular size or “LAS” list included 513 previously uncataloged galaxies that are generally $\gtrsim 30$ arcsec in diameter, the small angular size or “SAS” list covered the remaining 180 objects that are predominantly $\lesssim 30$ arcsec in diameter. The LAS list was completed

first, and the galaxies on that list have much better morphological information available from the APM scans, so the galaxies targeted for followup observation were chosen from the LAS list.

2.3 Photometric Calibration

Photometric calibration of the digitized APM scans was carried out using the general method outlined by Cawson et al. (1987). This method involves comparing the APM scans to externally calibrated CCD images of the same galaxies. As part of our campaign of followup observations, we obtained CCD photometry in Johnson *B* and *V* and Kron-Cousins *R* bands of 125 of the target objects. Galaxies were selected for CCD photometry based on several criteria. The most important were covering a representative sample of the morphologies seen in the survey, covering as many of the twenty four UKST plates as possible, and observational constraints such as minimizing airmass while maximizing observing efficiency. Nineteen nights of observations were carried out with the Steward Observatory 2.3m telescope on Kitt Peak. The nineteen nights were separated into eight observing runs over the period December 1990 through September 1992. Observations prior to May 1992 (about 80% of the total) used a thinned Texas Instruments 800×800 pixel detector, and those after May 1992 (the remaining 20%) used a thick Loral 2048×2048 pixel detector. Both detectors have 15 μm pixels, and both were used in direct imaging mode with 2×2 on-chip binning to yield an image scale of 0.3 arcsec pixel⁻¹. Field size was 2 × 2 arcmin for the TI and 5 × 5 arcmin for the Loral. Bias subtraction, dark current subtraction, and flat-fielding were carried out with the IRAF² data

²The Image Reduction and Analysis Facilities package is distributed by NOAO, which is operated by AURA Inc. under contract to the National Science Foundation.

reduction package. Standard stars from the lists of Christian et al. (1985) or Odewahn et al. (1992) were used for photometric calibrations. At least two fields were observed each night, giving an average of 15 stars per night. Internal errors in each night's photometric zeropoints were typically ≈ 0.03 mag, and the scatter among the zeropoints for each detector was ≈ 0.06 mag for the TI detector and ≈ 0.08 mag for the Loral detector.

After eliminating galaxy images that were compromised by weather or instrumental problems or by defects in the APM scans (*e.g.*, the galaxy being too near the edge of the plate), 106 galaxies remained for use in calibrating the APM scans. The breakdown of calibrators in each field appears in Table 2.1. Magnitudes and $B - V$ and $V - R$ colors for these galaxies were measured by aperture photometry in circular apertures centered on the intensity peak of the galaxy. First, the sky background was measured and subtracted from the image. The backgrounds were measured by making histograms of the pixel values in the four corners of each image, or in other regions well away from the galaxy if the galaxy was not centered in the frame. A gaussian was fit to the central peak of each histogram, and the center (the mode of the pixel histogram) and width of that gaussian were adopted as the background level and its uncertainty in that region. Then, for each image, the four modal values were ranked, the highest and lowest discarded, and the average of the remaining two was taken to be the background for the entire image. Next, the appropriate aperture radius was determined by measuring the total intensity within expanding concentric apertures until the intensity vs. radius growth curve became flat. Increasing the aperture radius in a number of small steps to determine the appropriate maximum also allowed a straightforward estimate of the half-light radius as the radius of the circular aperture that enclosed half of the total intensity found within the maximum aperture. Finally, a central surface intensity was determined by

Table 2.1: UKST Fields: Photometric Calibrations

Field Number	RA	TI	Loral	σ
(1)	(2)	(3)	(4)	(5)
892	23:00	4	0	0.19
893	23:20	4	2	0.19
894	23:40	4	2	0.21
824	00:20	4	3	0.23
826	01:00	7	0	0.22
827	01:20	0	3	0.25
828	01:40	0	3	0.25
830	02:20	0	2	0.25
831	02:40	9	0	0.21
833	03:20	6	0	0.16
834	03:40	8	0	0.15
835	04:00	2	0	0.25
851	09:20	7	0	0.20
853	10:00	7	0	0.14
854	10:20	3	0	0.25
855	10:40	4	0	0.24
856	11:00	3	0	0.25
857	11:20	3	0	0.25
859	12:00	4	0	0.20
860	12:20	6	0	0.24
862	13:00	2	0	0.25
863	13:20	1	0	0.25
865	14:00	0	1	0.25
867	14:40	0	2	0.25

Notes:

Column (1) lists the UKST plate numbers.

Column (2) lists the center RAs as hh:mm (1950.0). Center Dec = 0° for all plates.

Column (3) lists the number of calibrator galaxies observed with the TI CCD.

Column (4) lists the number of calibrator galaxies observed with the Loral CCD.

Column (5) is the adopted uncertainty in the APM-to-CCD transformation in magnitudes.

measuring the average intensity per pixel within the smallest concentric aperture. This smallest aperture had a diameter of 4 arcsec to provide adequate signal-to-noise in the lowest surface brightness objects. The measured intensities were then converted to magnitudes and magnitudes per square arcsecond using zeropoints and color terms derived from the standard stars observed on that night, and the magnitudes and surface brightnesses were corrected for Galactic extinction using the reddening maps of Burstein & Heiles (1982). The k -corrections from the tabulations of Coleman et al. (1980) were applied to all objects with measured velocities; the tabulated colors of their Sbc, Scd, and Irr types match the range of measured colors for the LSB galaxies nicely. The surface brightnesses and magnitudes of these objects were then corrected for cosmological dimming as $(1+z)^4$ and $(1+z)^2$, respectively.

Following the prescription of Cawson et al. (1987), we determined the transformation between APM “density” units and CCD intensities using the following 7 steps. First, the CCD image was rebinned to the same pixel scale as the APM scan ($0.51 \text{ arcsec pixel}^{-1}$). Second, the CCD image and APM scan were registered using foreground stars present in both images, and both images were trimmed to the same size. Third, the backgrounds were measured as described above and subtracted from the CCD image and APM scan. Fourth, the background-subtracted CCD image was scaled from B to the B_J bandpass of the APM scans using the transformation $B_J = B - 0.25(B - V)$ (per Blair & Gilmore 1982) and the overall B magnitude and $B - V$ color of the galaxy previously determined from the CCD photometry. Fifth, the background-subtracted CCD image was divided by its exposure time and the APM image was scaled by the ratio of APM units to UKST plate density units ($10000 \text{ APM units} = 1 \text{ unit of plate density}$). Sixth, a scatter plot was formed between normalized CCD intensity and plate density for each pixel. This scatter plot has a clustering at the origin, since most pixels are

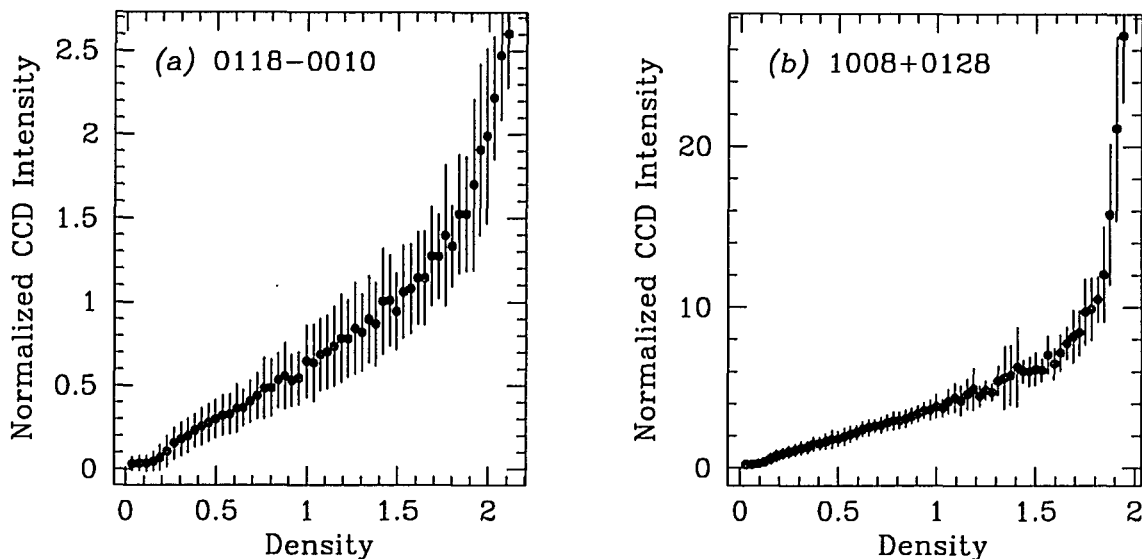


Figure 2.1: Examples of characteristic curves obtained from individual APM scans. Each point represents the average of all points from the scatter plot within a bin of width 0.05 units in normalized APM density. The vertical axis is in units of CCD intensity, normalized by the exposure time, and the horizontal axis is in units of UKST plate density. Galaxy 0118-0010 in (a) was observed with the Loral 2048 \times 2048 CCD, and Galaxy 1008+0128 in (b) was observed with the TI 800 \times 800 CCD. Note the difference between the vertical axis scalings due to the difference in B band quantum efficiency between the two CCDs.

sky. The ridgeline of this scatter plot defines the characteristic curve of the scanned plate section. Two examples appear in Figure 2.1. Finally, an average characteristic curve was determined for each UKST plate, and a fourth-order polynomial fit to that average curve is then used to transform the scaled APM values pixel-by-pixel into normalized CCD intensities, which can be calibrated into magnitudes using the standard-star zeropoints. The average characteristic curves for four representative plates appear in Figure 2.2, along with the overall average for the plates which had more than three calibrating galaxies.

The number of calibrator galaxies varies considerably from field to field. Also,

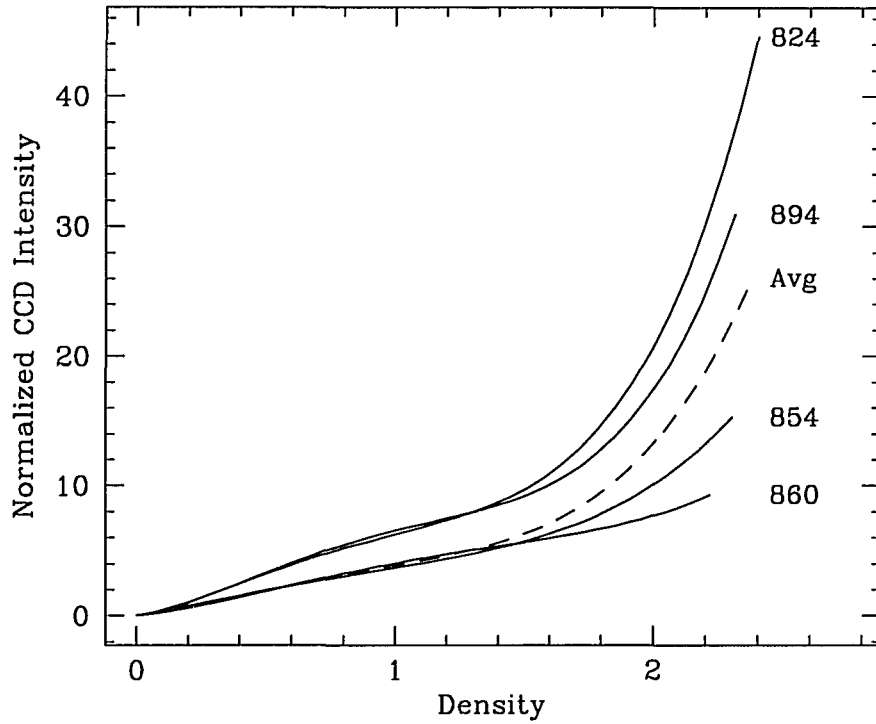


Figure 2.2: Plate-average characteristic curves for four representative UKST plates (solid lines), along with the overall average of the 13 well-calibrated plates (dashed line).

characteristic curves determined from the Loral CCD are not useable in combination with those determined from the TI CCD, due to the differences in quantum efficiency and color response of the two detectors. While it would in principle be possible to combine individual curves from the two detectors by calibrating the vertical axes into physical flux units (*e.g.*, $\text{erg cm}^{-2} \text{sec}^{-1}$ over the filter bandpass), there is no practical reason for doing so with these data. Only three of our UKST fields have calibrator galaxies observed with both detectors, and all three are well calibrated by the galaxies observed with the TI CCD. For both these reasons we determined plate-average curves only for the 13 plates that have 4 or more calibrator galaxies observed with the same CCD. For these 13 plates, the uncertainties quoted

in Table 2.1 are the formal uncertainties computed from the scatter among the calibrator galaxies for each plate. For the remaining 11 plates, we used the average of all the plate-average curves from the 13 well-calibrated plates. For these 11 plates, the quoted uncertainties reflect the external scatter among the transformations of the other 13 plates. This external scatter (0.25 mag) is about as large as the largest internal uncertainty (0.24 mag) for any one of the 13 well-calibrated plates. As a final external check, we estimated magnitudes for the 106 calibrator galaxies from their APM scans using these transformations. The mean magnitude difference $m_{CCD} - m_{APM}$ was -0.11 ± 0.26 (rms), which is consistent with the transformation uncertainties quoted in Table 2.1.

These transformation curves allow magnitudes to be estimated from the APM scans in the following manner. First, the background is measured as described above and subtracted from the scan. Second, the image is scaled into plate density units. Third, each pixel is transformed from a plate density value to a “normalized CCD B_J intensity” using the fourth-order polynomial fit to the applicable characteristic curve. Fourth, aperture photometry was performed on the transformed image in the same manner as for the CCD images to obtain a total intensity. Fifth, the total intensity was calibrated to a magnitude using an average B_J zeropoint for the relevant detector. Finally, to put all the galaxies on a common basis for comparisons, we converted the B_J magnitudes to B using the above color transformation equation and assuming $B - V = 0.53$, which is the median $B - V$ color of the 106 calibrator galaxies. The rms scatter in the $B - V$ colors of the calibrators is 0.21 mag, so the use of a fixed color term in the B_J to B transformation introduces a negligible additional uncertainty of 0.05 mag. Because the LAS and SAS lists were obtained from the same set of UKST plates, the same procedures were used for both lists. The method also yielded estimates of the half-light radius and central surface brightness,

in the same manner as described above for the CCD images.

We note that our transformation uncertainties are larger than those obtained by Cawson et al. (1987) using this same procedure. First, they obtained CCD images of 17 galaxies to calibrate a single UKST plate, compared with our average number of 4 useable calibrators per plate. Second, their galaxies were bright, high S/N ellipticals or early-type spirals with large numbers of pixels at flux levels well above the sky background. Most of the area of our LSB galaxies consists of pixels with net intensities only a few percent of the sky level. As a consequence, the characteristic curves of our galaxies are not as well determined, especially at the bright end. Third, the Cawson et al. (1987) CCD data were obtained in one observing run, whereas our CCD images were taken on 19 different nights separated into eight observing runs distributed over a two-year period. For all of these reasons, we were not able to duplicate their average photometric uncertainty of 0.1 mag. After accounting for the transformation uncertainties listed in Table 2.1, the zeropoint uncertainties that result from using averages of zeropoints taken from many nights, and the usual internal measurement uncertainties, our number-weighted average photometric uncertainty is 0.20 mag per galaxy.

2.4 Completeness

As mentioned above, the scanning of the UKST plates was completed in two parts, the LAS list and the SAS list. Due to the timing of the plate scanning and the followup observations, and to the superior morphological information available for objects on the LAS list, all the followup observations were limited to the LAS list. However, the SAS list was developed using the same galaxy detection criteria as the

LAS list, and from the same UKST plates. In evaluating the completeness of the survey, we will therefore consider the two lists together.

The digitized sections of UKST plates have high levels of background noise from different sources, including: shot noise in the sky flux, emulsion response, emulsion grain size, chemical fog during development, and emulsion and chemical effects during photographic copying of the plates. Measurement of the background level and its uncertainty by the peak and width of the pixel histogram reveals that the 1σ uncertainty is about eight times the level predicted by a simple Poisson noise model assuming simple object-plus-sky photon counts; this difference is not surprising since much of the noise comes from sources other than photon counting. To complicate matters further, the noise is not random spatially; it is clumpy, or spatially correlated, with a correlation scale length (*i.e.*, half-power point of the radial autocorrelation function) $\approx 3.2 \pm 0.3$ pixels. The correlation is caused by the finite spot size of the laser beam projected onto the plate (Gaussian core of $\sim 10\ \mu\text{m}$ FWHM) combined with the on-line 2×2 digital coaddition to form each output pixel. Such a large, patchy noise signal could cause some galaxies to be missed, especially if their surface brightnesses and sizes are such that they would fall near the detection limits of the survey.

To estimate the extent of this effect, and to understand the detection efficiency as a function of galaxy size and surface brightness, we created artificial APM scans of model galaxies with known structural parameters and passed these scans through the detection algorithm to determine the detection rate as a function of galaxy size and surface brightness. To simplify the analysis, we chose a face-on exponential profile for the model galaxies. This choice is reasonable for our survey, since most of our detected galaxies are fairly close to face-on (the median ellipticity as measured by

simple moments analysis on the images is 0.23) and exhibit radial profiles in annular surface brightness vs. radius plots that are well-approximated by an exponential (see also Impey, Bothun, & Malin 1988, Bothun, Impey, & Malin 1991, and McGaugh & Bothun 1994). Each model was therefore completely defined by two numbers, the central surface brightness ($\mu_B(0)$) and the exponential scale length (r_{scd}). Finally, we simulated the effects of seeing by convolving each model galaxy with a circular gaussian of width comparable to that of the typical seeing disk on the APM scans. The seeing disk was found to have a size of ≈ 2 arcsec FWHM, as measured from the images of unsaturated stars.

It is difficult to judge how the use of only face-on profiles affects the completeness estimates. If the model galaxies were assumed to be opaque, the use of inclination greater than zero (*i.e.*, other than face-on) would reduce the number of pixels above the threshold by a factor equal to the cosine of the inclination angle (for moderate inclinations). Inclined galaxies would be less likely to be detected, and the assumption of face-on models would thus overstate the completeness at a given pair of galaxy parameters. If the models were assumed to be completely transparent, then the surface intensity of the galaxy pixels would increase as the number decreased, and the net number above the threshold would not change for moderate inclinations. In this case, the assumption of face-on models would have less effect on the completeness estimate. The real optical depth of the LSB galaxies lies somewhere between these two extremes. In any case, the effects of the assumption are probably small due to the relatively low average ellipticities of the LSB galaxies detected in the survey.

Simulating the noisy background of the APM scans required matching both the overall noise level and the spatial correlation. We created images with a fixed

background level and a large random noise component using a standard random number generator. This background plus noise image was then convolved with a circular gaussian to simulate the clumpiness. The convolution also reduced the noise, so the noise level in the original artificial image was scaled up by the quadrature sum of the parameters of the convolving gaussian function to give the desired noise level in the final, convolved image. Thorough testing confirmed that these convolved images were indistinguishable from the real APM scans in both background noise level and spatial correlation of the noise. Finally, the convolved noise image was added to the seeing-convolved model galaxy image to obtain the final image for analysis. This process ignores the additional Poisson noise component associated with flux from the galaxy (i.e., it assumes the galaxy itself is completely noiseless). This omission is harmless, however, as the background noise completely dominates the Poisson noise associated with the galaxy flux at the surface brightness levels of interest here.

For each pair of galaxy parameters $(\mu_B(0), r_{scl})$, 100 galaxy-plus-background-noise frames were created and passed through the detection algorithm, and a record was kept of the number of detections out of the 100 trials. Stepping through a grid of galaxy parameters allowed the development of a two dimensional selection function, which gives the probability that a galaxy will be detected by the APM scan as a function of $\mu_B(0)$ and r_{scl} . We then convolved the two dimensional selection function with a one dimensional gaussian of $\sigma = 0.5 \text{ mag arcsec}^{-2}$ in the surface brightness dimension to account for the uncertainty in the average detection threshold used to develop the original function. The final selection function is shown in Figure 2.3. As anticipated, the surface defined by this function shows an effective completeness of 100% at central surface brightnesses brighter than $\mu_B(0) \approx 23.0 \text{ mag arcsec}^{-2}$, and in the range of $\mu_B(0)$ where completeness is $< 100\%$, the completeness increases

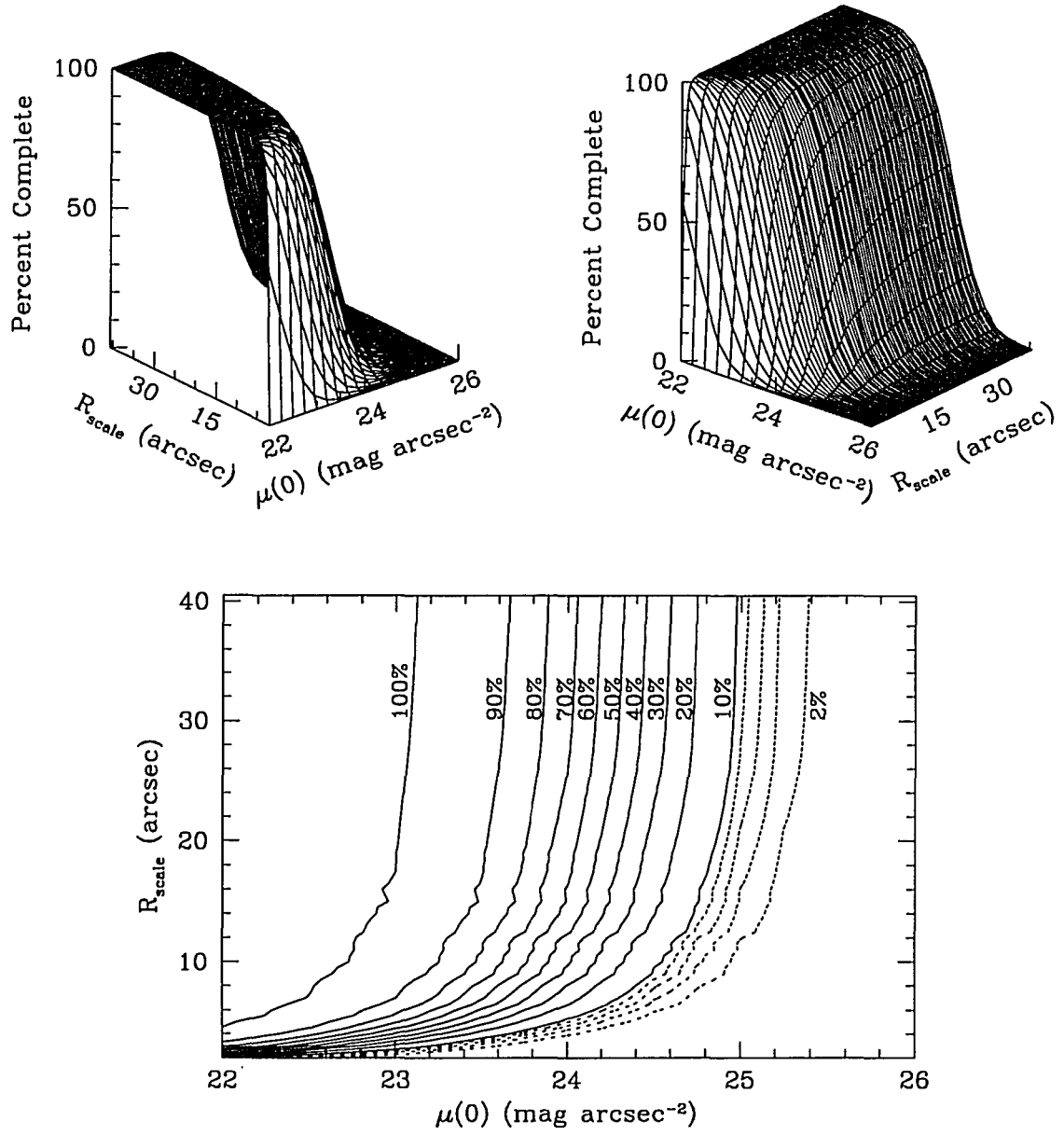


Figure 2.3: The selection function showing APM completeness as a function of galaxy $\mu_B(0)$ and r_{scl} . The upper panels are different perspective views of the surface, and the lower panel is a contour plot of the surface. In the lower panel, the dotted contours indicate a contour interval of 2% in completeness, running from 2% to 8%, and the solid contours indicate contour intervals of 10%, running from 10% to 100% completeness.

with increasing r_{scl} .

The effectiveness of this completeness correction can be checked by applying the $\langle V/V_{max} \rangle$ test of Schmidt (1968) and Felten (1976) to the combined (*i.e.*, LAS list plus SAS list) sample of LSB galaxies. The APM detection process requires that detected galaxies have a minimum number of connected pixels at or above the detection threshold. This requirement is equivalent to a minimum angular diameter of 11.5 arcsec for the case of an E0 or face-on spiral galaxy, cases which will give a minimum angular size for the given area. For an angular size limit θ_{lim} , $V/V_{max} = (\theta_{lim}/\theta_0)^3$, where θ_0 is the measured angular diameter of the galaxy at the limiting isophote. This calculation of V/V_{max} does not depend upon the intrinsic physical size of the galaxy, so there is no Malmquist-type bias. This simple calculation assumes no cosmological corrections in the relation between angular diameter and distance, but the median velocity of the LSB sample is only 7300 km s⁻¹, so the bias introduced is slight. There is also an implied apparent magnitude limit, based on the requirement that the pixels within the minimum area all be at or above the detection threshold. Using the formalism of Davies (1993), the implied apparent magnitude limit for completeness here is ≈ 19 magnitudes in B .

A simple unweighted average of the V/V_{max} values gives $\langle V/V_{max} \rangle = 0.18 \pm 0.06$ (where the uncertainty is determined as $1/\sqrt{12N}$, per Longair 1978), suggesting that the uncorrected sample is severely incomplete. For a weighted average V/V_{max} , where each galaxy is weighted by the inverse of the probability that it would be detected by the APM, the average rises to $\langle V/V_{max} \rangle = 0.44 \pm 0.06$. The selection function depicted in Figure 2.3 therefore substantially accounts for the incompleteness in the survey. The corrections become very large for $\mu_B(0) > 24.5$ mag arcsec⁻² and $r_{scl} < 5$ arcsec, or for $\mu_B(0) > 25.5$ mag arcsec⁻² at any scale

length, so to be conservative we claim the corrected survey is essentially complete to the values of $\mu_B(0)$ and r_{scl} that define the 10% completeness contour in Figure 2.3. The “knee” of that contour is at $\mu_B(0) \approx 24.5 \text{ mag arcsec}^{-2}$ and $r_{scl} \approx 10 \text{ arcsec}$, so we adopt those numbers as the characteristic completeness limits of the survey.

2.5 Implications

Figure 2.4 presents the distribution of central surface brightnesses among the LSB galaxies from the LAS list. The open circles show the distribution before application of the bivariate incompleteness correction, and the filled circles show the distribution after the correction. The distribution for the LAS list only is shown, because the SAS list is likely to be contaminated to some extent by background spirals whose measured surface brightnesses are affected by cosmological dimming. Because the survey selection technique actively discriminates against galaxies with $\mu_B(0) < 22 \text{ mag arcsec}^{-2}$, and because the completeness corrections become too large to be reliable at $\mu_B(0) \sim 25 \text{ mag arcsec}^{-2}$, this distribution is reliable only over that limited range $22 \text{ mag arcsec}^{-2} \lesssim \mu_B(0) \lesssim 25 \text{ mag arcsec}^{-2}$. The distribution is monotonically increasing over this entire range.

A debate has continued for some time over the question of whether there are preferred values of central surface brightness for galaxies of different types. Fish (1964) determined that the bright elliptical galaxies in his sample exhibited an average central surface brightness of $\mu_B(0) = 14.8 \pm 0.9 \text{ mag arcsec}^{-2}$. Freeman (1970) claimed the preferred value is $\mu_B(0) = 21.65 \pm 0.3 \text{ mag arcsec}^{-2}$ for 28 spiral galaxies drawn from a sample of 36 NGC objects with published surface photometry. More recently, van der Kruit (1987) obtained a similar result ($\mu_{B_J}(0) =$

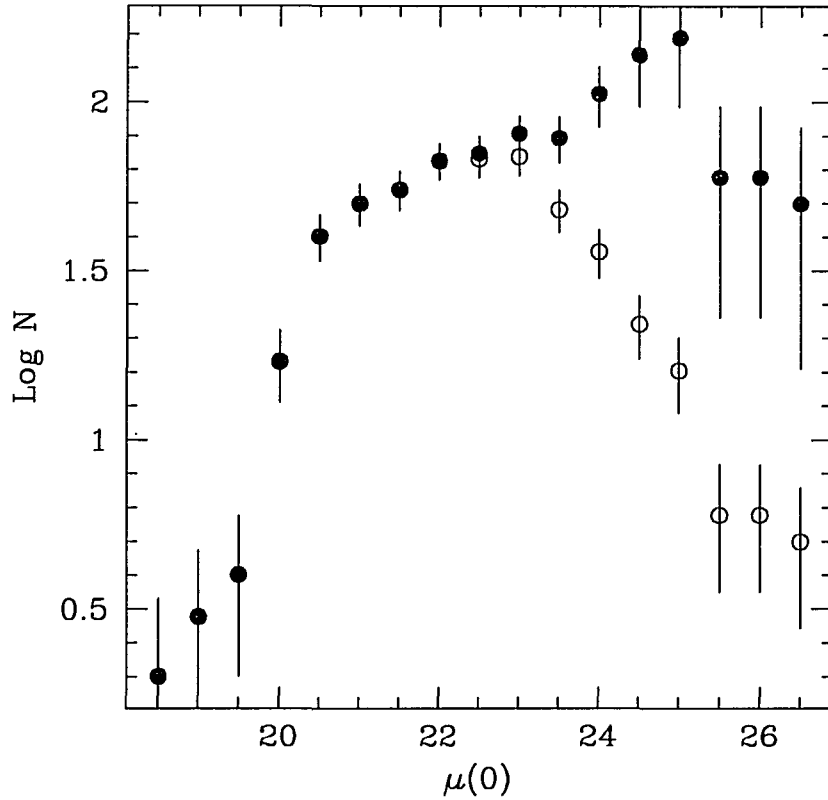


Figure 2.4: Log number of galaxies from the LAS list in the APM survey as a function of central surface brightness. Open circles are before correction for incompleteness, and filled circles are after correction. Error bars reflect counting statistics, and error bars on the filled circles include the effect of the completeness correction.

$21.8 \pm 0.6 \text{ mag arcsec}^{-2}$) from a carefully chosen sample of 40 face-on spiral galaxies from the UGC.

On the other hand, Disney (1976) and Disney & Phillipps (1983) argued that selection effects in photographic surveys could account for the observations of similar central surface brightnesses, and that the limiting isophote of the Palomar Observatory Sky Survey would quantitatively explain the preferred values of 14.8 and $21.65 \text{ mag arcsec}^{-2}$ for ellipticals and spirals, respectively. They contended that, at a given galaxy luminosity, galaxies of both low and high central surface

brightness would tend to be excluded from galaxy surveys, HSB galaxies because they are mistaken for stars, and LSB galaxies because they do not have a large enough angular size at the limiting isophote to be cataloged. Because most galaxy catalogs like the UGC are compiled from visual inspections of the POSS plates, samples drawn from such a catalog, such as the sample of van der Kruit (1987), are biased towards finding a mean $\mu_B(0) \approx 21.8 \text{ mag arcsec}^{-2}$.

Bosma & Freeman (1993) tested the selection-bias argument by examining a sample of galaxies drawn from the SRC-J survey plates, which have a fainter limiting isophote than the POSS. They argued that, if Disney (1976) were correct, then a galaxy sample from the SRC-J survey should have a fainter average central surface brightness than a sample drawn from the POSS. They identified several hundred galaxies with diameters $\gtrsim 2 \text{ arcmin}$ on the SRC-J survey plates, then measured the apparent diameters (at the limiting isophotes) of these same galaxies on the SRC-J, ESO-B, and POSS blue survey materials. By combining the ratios of the apparent diameters on the different surveys with independent knowledge of the limiting isophotes of the different survey materials, they were able to estimate the central surface brightnesses of the galaxies. They found that 55% of the galaxies had diameter ratios consistent with a mean central surface brightness of $21.65 \text{ mag arcsec}^{-2}$, with an intrinsic scatter of $0.5 \text{ mag arcsec}^{-2}$. They also found that 26% of the galaxies had low diameter ratios that were best explained as evidence of a sharp cut-off in disk radial surface brightness profiles, and that 19% of the galaxies had high ratios indicative of low central surface brightness. They concluded that these results were inconsistent with Disney's notion that the limiting isophote of the survey material biased the measured distribution of central surface brightnesses.

There are two aspects of the study of Bosma & Freeman (1993) that call into

question their conclusion that selection effects are not important. First, they give no indication of how they selected galaxies, except by saying that the major diameter was required to be > 2 mm on the SRC-J plates. Given the large area covered ($-32^\circ < \delta < -18^\circ$) and the relatively small numbers of galaxies used (222 for the POSS-SRC comparison and 520 for the ESO-SRC comparison), it is highly unlikely that their list of galaxies is complete, and they make no claims that it is. It is possible that they simply selected the most prominent galaxies, which is exactly the selection technique that Disney (1976) demonstrated would produce a biased result. Second, their distribution of diameter ratios shows a long tail of galaxies with large ratios (*i.e.*, low central surface brightness). Taking a simple number-weighted average across their entire distribution gives an average ratio of 1.51, which implies an average central surface brightness of $\langle \mu_B(0) \rangle = 22.7 \text{ mag arcsec}^{-2}$. Disney & Phillipps (1983) predicted that galaxies identified from the POSS materials would have $\langle \mu_B(0) \rangle = 21.8 \text{ mag arcsec}^{-2}$; application of that method to the fainter limiting isophote of the SRC-J survey yields a predicted average $\langle \mu_B(0) \rangle = 23.4 \text{ mag arcsec}^{-2}$. The $\langle \mu_B(0) \rangle$ of Bosma & Freeman (1993) is therefore closer to the value predicted by Disney & Phillipps (1983) than it is to the mean value of Freeman (1970).

If spirals did obey a gaussian distribution of mean $\langle \mu(0) \rangle = 21.65$ and $\sigma = 0.5$, then our survey (which is dominated by galaxies with exponential luminosity profiles) should show monotonically declining numbers with fainter $\mu_B(0)$ for all $\mu_B(0) > 22 \text{ mag arcsec}^{-2}$. The survey is essentially complete for $22 \leq \mu_B(0) \leq 25$, and the result is clearly the contrary. Figure 2.4 shows that the number of galaxies in the survey increases monotonically as $\mu_B(0)$ gets fainter over the entire range in $\mu_B(0)$ where the completeness corrections are reliable. The results of the present survey are inconsistent with any fixed characteristic value of $\mu_B(0)$ for spiral galaxies, and they are especially inconsistent with the idea that spiral $\mu_B(0)$'s have an

approximately gaussian distribution with a mean of $21.65 \text{ mag arcsec}^{-2}$.

2.6 Conclusions

We have described the process of identifying LSB galaxies from the UKST survey plates using a combination of APM and visual searches. We have measured the apparent magnitudes of the identified LSB galaxies with a typical uncertainty of $\sigma = 0.20 \text{ mag}$ in B , using pixel-to-pixel transformations calibrated by CCD observations of 106 of the LSB galaxies. Through simulations of the APM detection process we have developed a selection function for the APM survey that describes the probability that an LSB galaxy will be included in our catalog as a function of the galaxy's central surface brightness and scale length, and we have demonstrated that this objectively determined selection function substantially corrects for the incompleteness in the catalog. Finally, we have compared the distribution of central surface brightnesses in our catalog to that first described by Freeman (1970), and we have argued that the distribution in our catalog is inconsistent with a gaussian distribution of $\langle \mu_B(0) \rangle = 21.65 \pm 0.5 \text{ mag arcsec}^{-2}$.

Chapter 3

LOW SURFACE BRIGHTNESS GALAXIES AND THE FIELD GALAXY LUMINOSITY FUNCTION

We present luminosity functions for the low surface brightness galaxies identified in the APM survey, and for a combined sample of low surface brightness and high surface brightness galaxies. We find that the luminosity function for the low surface brightness galaxies shows both a steeper faint-end slope and a brighter characteristic luminosity (the M_* or L_* parameter) than the functions determined from other field galaxy surveys. We also find that the overall space density of low surface brightness galaxies is about one-fourth to one-third as great as the density determined from the other surveys' functions, and that the total luminosity density due to these low surface brightness galaxies is about one-third to one-half their level. Previous surveys are therefore missing a substantial fraction of the total number and luminosity density by not accounting for the selection bias against low surface brightness galaxies. These overlooked galaxies are not, however, sufficiently

numerous to account for the discrepancy between the counts of faint blue galaxies observed at moderate redshift and the predictions of no-evolution models based on previous estimates of the local luminosity function. We also find that the density of high luminosity LSB galaxies is as large or larger than the density of luminous galaxies recorded by other field galaxy surveys, and that this high density of luminous LSB galaxies could resolve a recently suggested difference between the number of local luminous galaxies and the number observed at moderate redshift by their association with absorption features in QSO spectra.

3.1 Introduction

The optical luminosity function of galaxies is one of the fundamental building blocks of cosmology. Accurate knowledge of the luminosity function is necessary for, among other things, estimating the mean luminosity density of the universe, and predicting the redshift distribution of objects in various magnitude intervals (see *e.g.*, the review by Binggeli et al. 1988). The shape of the luminosity function also provides an important test for theories of galaxy formation (*e.g.*, Press & Schechter 1974). Further, considerable attention has been focussed of late on the large numbers of blue galaxies found in deep surveys, first described by Tyson (1988). The degree to which number counts of these galaxies exceed those predicted from local observations (*e.g.*, Broadhurst et al. 1988 and Colless et al. 1990), and indeed whether an excess exists at all (compare Koo et al. 1993 and McGaugh 1994), depend on both the shape and the normalization of the luminosity function.

One of the problems with building a galaxy luminosity function is that surveys are limited in the detection of diffuse galaxies by the brightness of the night sky,

and in the detection of compact galaxies by the difficulty in distinguishing stars and galaxies. As Disney (1976) and Disney & Phillipps (1983) have demonstrated, at a given luminosity a survey will identify only those galaxies that have the maximum possible angular size above the limiting isophote. At a constant luminosity, galaxies of high surface brightness (HSB) become indistinguishable from stars, and galaxies of low surface brightness (LSB) fall below the limiting isophote over most of their extent. Although they purport to be magnitude limited, galaxy surveys which do not take account of surface brightness effects are missing an unknown but potentially large number of galaxies in each magnitude bin. Recent surveys of the Virgo cluster by Impey et al. (1988) and of the Fornax cluster by Irwin et al. (1990) and Bothun et al. (1991) have taken account of this potential source of bias by deliberately searching for LSB galaxies. They have found that previous surveys missed a significant fraction of the cluster populations, particularly at fainter luminosities ($M_B \gtrsim -16$), and Impey et al. (1988) determined that inclusion of LSB galaxies in Virgo steepened the low-luminosity tail of that cluster's luminosity function considerably. To date, however, no estimates of the field galaxy luminosity function have addressed the effects of surface brightness bias.

In this chapter, we present the luminosity function for LSB galaxies from the APM survey, and also a luminosity function that combines our set of newly discovered LSB galaxies with a set of previously cataloged HSB galaxies from the same region of the sky. We also review recent suggestions by McGaugh (1994) and by McLeod (1994) that LSB galaxies might account at least partially for the large numbers of faint blue galaxies seen in deep surveys. Section 3.2 describes the survey data and presents the samples used for determining the luminosity function and the corrections applied to those samples. Section 3.3 covers the methods used to develop the luminosity functions. Section 3.4 presents the luminosity functions

and reviews the effects of the corrections for incompleteness. Section 3.5 reviews the consequences of this LSB luminosity function for the general field luminosity function and for the question of local counterparts to the faint blue galaxies. Finally, Section 3.6 summarizes our conclusions. Throughout this chapter, we assume $H_0 = 100 h_{100} \text{ km s}^{-1} \text{ Mpc}^{-1}$. Also, all magnitudes and surface brightnesses used here are in the Johnson B band.

3.2 Samples Used

The APM survey for LSB galaxies is presented by Impey et al. (1995), and Chapter 2 describes the details of how LSB galaxies were identified and calibrated. We briefly summarize the pertinent points here. Twenty-four plates from the UK Schmidt Telescope, covering about 786 square degrees of sky, were searched for LSB objects using both visual and machine scans. The visual search allowed considerable flexibility in identifying interesting galaxies with significant LSB features, and the machine scan ensured a verifiable degree of completeness within certain simply defined limits of size and surface brightness. The combined list was carefully reviewed to eliminate plate flaws, Galactic cirrus, and other interlopers. The digitized APM scans of the galaxies were then used for photometric measurements after calibration as described in Chapter 2. A selection function is developed in Chapter 2 that gives the completeness of the survey as a function of galaxy central surface brightness and scale length (hereafter, “the APM selection function”).

We conducted followup optical spectroscopy at the Multiple Mirror Telescope¹

¹The Multiple Mirror Telescope is a facility jointly operated by the Smithsonian Institution and the University of Arizona.

and 21 cm H I spectroscopy at Arecibo Observatory² to obtain radial velocities for as many of the LSB galaxies as possible. To date we have measured recessional velocities for 332 of the 693 galaxies on the list, of which about half come from H I spectroscopy and half from optical spectroscopy. These heliocentric velocities are presented in Impey et al. (1995). For developing the luminosity function, we have further corrected these heliocentric velocities for Galactic rotation, using the standard correction $v_{corr} = v_{hel} + 300 \sin l \cos b$. No correction was applied for Virgocentric infall since the median velocity of the sample places most of the galaxies well beyond the Local Supercluster. These corrected velocities were then used to estimate distance moduli using the relation:

$$m - M = 5 [\log v_{corr} - \log H_0 + 5] \quad (3.1)$$

assuming as noted above that $H_0 = 100 \ h_{100} \text{ km s}^{-1} \text{ Mpc}^{-1}$.

The galaxies with velocities do not form a random subset of the overall survey. For reasons of observational efficiency, like all other galaxy surveyors we favored galaxies of higher central surface brightness and larger angular size. Figure 3.1 shows the distributions of central surface brightness and half-light radius for the complete sample and for the subset with velocities, along with the ratios of the two sets by bin. We assume that the galaxies for which we have measured redshifts are representative of all galaxies in a given bin of surface brightness and angular size. This additional source of bias must be taken into account in preparing a luminosity function. We have parameterized this bias in the simple forms depicted in Figure 3.1:

²The Arecibo Observatory is part of the National Astronomy and Ionosphere Center. The NAIC is operated by Cornell University under a cooperative agreement with the National Science Foundation.

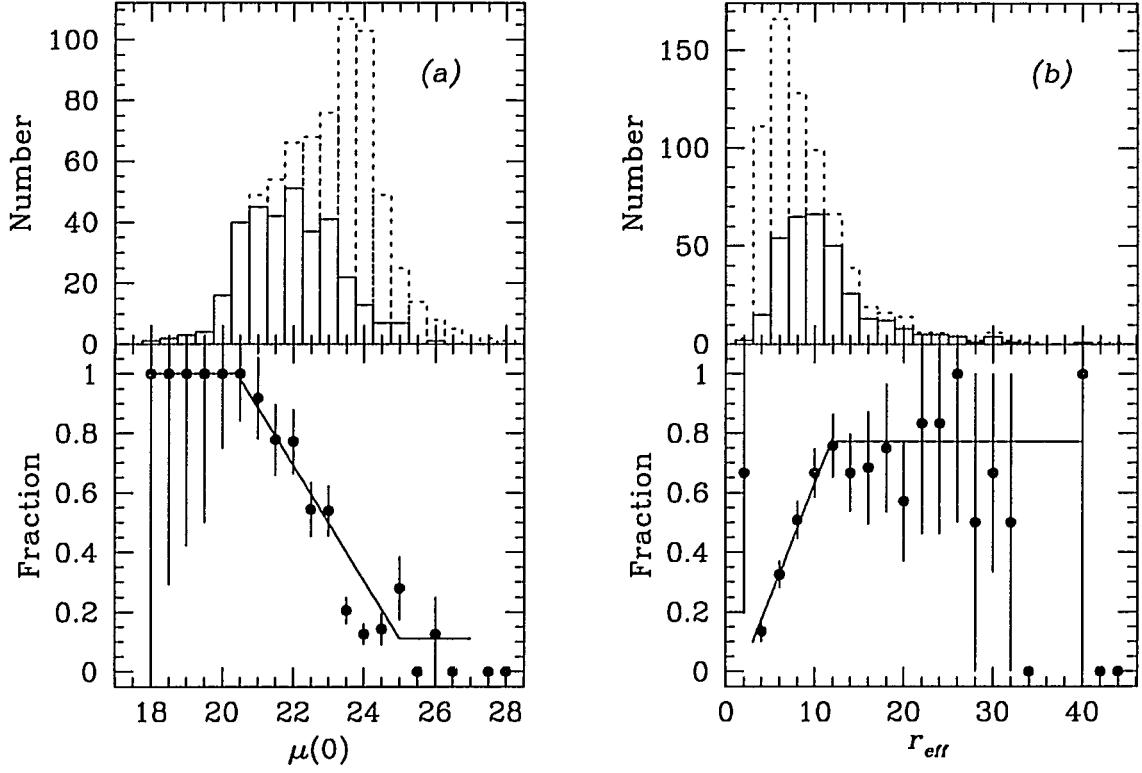


Figure 3.1: Structural properties of the complete LSB sample and the subset with radial velocities. (a) shows the distribution as a function of B central surface brightness, and (b) shows the distribution as a function of half-light radius. In the upper panels, the dotted histogram is the distribution of the complete sample, and the solid histogram is the distribution of the subset with velocities. In the lower panels, the filled circles show the fraction of galaxies with velocities for each bin, with error bars from counting statistics. The solid lines show the parametrizations described in the text.

three separate linear fits in the different regions of the $\mu(0)$ distribution

$$p_\mu = \begin{cases} 1.000, & \mu(0) < 20.25 \\ 4.950 - 0.194 \mu(0), & 20.25 \leq \mu(0) \leq 25.0 \\ 0.111, & \mu(0) > 25.0 \end{cases} \quad (3.2)$$

where $\mu(0)$ is in mag arcsec^{-2} , and in the different regions of the r_{eff} distribution

$$p_{r_e} = \begin{cases} 0.667, & r_{eff} < 3 \\ -0.130 + 0.076 r_{eff}, & 3 \leq r_{eff} \leq 13 \\ 0.773, & r_{eff} > 13 \end{cases} \quad (3.3)$$

where r_{eff} is in arcsec. The final probability that an LSB galaxy will be detected by the APM and included in the subset with velocities is given by

$$p_{tot} = p_{APM} \times p_\mu \times p_{r_e} \quad (3.4)$$

where p_{APM} is the probability derived from the APM selection function.

We can estimate the completeness of our sample of galaxies using the $\langle V/V_{max} \rangle$ test of Schmidt (1968). For the complete set of 693 LSB galaxies, the test yields $\langle V/V_{max} \rangle = 0.15 \pm 0.04$ with no corrections for incompleteness, and $\langle V/V_{max} \rangle = 0.44 \pm 0.06$ after correcting for incompleteness using the APM selection function described in Chapter 2. For the subset of 332 LSB galaxies with velocities, the test gives $\langle V/V_{max} \rangle = 0.04 \pm 0.05$ with no corrections for incompleteness, $\langle V/V_{max} \rangle = 0.34 \pm 0.07$ after applying just the APM selection function, and $\langle V/V_{max} \rangle = 0.50 \pm 0.07$ after applying the APM selection function and the further correction for incompleteness in the velocity observations from Equations 3.2, 3.3, and 3.4 (as depicted in Figure 3.1). The corrections thus substantially remove the incompleteness in both the complete LSB set and in the subset chosen for spectroscopy.

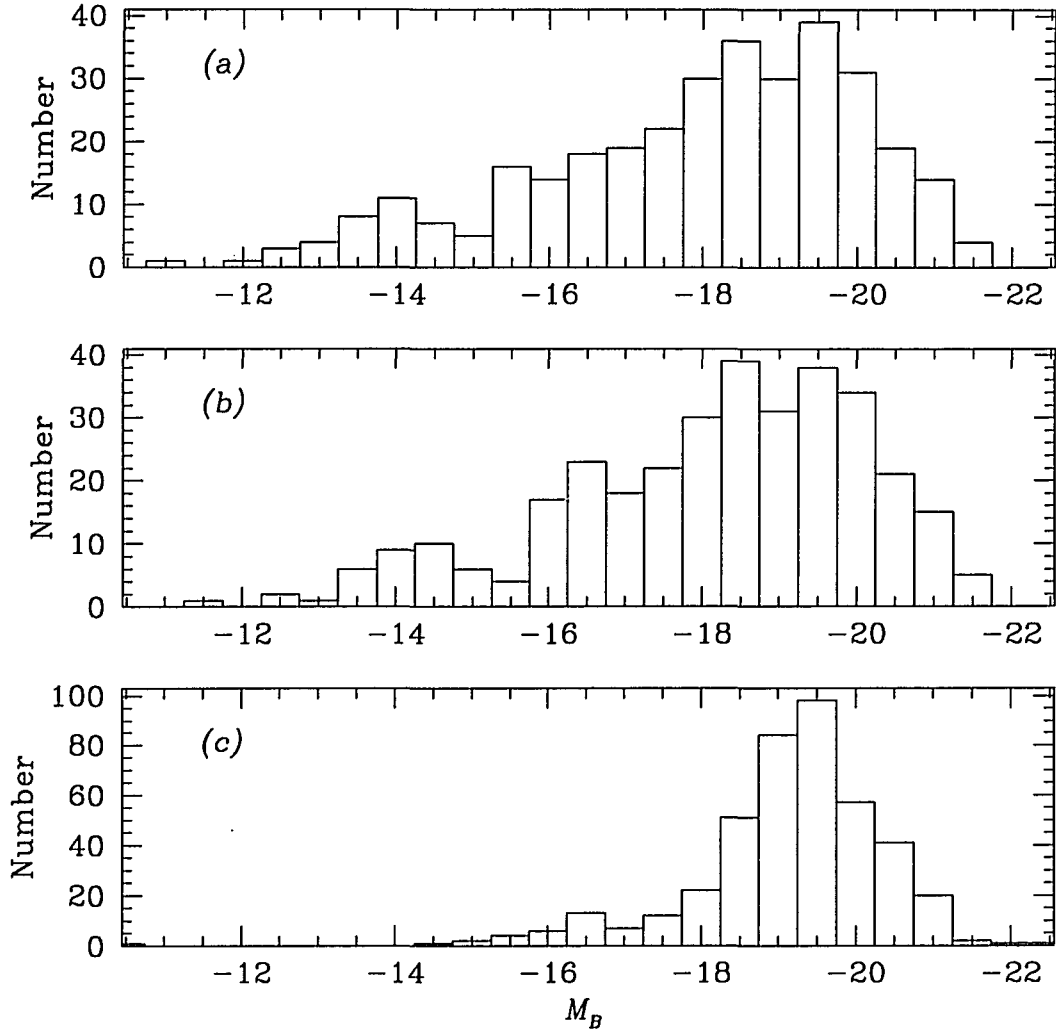


Figure 3.2: Distribution of absolute magnitudes for the LSB and ZCAT galaxies. Panel (a) shows the distribution for the LSB galaxies before correction for the difference between isophotal and total magnitudes, and Panel (b) shows the distribution for the LSB galaxies after correction. Panel (c) shows the distribution for the galaxies drawn from ZCAT as described in the text, with no correction for the difference between isophotal and total magnitudes.

There is yet another source of bias to be found in the magnitudes measured for the LSB galaxies. The magnitudes measured for the LSB galaxies are isophotal magnitudes, or apparent magnitudes measured within the limiting isophote of the detection system, which is $\mu_{lim} \approx 26 \text{ } B \text{ mag arcsec}^{-2}$ in the case of the APM survey. As McGaugh (1994) pointed out, use of isophotal magnitudes will cause galaxy luminosities to be underestimated, and the underestimation becomes more severe with decreasing central surface brightness. Most LSB galaxies are well-described by exponential surface brightness profiles (Impey et al. 1988, Bothun et al. 1991, and McGaugh & Bothun 1994) of the form

$$\mu(r) = \mu(0) + 1.086 \frac{r}{l} \quad (3.5)$$

where $\mu(0)$ is the central surface brightness in mag arcsec^{-2} and l is the exponential scale length in arcsec. This simple analytical form allows a direct calculation of the ratio of the total galaxy flux to that observed within the limiting isophote, as

$$\frac{F_{obs}}{F_{tot}} = 1 - (1 + n_l)e^{-n_l} \quad (3.6)$$

where n_l is the number of scale lengths l observed within the limiting isophote. This simple approximation will clearly understate the ratio for galaxies with central condensations, such as spirals with bulges. As McGaugh (1994) noted, the isophotal aperture in units of the galaxy scale length is given by

$$n_l = \frac{\mu_{lim} - \mu(0) - 10 \log(1 + z) - k(z)}{1.086} \quad (3.7)$$

where μ_{lim} is the surface brightness of the limiting isophote. The first term involving z accounts for the $(1 + z)^4$ cosmological dimming in surface brightness, and the second corrects for the redshifting of the galaxy's spectral energy distribution (the k correction). The k correction of course depends on galaxy type as well as redshift. The magnitudes and surface brightness for the LSB galaxies with velocities have

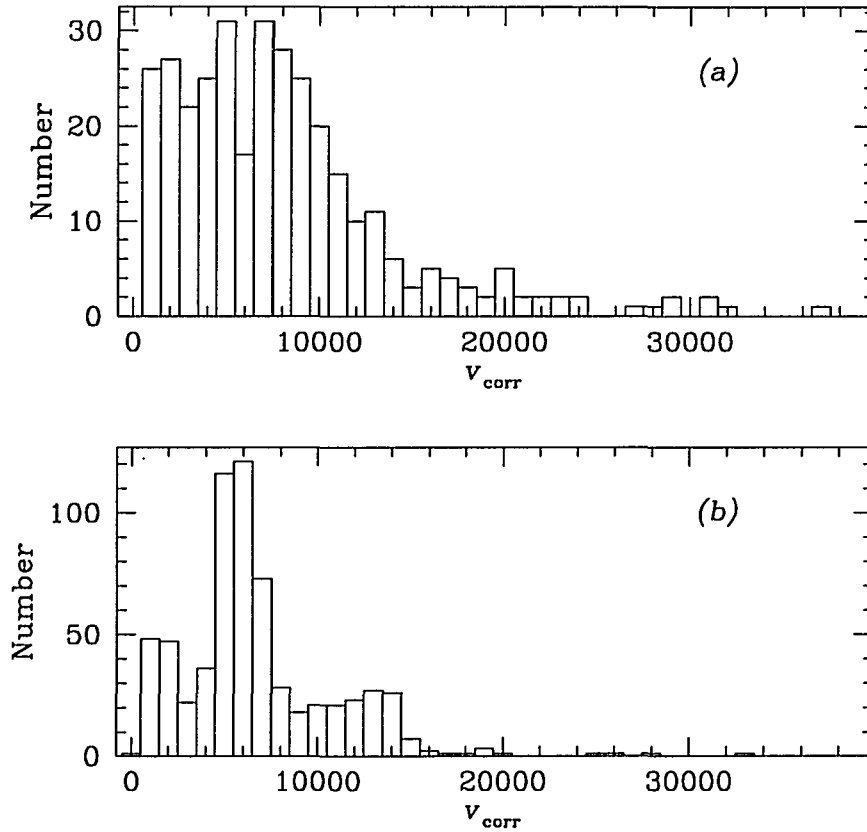


Figure 3.3: Distribution of galaxy radial velocities for the LSB sample (in Panel (a)) and the sample drawn from the ZCAT (in Panel (b)). The horizontal axis is the velocity corrected for Galactic rotation, in km s^{-1} .

been corrected as described in Chapter 2 using the tabulated k corrections of Coleman et al. (1980). The $B-V$ and $V-R$ colors for galaxy types Sbc, Scd, and Irr closely match the range of colors observed among the LSB galaxies for which we obtained CCD photometry. The absolute magnitudes for the LSB galaxies have been corrected according to Equations 3.7 and 3.6, so as to avoid skewing the luminosity function by this tendency to underestimate galaxy luminosities. Figure 3.2 shows the distribution of absolute magnitudes for the LSB galaxies before and after this correction.

Of course, our set of LSB galaxies is not itself a fair sample of the local galaxy

population, precisely because it excludes most galaxies with $\mu(0) \lesssim 21 \text{ mag arcsec}^{-2}$. In order to have a more representative sampling of all surface brightnesses, we culled from the Center for Astrophysics Redshift Catalog (hereafter “ZCAT”) galaxies in the same regions of the sky covered by the APM survey for LSB galaxies, using the version of ZCAT available through the NASA Astrophysics Data System Version 4.0 as of August 1994. ZCAT includes information from a wide variety of sources, from relatively shallow wide-angle surveys to deep pencil-beam studies. The sampling of galaxies by ZCAT is therefore quite uneven, both in position and in velocity. To reduce the effects of this uneven sampling, we limited the search to those galaxies with apparent magnitudes $m_B \leq 15.5$, which is the nominal completeness limit of the extension of the Center for Astrophysics redshift survey (Marzke et al. 1994b). To improve the comparability with our LSB sample, we further restricted the ZCAT list to those galaxies with corrected velocities $v_{corr} \leq 38000 \text{ km s}^{-1}$, which is the highest velocity of any galaxy in our LSB sample. Finally, we excluded 11 galaxies from the ZCAT list that had positions and velocities close enough (position difference $< 2 \text{ arcmin}$, velocity difference $< 200 \text{ km s}^{-1}$) to any galaxy in the LSB sample to suggest that they might be the same object. These restrictions yielded a list of 647 ZCAT comparison galaxies. Figure 3.3 shows the distribution of radial velocities for the LSB sample and for the galaxies drawn from ZCAT (after application of all the restrictions just described). The $\langle V/V_{max} \rangle$ test applied to the final ZCAT set yields $\langle V/V_{max} \rangle = 0.42 \pm 0.06$, indicating that this list is essentially complete, and that it is quite comparable in completeness to the total LSB sample. Because ZCAT does not list central surface brightnesses, we do not have the information necessary to correct the ZCAT magnitudes using Equations 3.7 and 3.6. Finally, we have restricted both the ZCAT and LSB samples by using only galaxies in the luminosity range $-14 \geq M \geq -22$, which is the range where the two samples overlap. This

restriction eliminated a total of nine galaxies from the two samples. The distribution of absolute magnitudes for the final ZCAT sample is shown in Figure 3.2.

3.3 Methods

The differential luminosity function of field galaxies $\phi(M)dM$ is defined as the function giving, at each absolute magnitude M , the number of galaxies per Mpc^{-3} in the luminosity interval $M + dM/2 \leq M \leq M - dM/2$. The “classical” method (so designated by Binggeli et al. 1988) of estimating this luminosity function was simply to divide the number of galaxies in each absolute magnitude bin by the maximum volume to which galaxies of that absolute magnitude would be visible given the apparent magnitude limit of the survey. This method has the advantage of being automatically normalized, that is, the density of galaxies is directly measured. However, this method assumes that the space distribution of galaxies is homogeneous, an assumption that is known to be wrong at the depth of most galaxy surveys. In a shallow survey, for example, the Local Supercluster represents a significant density enhancement, which will lead the classical method to overestimate the number of faint galaxies relative to the number of luminous ones.

More recent methods, several of which are summarized by Efstathiou et al. (1988), assume instead that the luminosity function is independent of position. Thus, if the number of galaxies in the magnitude interval $(M + dM/2, M - dM/2)$ and in a volume element $d^3\mathbf{x}$ is given by the function $f(M, \mathbf{x})dM d^3\mathbf{x}$, then the luminosity and density functions can be separated as $f(M, \mathbf{x}) = \phi(M)\rho(\mathbf{x})$. This separation allows the development of an estimator in which the spatial dependence factors out. One widely used estimator is the maximum likelihood method developed

by Sandage et al. (1979) (hereafter STY). Their method defines a likelihood function

$$\mathcal{L} = \prod_{i=1}^N p_i \quad (3.8)$$

where N is the number of galaxies in the sample and p_i is the probability that a galaxy with redshift z_i and absolute magnitude M_i is included in a magnitude limited catalog

$$p_i = \phi(M_i)\rho(\mathbf{x}) \bigg/ \int_{M_{\max}(z_i)}^{-\infty} \phi(M)\rho(\mathbf{x})dM \quad (3.9)$$

where $M_{\max}(z_i)$ is the faintest absolute magnitude visible at redshift z_i . As noted above, the density function $\rho(\mathbf{x})$ is now independent of luminosity, and so it can be taken outside the integral and factored out of the equation. The parameters of $\phi(M)$ can then be estimated by maximizing the value of the likelihood \mathcal{L} with respect to those parameters. We follow STY and virtually all other users of this method by parametrizing the luminosity function in the form first proposed by Schechter (1976), which is written in absolute magnitudes as

$$\phi(M)dM = 0.4 \ln 10 \phi_* \left[(10^{0.4(M_* - M)})^{1+\alpha} e^{-(10^{0.4(M_* - M)})} \right] dM \quad (3.10)$$

The STY method then yields the values of α and M_* that give the maximum value of \mathcal{L} .

The observed luminosity function is a convolution of the true luminosity function with the magnitude error distribution (Efstathiou et al. 1988; Marzke et al. 1994b). The error distribution in m for objects with CCD photometry is slightly skewed, because m is a logarithmic quantity, but the deviation from a Gaussian is small, because the relative size of the errors in intensity (the linear quantity) is also very small. For the objects with photometry obtained from the APM scans, the errors in m are obtained directly from the external scatter in magnitudes among the calibration galaxies, as described in Chapter 2; this process yields a symmetric

error distribution. Assuming a Gaussian error distribution, the observed luminosity function is

$$\phi_{obs}(M) = \frac{1}{\sigma_M \sqrt{2\pi}} \int_{-\infty}^{\infty} \phi_{true}(M') e^{-(M'-M)^2/2\sigma_M^2} dM' \quad (3.11)$$

To determine the parameters of the true luminosity function, this convolved function is used in the likelihood equations. We assume a fixed dispersion $\sigma_M = 0.20$ mag. This is the weighted average uncertainty developed in Chapter 2 for the LSB galaxy magnitudes. For the ZCAT galaxies, we adopt the value of $\sigma_M = 0.35$ mag used by Marzke et al. (1994b) for the CfA redshift survey galaxies.

Among the advantages of the STY method are that maximum likelihood estimators have well-defined asymptotic error properties. Errors may be estimated simply by finding the ellipsoid of parameter values defined by

$$\ln \mathcal{L} = \ln \mathcal{L}_{max} - 0.5 \chi_{\beta}^2(N_f) \quad (3.12)$$

where $\chi_{\beta}^2(N_f)$ is the β -point of the χ^2 distribution with N_f degrees of freedom. Also, the estimator is continuous, so the data need not be binned. The STY method also has drawbacks. First, because a parametrized model of the function $\phi(M)$ must be assumed, there is no independent check of the goodness-of-fit of the assumed model. Second, because the density factor cancels out of Equation 3.9, a separate estimate of the normalization is necessary to recover the complete luminosity function. Third, the estimator is biased; galaxies with the smallest probabilities of inclusion will dominate the product in Equation 3.8. When the probabilities are determined via Equation 3.9, the most luminous galaxies will therefore dominate the determination of both M_* and α .

Efstathiou et al. (1988) (hereafter EEP) addressed the first problem by introducing a model-independent estimator for the luminosity function. They

simply parametrized the luminosity function as N_p steps $\phi(M) = \phi_k$, where $M_k - \Delta M/2 \leq M \leq M_k + \Delta M/2$ and $k = 1, \dots, N_p$. Then, in a manner analagous to Equations 3.8 and 3.9, the likelihood function can be written as

$$\ln \mathcal{L} = \sum_{i=1}^N W(M_i - M_k) \ln \phi_k - \sum_{i=1}^N \ln \left\{ \sum_{j=1}^{N_p} \phi_j \Delta M H(M_{\max(z_i)} - M_j) \right\} + \text{const} \quad (3.13)$$

where N is the total number of galaxies in the sample, N_p is the number of steps, $M_{\max(z_i)}$ is the maximum (*i.e.*, the faintest) absolute magnitude visible at z_i , and the window functions are

$$W(x) = \begin{cases} 1, & |x| \leq \Delta M/2 \\ 0, & \text{otherwise} \end{cases} \quad (3.14)$$

and

$$H(x) = \begin{cases} 0, & x < -\Delta M/2 \\ (x/\Delta M + 1/2), & |x| \leq \Delta M/2 \\ 1, & x > \Delta M/2 \end{cases} \quad (3.15)$$

There is an implied sum over the doubled index k in the first term of Equation 3.13. Maximizing the likelihood with respect to the ϕ_k yields the following equation, which can be solved iteratively for the ϕ_k

$$\phi_k \Delta M = \frac{\sum_{i=1}^N W(M_i - M_k)}{\sum_{i=1}^N \left\{ H(M_{\max(z_i)} - M_k) / \sum_{j=1}^{N_p} H(M_{\max(z_i)} - M_j) \phi_j \Delta M \right\}} \quad (3.16)$$

The uncertainties the N_p parameters ϕ_k may be determined from the information matrix described by EEP, which can then be inverted to become the covariance matrix.

This stepwise maximum likelihood (hereafter SWML) method provides an independent measure of the quality of the parametrization obtained through some other method such as that of STY. As EEP describe, the SWML can be used to

obtain a likelihood ratio $\ln(\mathcal{L}_1/\mathcal{L}_2)$ that quantifies the goodness-of-fit of the STY parametrization. However, if Equation 3.8 is used directly to compute \mathcal{L}_1 , the likelihood ratio can become meaningless, because \mathcal{L}_2 is sensitive to the choice of bin widths, but \mathcal{L}_1 is not. A meaningful likelihood ratio test can be devised which compares \mathcal{L}_2 derived from the data via the SWML to a value for \mathcal{L}_1 computed from Equation 3.13 with the parameters ϕ_k computed using the STY Schechter parametrization in the following equation, in the limit $\Delta M \rightarrow 0$

$$\phi_k = \int_{M_k+\Delta M/2}^{M_k-\Delta M/2} \phi_{\text{STY}}^2 10^{0.6M} dM \bigg/ \int_{-\Delta M/2}^{\Delta M/2} \phi_{\text{STY}} 10^{0.6M} dM \quad (3.17)$$

With \mathcal{L}_1 determined this way, the likelihood ratio $2\ln(\mathcal{L}_1/\mathcal{L}_2)$ is distributed asymptotically as χ^2 with $N_p - 3$ degrees of freedom, as EEP demonstrated through extensive Monte Carlo simulations.

Both the STY and SWML methods require a separate normalization because the density function cancels out of both likelihood estimators. The most straightforward determination of the normalization ϕ_* is based on an unbiased, minimum variance estimator of the mean space density of galaxies derived by Davis & Huchra (1982). For galaxies having absolute magnitudes in the range $M_1 < M < M_2$, a selection function can be defined as

$$S(x) = \int_{\max[M_{\max(x)}, M_2]}^{M_1} \phi(M) dM \bigg/ \int_{M_2}^{M_1} \phi(M) dM \quad (3.18)$$

where $M_{\max(x)}$ is the maximum (*i.e.*, the faintest) absolute magnitude visible at distance x according to the apparent magnitude limit of the catalog. The mean density of galaxies is then simply

$$\langle n \rangle = \frac{1}{V} \sum_{i=1}^N \frac{1}{S(x_i)} \quad (3.19)$$

where the sum extends over all the galaxies in volume V . EEP showed that the Schechter function normalization ϕ_* can be obtained directly from the mean density

as

$$\phi_* = \frac{\langle n \rangle}{\Gamma(\alpha + 1, 10^{0.4(M_* - M_2)}) - \Gamma(\alpha + 1, 10^{0.4(M_* - M_1)})} \quad (3.20)$$

where Γ is the Euler incomplete gamma function.

Both the STY method and the SWML method assume that the galaxy catalog in use is magnitude limited, *i.e.*, the probability of a galaxy's inclusion in the catalog is completely described by Equation 3.9 or by its stepwise analog. These equations are still applicable in the case where all galaxies with $m < m_{lim}$ have the same probability ($p < 1$) of being included in the catalog, as in the case of a redshift survey that uniformly samples a magnitude-limited catalog with $1/n$ sampling. In our case, however, each galaxy has a unique probability of inclusion that is determined from Equation 3.4, so the given forms of the STY and SWML methods require modification. Zucca et al. (1994) recently addressed this problem. They derived a simple modification to the STY estimator in Equation 3.8 that accounts for the unique observation probability assigned to each galaxy:

$$\mathcal{L} = \prod_{i=1}^N p_i^{w_i} \quad (3.21)$$

where the weight w_i is defined as the inverse of the probability that the i th galaxy will be included in the sample (*i.e.*, for our situation $w_i = 1/p_{tot,i}$, with $p_{tot,i}$ from Equation 3.4), and p_i is as defined in Equation 3.9. The corresponding change to the SWML estimator of Equation 3.13 immediately yields

$$\ln \mathcal{L} = \sum_{i=1}^N W(M_i - M_k) w_i \ln \phi_k - \sum_{i=1}^N w_i \ln \left\{ \sum_{j=1}^{N_p} \phi_j \Delta M H(M_{max(z_i)} - M_j) \right\} + \text{const} \quad (3.22)$$

Finally, the survey biases must also be incorporated into the normalization. This is most directly done by combining the selection function of Equation 3.18 with the combined probability of detecting and spectroscopically observing an LSB galaxy,

from Equation 3.4:

$$S_{tot}(x_i) = S(x_i) \times p_{tot,i} \quad (3.23)$$

Zucca et al. (1994) also estimated the effects of failing to consider the individual galaxy weights. Their simulations revealed that use of Equation 3.9 to determine the Schechter function parameters for a galaxy sample with significant incompleteness ($\langle V/V_{max} \rangle \lesssim 0.3$) would bias the results towards flatter faint-end slopes (*i.e.*, lower absolute values of α) and brighter values of M_* . We can objectively determine individual galaxy weights from parameters of our survey technique (the APM selection function) and from the internal statistics of our followup observations (Figure 3.1 and Equations 3.2 and 3.3), so Equations 3.21 and 3.22 are the clear techniques of choice for our data.

The problem of bias in the STY estimator can be aggravated by this modification. The galaxies for which the survey is most incomplete will have very large weights w_i and hence will dominate the product in Equation 3.21. This bias is also visible in the SWML from Equation 3.22, but its effects will be confined to individual bins. The weights have been limited to reduce the effects of this bias. Because the weights are determined as a function of $\mu(0)$ and r_{eff} , the limits are determined based on the distributions of $\mu(0)$ and r_{eff} : the galaxies in any bin of either variable that contains 3 or fewer galaxies are constrained to have a weight (defined as $1/p_{tot}$, p_{tot} from Equation 3.4) no larger than the largest weight assigned to any galaxy in a more populous bin. In practice, this limit affects only five LSB galaxies out of 332, and the average change in the affected weights is a factor of ≈ 2.5 . The effects of this bias on the SWML estimator can also be exaggerated by choosing bins that are too narrow, so that one or two galaxies can easily dominate the calculation of a single ϕ_k . We have chosen bins 1 mag wide to minimize these

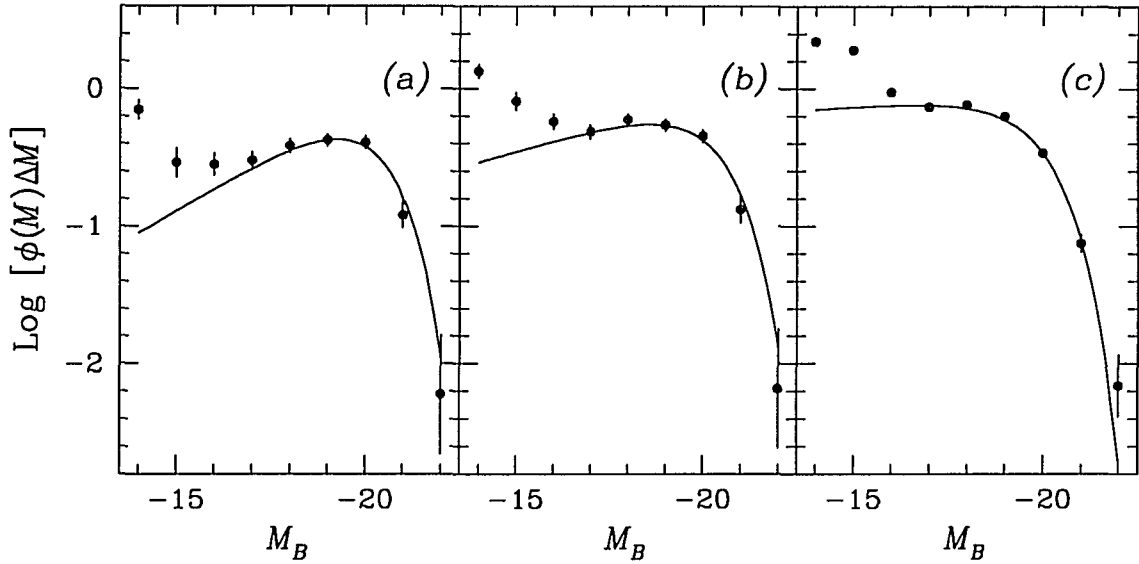


Figure 3.4: Luminosity functions for LSB galaxies with and without completeness corrections. Points are from the SWML method, smooth curves are Schechter functions from the STY method. All functions are arbitrarily normalized to $\phi_* = 1$ for comparison. Panel (a) shows the functions with no corrections for incompleteness, Panel (b) shows the functions with only the corrections from the APM selection function, and Panel (c) shows the functions with full corrections.

extreme effects.

3.4 Results

3.4.1 Effects of the Corrections

Figure 3.4 illustrates the effects of sample incompleteness on the STY and SWML estimators. The points are from the SWML estimates, and the solid curves show the continuous Schechter functions obtained with the STY estimator. Table 3.1 lists the values of α and M_* obtained in each case, and Column (5) gives the probability P from the likelihood ratio test that the stepwise luminosity function is

Table 3.1: Effects of Completeness and Magnitude Corrections

Correction (1)	$\langle V/V_{max} \rangle$ (2)	α (3)	M_* (4)	P (5)
None	0.04 ± 0.05	-0.59 ± 0.15	-20.23 ± 0.40	< 0.0001
APM Only	0.34 ± 0.07	-0.80 ± 0.13	-20.35 ± 0.48	< 0.0001
Full	0.50 ± 0.07	-0.95 ± 0.12	-20.01 ± 0.55	0.0002
Full (no mag corr.)	0.50 ± 0.07	-1.26 ± 0.14	-20.56 ± 0.90	< 0.0001

Notes:

All rows except the last incorporate the isophotal-to-total magnitude correction.
Column(5): P is the probability of the stepwise $\phi(M)$ being accurately described by a Schechter function as given by the likelihood ratio test.

well-described by a Schechter function with those parameters. Figure 3.4(a) shows the results obtained with the raw LSB sample, uncorrected for incompleteness in any way, Figure 3.4(b) shows the results obtained with the LSB sample corrected only for the effects of the APM selection function, and Figure 3.4(c) shows the results from correcting the LSB sample with the full correction of Equation 3.4. As Zucca et al. (1994) noted, incompleteness in the sample tends to bias the maximum-likelihood estimators; each stage of completeness correction increases the densities at the faint end of the function (*i.e.*, raises the absolute value of α), and M_* becomes fainter when the full correction is applied, although the change is not significant. Figure 3.4 also illustrates the tendency of the STY maximum likelihood estimator to be dominated by the bright galaxies. The faint-end slope α is set to provide a good fit to the galaxies around M_* and much less weight is given to the galaxies with $M > -17$.

The luminosity functions shown in Figure 3.4 include the correction from isophotal to total magnitudes set out in Equations 3.6 and 3.7. Figure 3.5 shows

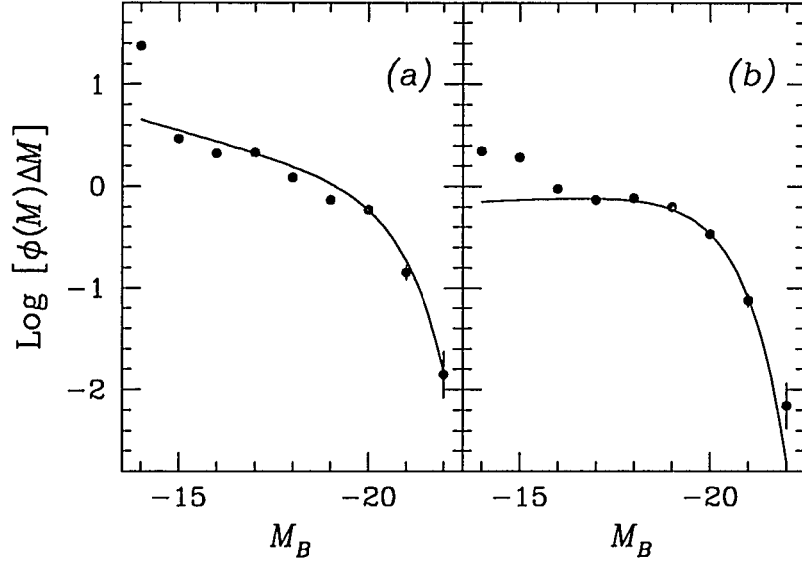


Figure 3.5: Luminosity functions for LSB galaxies without and with magnitude corrections. Points are from the SWML method, smooth curves are Schechter functions from the STY method. All functions are arbitrarily normalized to $\phi_* = 1$ for comparison. Panel (a) shows the function without the magnitude correction, and Panel (b) shows the function with the magnitude correction.

the effect of this correction to total magnitudes (assuming the full correction for incompleteness is applied). This correction has the effect of making the faint end slope less steep (*i.e.*, reducing the absolute value of α) and making M_* fainter. The last row of Table 3.1 lists the Schechter function parameters obtained without these magnitude corrections.

3.4.2 Comparisons with Other Studies

Figure 3.6 shows the luminosity functions of the LSB sample (in (a)), the ZCAT sample (in (b)), and the combined LSB-plus-ZCAT samples (in (c); hereafter, “the Combined sample”). Table 3.2 lists the parameters of the fitted Schechter functions, along with the parameters obtained in three other recent studies. As with Table 3.1,

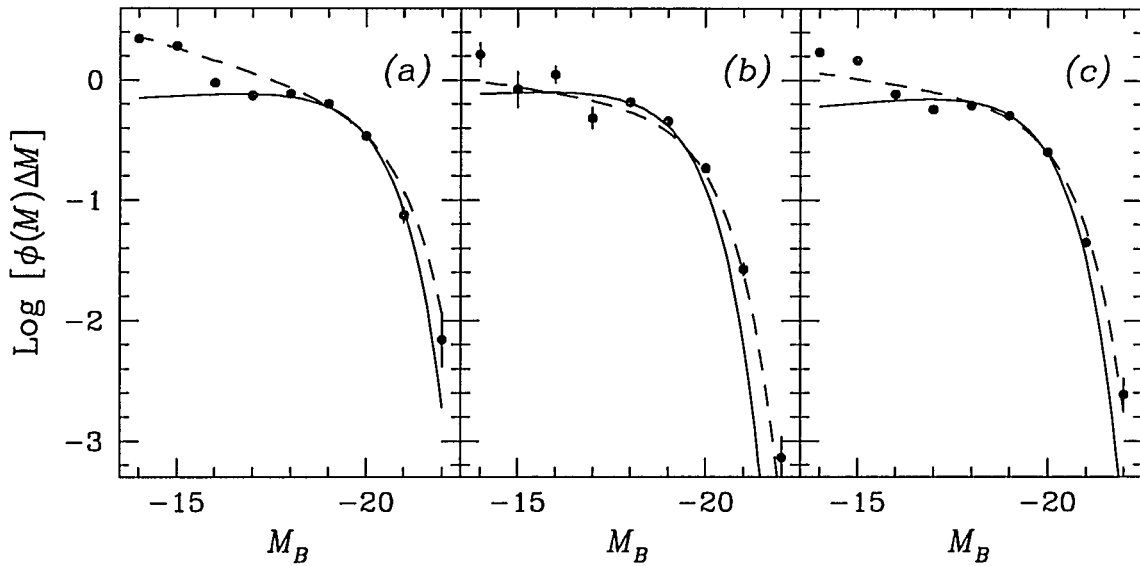


Figure 3.6: Luminosity functions for the LSB, ZCAT and Combined samples. Points are from the SWML method, solid curves are Schechter functions from the STY method, and dashed curves are Schechter functions determined by Levenburg-Marquardt fits to the SWML points. All functions are arbitrarily normalized to $\phi_* = 1$ for comparison. Panel (a) shows the function for the LSB sample, Panel (b) shows the function for the ZCAT sample, and Panel (c) shows the function for the Combined LSB-plus-ZCAT sample.

Column (5) of Table 3.2 gives the probability P that the SWML luminosity function is accurately described by the given Schechter function. The values of α for the LSB, ZCAT, and Combined samples are consistent at the 1σ level, but the value of M_* for the LSB sample is significantly higher than that for the ZCAT sample. Not surprisingly, M_* for the combined sample is midway between the other two. These similarities and differences are illustrated in Figure 3.7, which shows the error contours around the maximum-likelihood Schechter parameters for the three samples. The values of α derived from all three of the present samples are generally consistent with those obtained by the other studies, but there is some deviation among the values of M_* . The M_* value from the LSB sample is at least 1σ brighter than those of EEP, Loveday et al. (1992), or Marzke et al. (1994b), and the M_* for

Table 3.2: Luminosity Functions for LSB, ZCAT and Combined Samples

Sample (1)	α (2)	M_* (3)	ϕ_* (4)	P (5)
LSB (STY)	-0.95 ± 0.12	-20.01 ± 0.55	1.0 ± 0.1	< 0.01
LSB (fit)	-1.24 ± 0.16	-20.63 ± 0.45	1.6 ± 0.1	0.02
ZCAT (STY)	-0.96 ± 0.21	-19.24 ± 0.26	2.1 ± 0.1	0.03
ZCAT (fit)	-1.11 ± 0.22	-19.81 ± 0.36	2.6 ± 0.2	0.28
Combined (STY)	-0.92 ± 0.08	-19.66 ± 0.23	2.4 ± 0.5	0.61
Combined (fit)	-1.11 ± 0.10	-20.12 ± 0.26	2.5 ± 0.2	0.09
Efstathiou et al. 1988	-1.07 ± 0.05	-19.68 ± 0.10	15.6 ± 3.4	0.25
Loveday et al. 1992	-0.97 ± 0.15	-19.50 ± 0.13	14.0 ± 1.7	0.65
Marzke et al. 1994a	-1.02 ± 0.20	-18.90 ± 0.30	20.0 ± 5.0	0.25
Marzke et al. 1994b	-1.00 ± 0.20	-18.80 ± 0.30	40.0 ± 10.0	0.25

Notes:

Column (2): Schechter function parameter α .

Column (3): Schechter function parameter M_* , in B magnitudes for all except Loveday et al., which is in B_J magnitudes.

Column (4): Schechter function normalization in units of $10^{-3} h_{100}^3 \text{Mpc}^{-3} \text{mag}^{-1}$.

Column (5): Probability of the stepwise $\phi(M)$ being accurately described by a Schechter function as given by the likelihood ratio test.

the ZCAT sample is roughly 1σ below the values found by EEP and Loveday et al. (1992), while the M_* derived for the Combined sample here is consistent with those from EEP and Loveday et al. (1992). The M_* value from Marzke et al. (1994b) is $\gtrsim 1\sigma$ fainter than all the others listed.

The most striking differences visible in Table 3.2 are in the normalizations ϕ_* . The ϕ_* values derived by EEP, Loveday et al. (1992), and Marzke et al. (1994a) are all roughly comparable. The values derived here for all three samples are substantially lower. Because the STY estimates of the Schechter parameterizations for the LSB, ZCAT, and Combined samples deviate so markedly from the SWML results at both the high and low luminosity ends, the values reported in Table 3.2

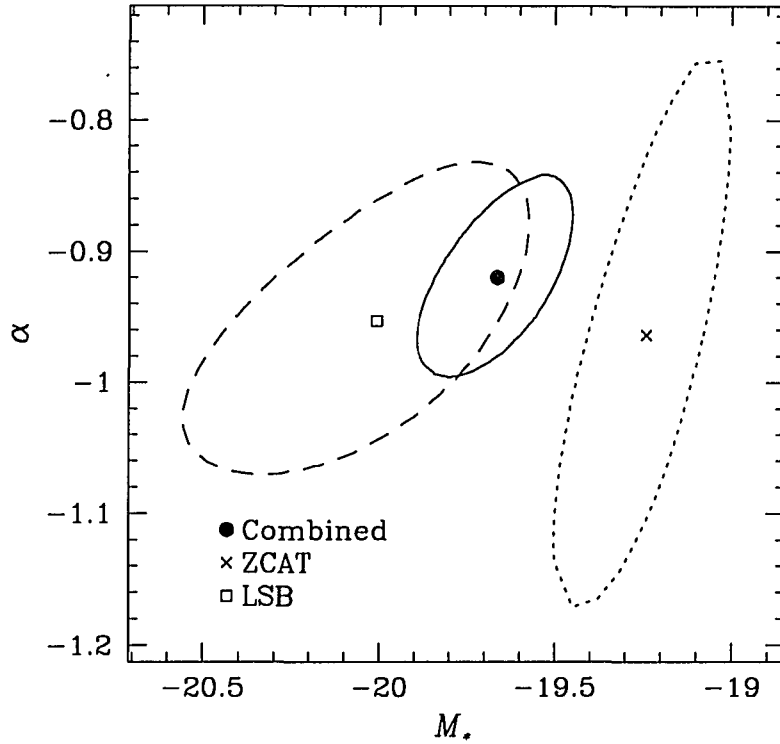


Figure 3.7: Error contours at the 1σ level for the Schechter function parameters as determined by the STY maximum-likelihood method for the LSB, ZCAT and Combined samples.

were determined by substituting discrete sums over the SWML luminosity function for the integrals over smooth Schechter functions in Equation 3.18. The ϕ_* values from EEP, Loveday et al. (1992), and Marzke et al. (1994b) were all computed using integrals over the smooth Schechter parameterization, but this difference in method is not responsible for the differences in the ϕ_* values. When ϕ_* for the LSB, ZCAT, and Combined samples are recomputed using the smooth integrals, the overall results change by only $\approx 30\%$. The differences are most likely due to differences in the shapes of the luminosity functions. The ϕ_* computations in Equations 3.18, 3.19, and 3.20 are sensitive to the values of α and M_* , in that more negative values of α or fainter values of M_* give larger values of ϕ_* . For example,

using the integrals over Schechter functions in Equation 3.18, a change in M_* of only 0.2 mag (to a fainter value) more than doubles the value of ϕ_* for the Combined sample. Similarly, a 20% change in α (to a more negative value) almost doubles ϕ_* for the Combined sample.

The results of the likelihood ratio test indicate that the STY maximum-likelihood Schechter function can be regarded as a reasonable parameterization of the SWML luminosity function only for the Combined sample. The maximum-likelihood Schechter function is not a fair representation of the SWML results for either the LSB or ZCAT sample considered separately. Like the STY maximum-likelihood method, the likelihood ratio test of EEP is most heavily influenced by the galaxies with $M \sim M_*$. These results imply that the STY maximum-likelihood parameterization is a much closer representation of the SWML results in the neighborhood of M_* for the Combined sample than it is for the other two, notwithstanding the deviations that all three show at both the high and low luminosity extremes. These difficulties with the STY maximum-likelihood estimates prompted a second approach to determining Schechter parameterizations, whereby a Schechter function was fit directly to the SWML points using a Levenburg-Marquardt nonlinear fitting routine (hereafter, “LM fits”). These fits are shown as the dashed curves in Figure 3.6, and their parameters are shown on the “(fit)” lines in Table 3.2. For all three samples, the LM fits yielded brighter values of M_* , steeper values of the slope α , and higher values of the normalization ϕ_* . For the LSB and ZCAT samples, the likelihood ratio test indicates that the LM fit is a substantial improvement over the STY parameters, although the STY parameters are still better for the Combined sample. For the rest of this analysis, where a parameterization is necessary we will use the parameterization for each sample that yields the highest probability in the likelihood ratio test: the LM fits for the LSB

and ZCAT samples, and the STY estimates for the Combined sample.

The differences between the luminosity function for the ZCAT sample and the function derived by Marzke et al. (1994b) are disturbing. In particular, the present ZCAT sample shows a brighter M_* and a much lower ϕ_* than the complete catalog analyzed by Marzke et al. (1994b). The most plausible explanation is that the ZCAT sample suffers from subtle incompleteness effects due to the mingling of redshift and magnitude data from many different sources, as noted above. The redshift distribution of the ZCAT sample (see Figure 3.3) shows a sharp peak centered at $\sim 6000 \text{ km s}^{-1}$, and a relatively flat distribution on either side. The peak is at the approximate redshift of the “Great Wall,” suggesting that the ZCAT sample is heavily influenced by large scale structures. The redshift distribution for the LSB sample shows no such peak. If the ZCAT sample is partially volume limited, it would probably be relatively deficient in high luminosity galaxies, since it would not be covering a large enough volume to find many of these rare objects. Such a deficiency would bias the estimate of M_* towards fainter values. If the ZCAT sample is both volume limited and incomplete near the assumed apparent magnitude limit, there would also be a deficiency of low luminosity galaxies. The distribution of absolute magnitudes for the ZCAT sample in Figure 3.2 implies just such a deficiency. These concerns about the ZCAT sample limit its usefulness for the present study. The intention was to combine the LSB sample, which is corrected for surface brightness selection effects but excludes previously known galaxies of (mostly) high surface brightness, with the ZCAT sample, which was hoped would be a complete sample of the type of galaxy excluded from the LSB sample, to obtain a complete, selection-effect-corrected sample from the common region of sky. Unfortunately, the volumes and magnitudes sampled by the two samples are not comparable enough for the combination to be meaningful.

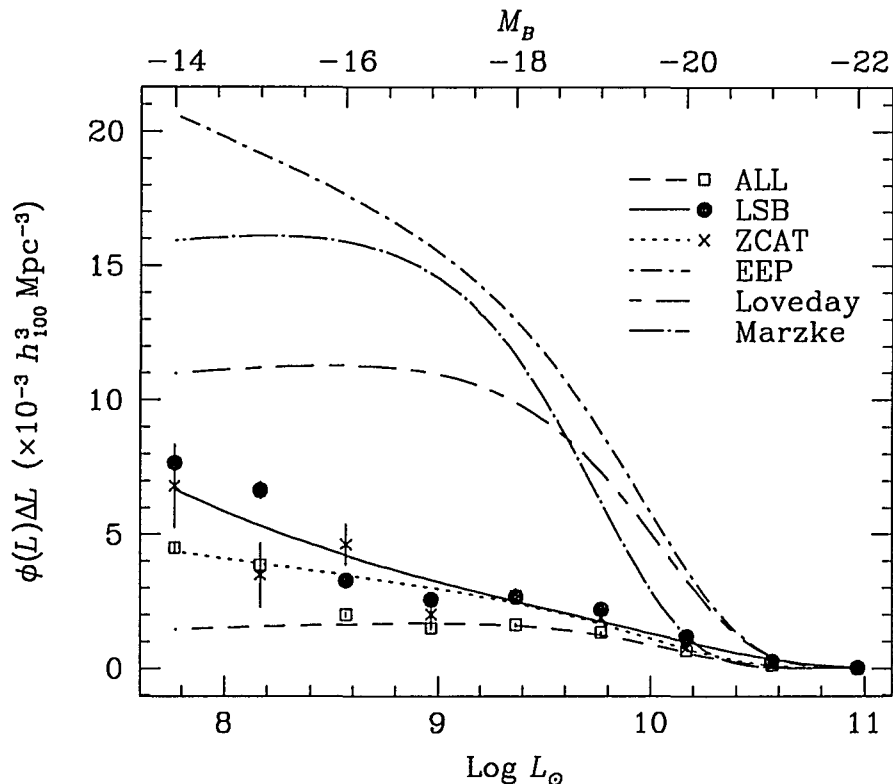


Figure 3.8: Luminosity functions for the LSB, ZCAT, and Combined samples plotted linearly as a function of $\text{Log } L$. The top axis indicates the corresponding absolute B magnitude. The points represent the binned luminosity functions from the SWML method, and the smooth curves show the Schechter parameterizations from the LM fit method for the LSB and ZCAT samples, and from the STY maximum likelihood method for the Combined sample. Schechter functions obtained by Efstathiou et al. 1988, Loveday et al. 1992, and Marzke et al. 1994a are drawn in for comparison.

3.4.3 Number and Luminosity Density of LSB Galaxies

To investigate the fraction of the total galaxy population represented by LSB galaxies, we have computed the integrated number and luminosity densities for the three samples studied here, and compare the results to those from the prior works. The results appear in Table 3.3. The integrated number density of LSB galaxies in our sample, based on the LM fit parameters, is about one-third the density found by Loveday et al. (1992) from the Stromlo-APM redshift survey, and

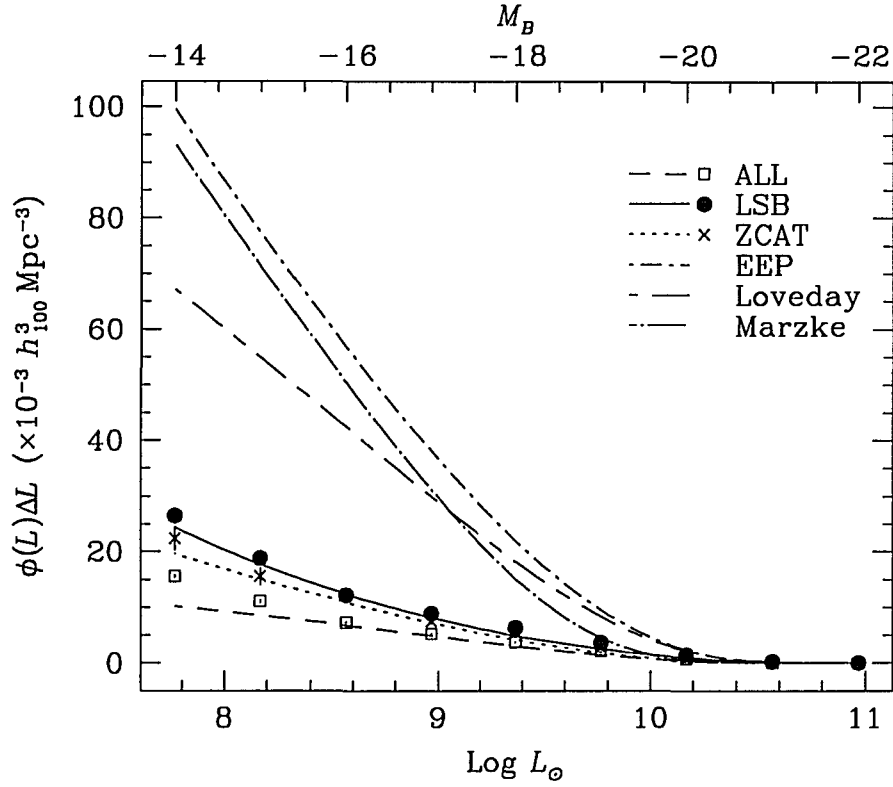


Figure 3.9: Cumulative luminosity functions for the LSB, ZCAT, and Combined samples plotted linearly as a function of $\text{Log } L$. The top axis indicates the corresponding absolute B magnitude. The points represent the binned luminosity functions from the SWML method, and the smooth curves show the Schechter parameterizations from the LM fit method for the LSB and ZCAT samples, and from the STY maximum likelihood method for the Combined sample. Schechter functions obtained by Efstathiou et al. 1988, Loveday et al. 1992, and Marzke et al. 1994a are drawn in for comparison. The summation or cumulation runs from the high luminosity bin to the low luminosity bin, (*i.e.*, from right to left).

Table 3.3: Integrated Number and Luminosity Densities

Sample (1)	Number Density (2)	Luminosity Density (3)
LSB (STY)	8.66 ± 2.28	1.45 ± 0.76
LSB (fit)	26.48 ± 3.53	5.23 ± 1.40
ZCAT (STY)	12.42 ± 2.02	1.52 ± 0.50
ZCAT (fit)	22.40 ± 3.44	3.53 ± 1.08
Combined (STY)	15.59 ± 1.79	2.50 ± 0.58
Combined (fit)	23.72 ± 2.67	4.38 ± 0.98
Loveday et al. 1992	66.96 ± 7.73	14.69 ± 3.38
Marzke et al. 1994a	93.02 ± 19.58	10.82 ± 4.56
Efstathiou et al. 1988	99.27 ± 18.00	19.30 ± 7.0

Notes:

Column (2): Integrated number density in units of $10^{-3} h_{100}^3 \text{ Mpc}^{-3}$.

Column (3): Integrated luminosity density in units of $10^7 h_{100} L_{\odot} \text{ Mpc}^{-3}$.

about one-fourth the density found by Marzke et al. (1994a) and by EEP. The fractions for the ZCAT and Combined samples, again using the LM fit parameters, are roughly comparable. The fractions based on the STY parameter estimates are somewhat lower. These relationships can best be illustrated by plotting the luminosity functions linearly, instead of the customary $\text{Log } \phi$ versus M or $\text{Log } L$ form. Figure 3.8 shows the luminosity functions for the three samples, plotted against $\text{Log } L$ and M , and Figure 3.9 shows the cumulative number densities, where the cumulation runs from the high luminosity bin to the low luminosity bin (*i.e.*, from right to left in Figure 3.9). In both figures, the Schechter functions obtained by Loveday et al. (1992), Marzke et al. (1994a) and EEP are also drawn in for comparison. The cumulative density for the Combined sample is not equal to the sum of the densities from the LSB and ZCAT samples because the three samples were normalized independently, each using the sum over its own SWML luminosity

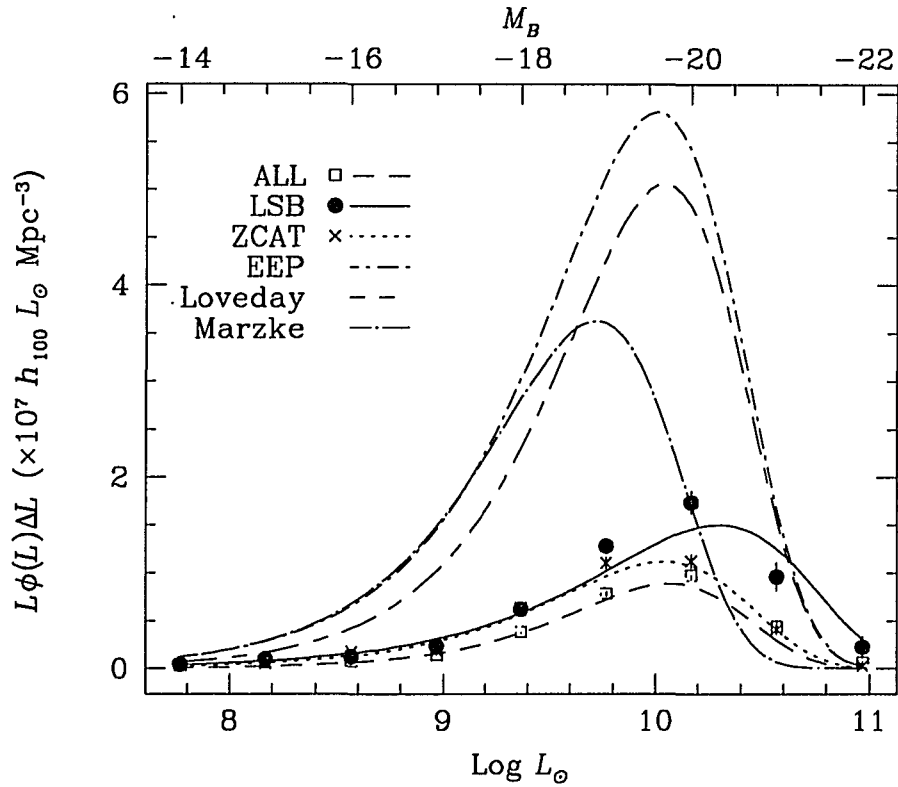


Figure 3.10: Luminosity densities for the LSB, ZCAT, and Combined samples plotted linearly as a function of $\text{Log } L$. The top axis indicates the corresponding absolute B magnitude. The points represent the binned luminosity densities from the SWML method, and the smooth curves show the Schechter parameterizations from the LM fits for the LSB and ZCAT samples and from the STY estimate for the Combined sample. The Schechter functions from Efstathiou et al. 1988, Loveday et al. 1992 and Marzke et al. 1994a are shown for comparison.

function in Equation 3.18. These functions have different shapes, which causes the normalizations to vary as noted above.

Integrated luminosity densities in units of $h_{100} L_{\odot} \text{ Mpc}^{-3}$ were computed for each of the samples from their Schechter function parameters using the equation

$$\langle L \rangle = \phi_* \Gamma(\alpha + 2) L_* \quad (3.24)$$

where L_* is the luminosity corresponding to M_* and Γ is the Euler gamma function.

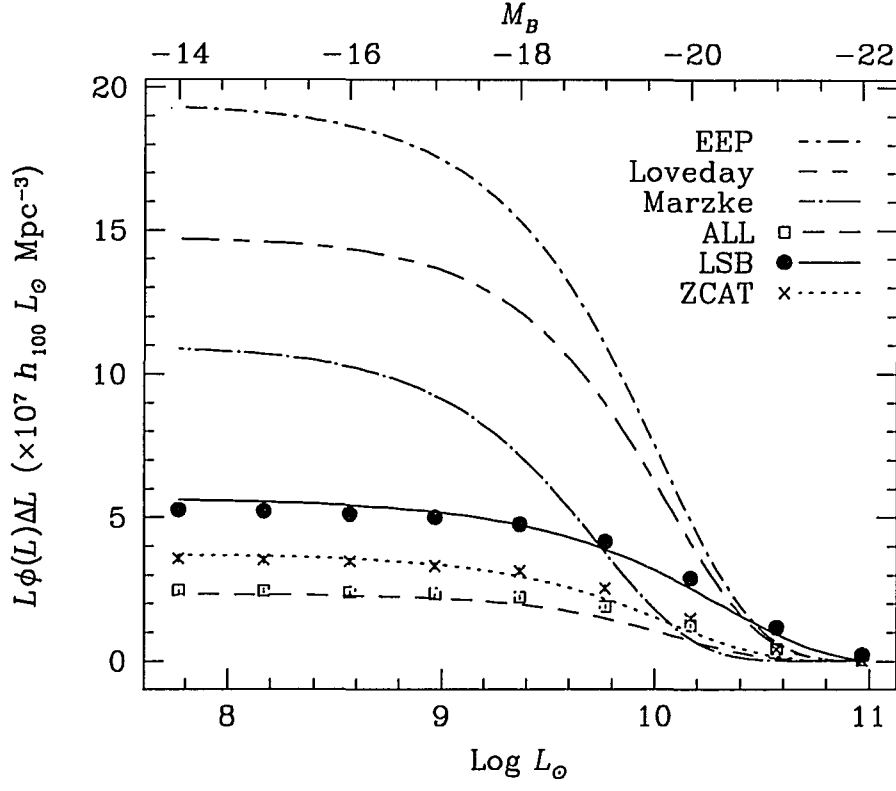


Figure 3.11: Cumulative luminosity densities for the LSB, ZCAT, and Combined samples plotted linearly as a function of $\text{Log } L$. The top axis indicates the corresponding absolute B magnitude. The points represent the binned luminosity densities from the SWML method, and the smooth curves show the Schechter parameterizations from the LM fits for the LSB and ZCAT samples and from the STY estimate for the Combined sample. The Schechter functions from Efstathiou et al. 1988, Loveday et al. 1992 and Marzke et al. 1994a are shown for comparison. The summation or cumulation runs from the high luminosity bin to the low luminosity bin, (*i.e.*, from right to left).

The results appear in Table 3.3. Using the Schechter parameters from the LM fit, the LSB sample represents about one-half the overall luminosity density found by Marzke et al. (1994a), about one-third the density found by Loveday et al. (1992), and about one-fourth the density found by EEP. These comparisons show that the surface brightness selection bias has caused previous field galaxy surveys to miss somewhere between 20% and 35% of the total luminosity density in the local universe. The luminosity densities are depicted in Figure 3.10, which shows the luminosity density as a function of $\text{Log } L$, and Figure 3.11, which shows the cumulative luminosity density as a function of $\text{Log } L$ (as before, the cumulation runs from high to low luminosity). As these figures show, the LSB galaxies account for more total luminosity density among galaxies with $M < -21$ than any other sample. Surface brightness selection biases have therefore caused prior surveys to miss more than half of the very brightest galaxies; these missed galaxies must be relatively large to have high luminosities despite their low surface brightnesses. The importance of properly accounting for surface brightness selection effects is underscored by the fact that a majority of the most luminous galaxies can be missed.

3.4.4 Luminosity Functions by Morphological Type

Both the LSB and Combined samples contain a significant number of low-luminosity galaxies in excess of that predicted by the STY maximum-likelihood Schechter function. The rise in density at the low luminosity bins is responsible for the differences in α between the STY parameterizations and the LM fits. This excess over the STY slope represents a density of galaxies with $M \geq -16$ up to twice the predicted level. Marzke et al. (1994b) noted a similar excess in the CfA survey. The luminosity function derived by EEP did not extend to luminosities fainter

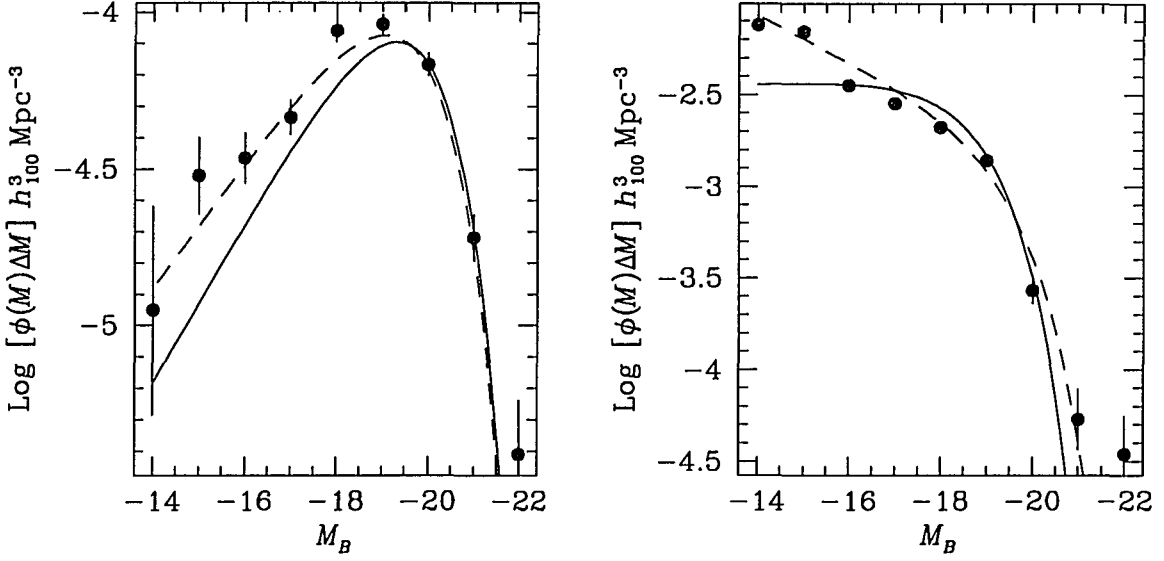


Figure 3.12: Luminosity functions for LSB spiral galaxies (left panel) and LSB irregular galaxies (right panel). The filled circles show the SWML binned luminosity functions, the solid curves represent the STY maximum likelihood estimates of Schechter parameterizations, and the dashed curves represent the LM fits of Schechter functions to the SWML points.

than $M_{B_J} = -17$, and the function of Loveday et al. (1992) extended only to $M_{B_J} = -15.5$, which is approximately where the excess becomes visible in the present work. Neither EEP nor Loveday et al. (1992) noted any excess of faint galaxies like that observed here and by Marzke et al. (1994b). Marzke et al. (1994a) attributed this excess to a very steep faint-end slope among irregular and dwarf galaxies.

Binggeli et al. (1988) demonstrated that different morphological types of galaxies have very different luminosity functions. We have investigated these possible differences for the LSB sample by dividing it into LSB spirals, defined as those galaxies with de Vaucouleurs types $1 \leq T \leq 8$, and LSB irregulars, defined as galaxies with de Vaucouleurs types $T = 9$ or $T = 10$. The total LSB sample (with velocities) is $\approx 50\%$ spirals and $\approx 40\%$ irregulars, with the remainder being

Table 3.4: Luminosity Functions for LSB Galaxies by Morphology

Sample (1)	α (2)	M_* (3)	ϕ_* (4)	P (5)
Spirals (STY)	-0.36 ± 0.26	-19.80 ± 0.5	2.6 ± 3.5	0.99
Spirals (fit)	-0.49 ± 0.10	-19.81 ± 0.2	2.1 ± 2.9	0.98
Irregulars (STY)	-0.97 ± 0.22	-18.96 ± 0.92	11.1 ± 1.6	0.97
Irregulars (fit)	-1.31 ± 0.11	-19.68 ± 0.12	18.4 ± 2.6	0.95
Spirals, Marzke et al. 1994a	$-0.81 \pm \dots$	$-18.76 \pm \dots$	$150.0 \pm \dots$	0.55
Sm-Im Marzke et al. 1994a	$-1.87 \pm \dots$	$-18.79 \pm \dots$	6.0 ± 2.0	0.46

Notes:

Column (2): Schechter function parameter α .

Column (3): Schechter function parameter M_* , in units of B magnitudes.

Column (4): Schechter function normalization in units of $10^{-4} h_{100}^3 \text{ Mpc}^{-3} \text{ mag}^{-1}$.

Column (5): Probability of the stepwise $\phi(M)$ being accurately described by the Schechter function parameters, as given by the likelihood ratio test.

either interacting pairs, dwarf ellipticals, or unclassifiable peculiar morphologies. Figure 3.12 shows the normalized luminosity functions, in the customary $\text{Log } \phi$ versus absolute magnitude format, for the spiral and irregular classes. The solid curves there represent the STY maximum likelihood Schechter functions, and the dashed curves represent the Schechter functions obtained by LM fits to the SWML results depicted by the filled circles. Parameters for the STY maximum likelihood and Schechter functions obtained via LM fits are listed in Table 3.4. According to the likelihood ratio tests, both estimation methods make acceptable representations of the SWML points, despite the disparity in the parameter values. ϕ_* for the irregulars is about five to ten times greater than for the spirals due to the greater weights assigned to the irregulars by the APM selection function. The median central surface brightness for the irregulars is $\approx 1.2 \text{ mag arcsec}^{-2}$ fainter than for the spirals, which would cause them to receive heavier weightings.

The irregular galaxies clearly have a faint-end slope (as determined from the simple fit) that rises significantly more steeply than that of the overall LSB luminosity function. This function is consistent with the luminosity function for field irregulars shown in the review of Binggeli et al. (1988), but their function does not extend to luminosities as high as those found here. This result is also generally consistent with the result obtained by Marzke et al. (1994a) for the higher surface brightness galaxies in the CfA Redshift Survey, although the slope found here ($\alpha = -1.31$) is not so extreme as theirs ($\alpha = -1.87$). This rising faint-end slope accounts for the excess of faint galaxies observed beyond the Schechter function fit to the overall LSB and Combined sample luminosity functions. The LSB spiral galaxies have a faint-end slope that declines rapidly. This trend is generally consistent with the archetypal field spiral luminosity function shown in the review of Binggeli et al. (1988), but Marzke et al. (1994a) found a similarly declining slope in the CfA survey data only for the Sa-Sb subclass. Loveday et al. (1992) found a flat faint-end slope for the spiral galaxies in the Stromlo-APM survey. The declining slope and low normalization suggest that the LSB spiral sample could be incomplete, but a $\langle V/V_{max} \rangle$ test yields $\langle V/V_{max} \rangle = 0.40 \pm 0.06$, so while there is apparently some incompleteness it is not severe.

3.5 Implications

3.5.1 Faint Galaxies

Recent observations have revealed a population of faint blue ($m_{B_J} \lesssim 27$, median $B_J - R \sim 0.6$: Tyson 1988, Efstathiou et al. 1991) galaxies at moderate redshifts (median $z \sim 0.4$, Colless et al. 1990 and Lilly et al. 1991). Given their redshifts, they

are also intrinsically faint, with $M_{B_I} \gtrsim -18$. These galaxies are clustered much more weakly than are local bright galaxies (Efstathiou et al. 1991), and their numbers are significantly in excess (*i.e.*, by a factor of two or three) of expectations based on local galaxy populations in the absence of evolution (Lilly et al. 1991). This excess has lead some authors to suggest non-standard cosmologies as a possible explanation (Yoshii 1993), and others to propose strong evolution in galaxy luminosities, perhaps with the rate of evolution itself a function of luminosity (Broadhurst et al. 1988). Still another approach, taken by Koo et al. (1993), is to derive local luminosity functions by finding functions that can explain as well as possible the faint galaxy number counts without invoking strong evolution; the luminosity functions they derive predict more local low-luminosity galaxies than are observed in existing surveys.

McGaugh (1994) suggested that LSB galaxies such as those in the present sample could be local counterparts to this population of faint blue galaxies (hereafter, FBGs). He noted that, like the FBGs, LSB galaxies are generally blue (McGaugh & Bothun 1994) and weakly clustered (Mo et al. 1994). Furthermore, if current models of slow, continuous star formation LSB galaxies are correct (McGaugh & Bothun 1994), McGaugh (1994) argues that LSB galaxies should become only slightly redder over the timescales of interest, $0 < z \lesssim 0.5$. He also demonstrated through a simple analytic calculation that the deep CCD surveys would be more sensitive to LSB galaxies at $z \sim 0.4$ than wide-field photographic surveys are to local ($z \lesssim 0.1$) LSB galaxies. He argued that including nearby LSB galaxies in the local luminosity function could reconcile the number of low-luminosity galaxies in the local population with the FBG population.

McLeod (1994) addressed this suggestion with a simple model for the local LSB

population. He assumed a spectral energy distribution for LSB galaxies based on the color measurements available from the literature (McGaugh & Bothun 1994), and a luminosity function identical to that of the local HSB galaxies (Loveday et al. 1992). These assumptions yielded a population of LSB galaxies that could resolve the discrepancy in the number counts to $m_B \approx 23$, but a still-unexplained excess of FBGs at fainter magnitudes remained.

The number and luminosity densities derived from the luminosity function for the LSB sample do not support the hypothesis of McGaugh (1994). They show that existing luminosity functions are missing a substantial fraction of the local galaxy population, but that the missed fraction is too small to account for the discrepancy between no-evolution models and the counts of FBGs. The present work finds a normalization and resultant number density for the LSB galaxies much lower than that assumed by McLeod (1994), and even his assumed higher numbers could not account for the discrepancy at faint magnitudes. The number density of LSBs relative to HSB galaxies increases with decreasing luminosity, but even at $M = -14$ it is only about one-half that found by extrapolating the function of Loveday et al. (1992). Even at the low luminosity end of the distribution, the APM survey does not find enough LSB galaxies to resolve the discrepancy.

Marzke et al. (1994a) considered the luminosity functions for different morphological types in the the CfA Redshift Survey data and found a very steep faint-end slope of $\alpha = -1.87$ for the irregular types Sm-Im. Assuming no evolution, they determined that this steep slope in the dwarf galaxy luminosity function could double the expected counts at $m_B = 25$, thus substantially reducing but not entirely eliminating the discrepancy between the no-evolution model and the observed counts. They also found that their luminosity functions for earlier galaxy

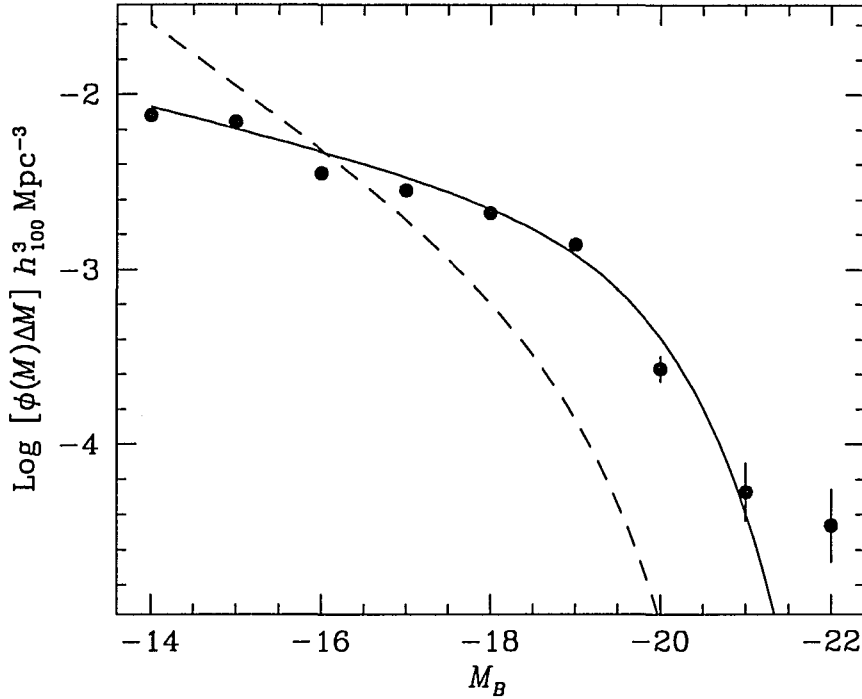


Figure 3.13: Comparison of luminosity functions for irregular galaxies. The points are the SWML luminosity function for the LSB irregular galaxies, and the solid curve is the LM fit of a Schechter function to those points. The dashed curve is the Schechter function derived by Marzke et al. (1994a) for irregular galaxies in the CfA Redshift Survey.

types did not match the local luminosity functions predicted for red ($B-V \geq 0.85$) and intermediate-color ($0.6 \leq B-V \leq 0.85$) galaxies predicted by Koo et al. (1993). As noted above, the overall result of Marzke et al. (1994a) for the Sm-Im types parallels the steeper slope found here among LSB galaxies in the same type range, although the slope estimated here is not so extreme ($\alpha = -1.31$). Figure 3.13 presents the luminosity functions for irregular galaxies from the LSB sample and from Marzke et al. (1994a) on the same scale, using the data from Table 3.4. The LSB irregulars have higher number densities than do the irregulars of Marzke et al. (1994a) at all luminosities $M < -16$, but the LSB irregulars are only one-third as

common at $M = -14$. Thus for the dwarf galaxies, the LSB irregulars cannot do as much to resolve the discrepancy as the luminosity function found by Marzke et al. (1994a), because the LSB irregulars do not have as steep a faint-end slope.

3.5.2 Bright Galaxies

Steidel & Dickinson (1994) developed a luminosity function for galaxies selected by their association with absorption features in the spectra of background QSOs. This selection process allowed them to identify galaxies with luminosities $M \sim M_*$ out to $z \gtrsim 1$ in a manner independent of the normal magnitude and surface brightness limits faced by local galaxy surveys. Their luminosity function for the rest-frame B band showed a steeply declining faint-end slope, while their function in the rest-frame K band showed a relatively flat slope. They obtained a normalization of $\phi_* = 3.0 \pm 0.7 \times 10^{-2} h_{100}^3 \text{ Mpc}^{-3} \text{ mag}^{-1}$. They compared this result to the normalization of $\phi_* = 1.4 \pm 0.17 \times 10^{-2} h_{100}^3 \text{ Mpc}^{-3} \text{ mag}^{-1}$ found by Loveday et al. (1992) and concluded that there was a discrepancy of a factor of 2 between the local density and the density in the redshift range to which they were sensitive ($0.3 \lesssim z \lesssim 1.5$).

If their conclusion of a discrepancy is correct, then LSB galaxies could account for at least part of the difference. The selection of galaxies by their identification with absorption features in QSO spectra should be blind to the surface brightness of the absorbers, so the normalization of Steidel & Dickinson (1994) should include galaxies similar to those identified by the APM survey. The overall density of LSB galaxies is not enough to explain the excess found by Steidel & Dickinson (1994), but the density of high luminosity galaxies may be more important for this purpose. The galaxies detected by Steidel & Dickinson (1994) are predominantly

high luminosity ($M_B \lesssim -19$). As noted above, the number and luminosity density of the LSB galaxies exceeds the levels from the Loveday et al. (1992) function in the range $-19 \geq M \geq -22$, so the inclusion of LSB galaxies like those found in the APM survey may well resolve the difference. Unfortunately, it is not clear that such a discrepancy really exists. As Table 3.2 makes clear, there is no general agreement on the local value of ϕ_* . Recent estimates from EEP, Loveday et al. (1992), Marzke et al. (1994b), and Marzke et al. (1994a) span a factor of two. Also, the normalization ϕ_* is very sensitive to the shape of the luminosity function; total number and luminosity densities integrated over the luminosity range of interest would be more robust measures of the galaxy population. Steidel & Dickinson (1994) do not give sufficient information about their derived luminosity functions to allow computation of integrated densities, so the question cannot be resolved more definitively without more information. It is intriguing, though, that they find an excess of high luminosity galaxies roughly similar to that represented by the LSB sample.

3.6 Conclusions

We have presented luminosity functions for the LSB galaxies of the APM LSB survey, and for a combined sample of LSB and HSB galaxies from the same region of the sky. We find that the inclusion of the LSB galaxies does not significantly change the shape of the combined luminosity function from that obtained by other, purely HSB, field surveys, except for an excess of low-luminosity galaxies and a small shift of M_* towards brighter values. We also find that LSB galaxies represent only about one-fourth to one-third the integrated number density of galaxies found by other field

galaxy studies. The luminosity function for LSB irregulars has a much steeper faint-end slope than the overall luminosity function, and this difference seems to account for the excess of low-luminosity galaxies in the overall function. LSB galaxies may therefore contribute to a resolution of the discrepancy between no-evolution models and the excess counts of faint blue galaxies, but they are not numerous enough to explain away the discrepancy entirely. Finally, we find that the density of high luminosity galaxies in the LSB sample is equal to or greater than the density of such galaxies seen in other field surveys. This relatively high density of luminous LSB galaxies could resolve the recently-noted difference between the numbers of local luminous galaxies and luminous galaxies detected at moderate redshift by their association with absorption features in QSO spectra.

Chapter 4

THE MASS-TO-LIGHT RATIOS OF FIELD LOW SURFACE BRIGHTNESS SPIRAL GALAXIES: CLUES FROM THE TULLY-FISHER RELATION

We have obtained 21 cm profiles and CCD surface photometry for a subset of field low surface brightness (LSB) spiral galaxies found by a large survey using the Automated Plate Measuring machine. We find that the LSB spirals generally follow the same Tully-Fisher relations defined by a sample of higher surface brightness (HSB) galaxies drawn from the Ursa Major cluster, albeit with a considerably greater scatter. This general trend implies that LSB galaxies of a given total luminosity have mass-to-light ratios (M/L) similar to those of HSB galaxies of comparable total luminosity, despite their differences in luminosity density (*i.e.*, surface brightness). We also find evidence that galaxies with extremely large half-light radii (the “Malin 1 cousins”) tend to be excessively luminous for their rotation speeds. We find that, at a given profile width, the luminosity of an LSB galaxy relative to the Tully-Fisher

relation seems to be weakly anticorrelated with gas richness, indicating that some of the higher scatter may be associated with the evolutionary status of the LSB galaxies. Finally, we find that the LSB galaxies tend to have higher total atomic gas masses than the Ursa Major comparison galaxies, despite the generally comparable optical luminosities between the two sets.

4.1 Introduction

In Chapter 3, we estimated the space density and luminosity density of galaxies that had been overlooked by previous surveys because of their low contrast against the night sky. The next step in determining the pernicious effects of sky brightness is to compare the properties of LSB galaxies to those of HSB galaxies. One particularly interesting galaxian property is the mass-to-light ratio (M/L). For example, it is important to know whether LSB galaxies represent a cosmologically significant amount of baryonic matter that has been overlooked by previous galaxy surveys. Since determination of the masses of large numbers of individual galaxies is difficult, it makes more sense to proceed by determining a luminosity function for LSB galaxies, and then in some way estimating their M/L to arrive at a mass distribution function. Also, comparisons of the M/L of LSB and HSB galaxies could help shed light on the reasons for their apparent differences in stellar populations and evolution as noted by McGaugh & Bothun (1994). Although Impey et al. (1988) and Bothun et al. (1991) were unable to quantify the M/L s for the LSB dwarf galaxies of the Virgo or Fornax clusters, they concluded that these small ($-11 \lesssim M_B \lesssim -15.5$) galaxies must have very high M/L s in order to survive the tidal fields of those massive clusters. If low surface brightness is correlated with high M/L , then the

more luminous LSB spirals in the general field could have very high total masses. In order to address this question, we have studied such a set of field LSB spiral galaxies ($-17.5 \lesssim M_B \lesssim -21.5$) to see how their M/L s compare to those of HSB galaxies having similar total luminosities.

Actually determining a M/L for any individual spiral galaxy requires a well-measured rotation curve and a halo model with several assumed parameters, as exemplified by the work of Kent (1986) and Kent (1987). However, it is possible to compare M/L s at a particular radius for two different sets of spiral galaxies by comparing their locations in the luminosity—H I profile width plane. HSB spiral galaxies fall along a well-defined track in this plane: the famous Tully-Fisher relation, from Tully & Fisher (1977). The virial theorem for a galaxy bound by Newtonian gravity gives $M/r \propto v^2$, where r is the galactocentric radius, v is the rotation speed at that radius, and M is the mass enclosed within that radius. Taking $\langle\mu\rangle$ as the mean surface brightness, we have the luminosity as $L \propto \langle\mu\rangle r^2$. Assuming $\langle\mu\rangle$ and M/L are constant, the relation $L \propto v^4$ can be readily obtained. Thus, under these idealized assumptions, the Tully-Fisher relation should have a slope of 10. Variations in M/L among individual galaxies in the set will produce scatter around this slope. Any dependence of M/L on L , or of $\langle\mu\rangle$ on L , will change the slope. If two samples of galaxies have systematically different M/L s, this difference will manifest itself as an offset in their Tully-Fisher zeropoints. Bothun & Mould (1987) showed that surface brightness variations within a fixed profile width can contribute greatly to the scatter around the Tully-Fisher relation. They were attempting to improve the Tully-Fisher relation as a distance indicator, and they found that the scatter in the relation could be reduced significantly by excluding the galaxies with the highest and lowest overall surface brightnesses. We take the opposite approach here; we intend to use the deviations from a baseline Tully-Fisher relation to learn

something about other properties of the LSB galaxies.

To that end, we present photometric and 21 cm radio observations of a sample of LSB galaxies. In Section 4.2 we describe the galaxies chosen for this comparison and the data reduction and analysis techniques employed. Section 4.3 contains the comparison of LSB and HSB Tully-Fisher relations, and in Section 4.4 we review the implications of those comparisons for both the LSB galaxies and the Tully-Fisher relation itself. Section 4.5 lists our conclusions.

4.2 Data Reduction And Analysis

4.2.1 Galaxy Selection and Data Reduction

We have chosen galaxies for this study from the survey of Impey et al. (1995), and Chapter 2 gives a complete description of the survey parameters. The sample of galaxies is complete to specific angular size and surface brightness criteria: machine scanning verifies that all objects with a projected central surface brightness of $\mu_B(0) \geq 22 \text{ mag arcsec}^{-2}$ and with an angular size in the range $13'' \leq \theta \leq 200''$ (where θ is the diameter at an effective surface brightness of $24.5 \text{ mag arcsec}^{-2}$) will be found. CCD images were also obtained in B , V , and R of 112 LSB galaxies found by that survey, and 190 of the galaxies were detected in the 21 cm H I line with the 305 m Arecibo telescope. We have chosen from that database all the spiral galaxies that have H I profile widths $W_{50} > 180 \text{ km s}^{-1}$ (where W_{50} is the width measured at 50% of the mean flux) and that have CCD images. We also independently obtained CCD images in I of 11 of LSB galaxies which met all of the above criteria, 7 of which also had BVR photometry. Finally, after measuring the

ellipticities as described below, we further eliminated those galaxies with ellipticities $e < 0.3$ (*i.e.*, inclinations $i \lesssim 45^\circ$). Small inclination angles require large $1/\sin i$ corrections to obtain the edge-on profile width from the observed profile width, and the large corrections raise the uncertainties in the profile widths to unacceptable levels. The final sample of LSB galaxies includes 21 galaxies measured in B , 17 galaxies measured in R , and 10 galaxies measured in I .

The CCD images were bias-subtracted and flat-fielded using standard IRAF tasks. Total integrated magnitudes were then determined for all galaxies using modified VISTA routines. First, sky values and uncertainties were measured using the corners of the image or four other large regions well away from the galaxy. Second, the sky was subtracted from the image as a constant or as a flat plane if there was a smooth gradient in the sky across the image. Third, elliptical isophotes were fit to the galaxy image. Fourth, a two-dimensional radial profile of average isophotal surface brightness vs. isophotal semi-major axis was plotted, and an exponential model was fit to regions of the radial profile that appeared to be well beyond any bulge or central condensation. Also, at this point both the radial surface brightness profile and the radial total intensity growth curve were examined for evidence of errors in the sky level; if any were suspected, the entire process was repeated with an adjusted sky level. Fifth, the total galactic intensity (*i.e.*, including both bulge and disk) was determined by summing the actual pixel intensities inside the outermost isophote, and then extrapolating the exponential fit only from this last isophote to infinity. This extrapolation typically increased the galactic magnitude by < 0.1 mag. Finally, this total intensity was transformed to a total magnitude in the usual manner using zero points and color terms derived from observations of standard stars from Landolt (1992), Christian et al. (1985), and Odewahn et al. (1992). We corrected for Galactic reddening using the maps of Burstein & Heiles (1982), and

applied k -corrections from the tabulations of Coleman et al. (1980). For those galaxies observed in more than one filter, the isophotes were fit only to one filter, and the same isophotes were used as elliptical apertures for summing intensities in the other filters. This procedure ensures that both the radial color profiles and the total colors of the galaxies are uniformly measured.

A brief comment about the colors is necessary here. For those galaxies with both B and R magnitudes, the $B-R$ colors are fairly reliable, in that B , V and R images were obtained on the same nights and processed and calibrated in parallel. The I images, and the B images of the 4 galaxies that do not also have R data, were all obtained some months later using different CCDs, different filters, different standard stars, and different observing techniques. Hence the $B-I$ and $R-I$ colors are probably not as trustworthy. Galaxy 0233+0012 illustrates the problem. Its colors are $B-R = 1.13$ and $R-I = -0.41$. Much of this inconsistency in color is probably due to a difference in observing techniques. The B , V and R images were taken as single long exposures centered on the galactic nucleus with a TI 800×800 pixel CCD that could be flatfielded well with dark sky flats. The I band image was taken with a Loral 800×1200 pixel CCD which has the same pixel scale as the TI but also has severe fringing at long wavelengths. The I image was compiled from a series of short exposures, each taken with the galaxy in a different part of the field of view. This procedure allowed better flatfielding, but resulted in a small composite image that has few if any sky pixels that are not contaminated at some level by the faint outer regions of the galactic disk. Thus, the I luminosity for this object is probably underestimated due to the likely overestimation of the sky flux level.

For each galaxy, a disk ellipticity was estimated by a simple average of the ellipticities of all the isophotes used in fitting the exponential disk profile. The

inclination was determined by assuming that the ellipticity was due to the inclination of a circular disk, and that an edge-on disk would have an intrinsic ellipticity of 0.8, per Holmberg (1958). Finally, a half-light radius was measured for each galaxy by locating the semi-major axis at which the integrated magnitude was 0.753 mag fainter than the extrapolated total magnitude. We have chosen to report this half-light radius, rather than the fitted disk exponential scale length, because it is model-independent, and because it reflects to some extent the degree of central condensation in the luminosity profile, as well as the scale of the disk.

H I parameters of these galaxies were determined from 21 cm observations using the Arecibo radio telescope. The data were reduced on-site using the Arecibo Observatory's standard GALPAC software. Widths of the reduced H I profiles were measured in several different ways; those shown here are W_{50} , the full width at 50% of the mean flux across the profile, and W_{20} , the full width at 20% of the peak flux. Heliocentric radial velocities were determined from the centers of the profiles and adjusted for Galactic rotation using the conventional $300 \sin l \cos b \text{ km s}^{-1}$ correction. The reduced data values for the selected LSB galaxies appear in Table 4.1.

4.2.2 Selection of HSB Comparison Sets

The desiderata for a comparison set of HSB galaxies are fairly simple. First, the chosen set must have H I and photometric data comparable to those of our LSB set. In particular, the galactic magnitudes should be determined by surface photometry rather than aperture photometry, to ensure that the galaxy magnitudes are measured in a way that does not introduce a bias towards underestimating luminosity as galaxy scale length increases, as detailed in Bothun & Mould (1987). Second, the comparison galaxies should cover ranges of luminosity and H I profile width

Table 4.1: Low Surface Brightness Galaxies Used For Tully-Fisher Analysis

Name (1)	RA (2)	Dec (3)	v (4)	w_{50} (5)	w_{20} (6)	e (7)	$r_{1/2}$ (8)	B_T (9)	R_T (10)	I_T (11)
0014+0115	0:14:03.1	+1:15:23	12377	233	250	0.34	6.1	15.91	14.98	...
0023+0044	0:23:51.1	+0:44:35	5502	318	333	0.39	5.2	16.02	15.05	14.56
0050+0230	0:50:54.4	+2:30:11	5126	226	230	0.39	2.8	15.62	14.66	...
0059+0248	0:59:11.4	+2:48:47	4499	178	187	0.54	4.0	15.77	15.21	14.84
0142-0033	1:42:29.8	-0:33:06	5480	165	179	0.32	3.5	16.89	16.00	...
0229+0004	2:29:09.4	+0:04:22	6369	212	224	0.46	5.4	15.60	14.72	14.39
0233+0012	2:33:26.9	+0:12:10	2648	194	201	0.40	4.7	14.19	13.06	13.47
0243+0301	2:43:13.1	+3:01:13	6846	339	345	0.61	4.5	15.17	14.42	...
0400+0149	4:00:12.6	+1:49:36	3781	493	499	0.75	7.2	14.09	...	11.40
0411+0236	4:11:46.8	+2:36:21	3293	270	270	0.50	4.3	14.62	...	12.91
0918-0028	9:18:03.9	-0:28:01	3290	277	329	0.35	1.8	15.60	14.49	...
1106+0032	11:06:06.2	+0:32:16	7466	334	338	0.43	4.3	16.12	15.03	...
1132+0249	11:32:30.9	+2:49:40	5088	182	196	0.70	4.6	15.58	14.88	...
1209+0137	12:09:25.9	+1:37:40	6136	275	292	0.43	3.2	16.02	15.11	...
1226+0105	12:26:39.2	+1:05:39	23529	269	278	0.32	15.7	16.10	15.01	...
1300+0144	13:00:42.6	+1:44:12	12164	393	393	0.74	9.9	17.42	15.94	...
2303-0006	23:03:57.8	-0:06:02	7644	295	303	0.41	6.3	14.41	13.57	13.14
2315-0000	23:15:41.9	-0:00:43	9109	420	428	0.40	9.2	15.19	...	13.16
2318+0236	23:18:34.0	+2:36:35	4112	217	229	0.36	2.9	15.64	...	14.20
2344+0139	23:44:47.4	+1:39:20	5397	197	205	0.37	4.2	15.14	13.90	...
2349+0248	23:49:17.0	+2:48:14	5489	280	290	0.37	6.3	14.39	13.68	13.15

Notes:

Columns (2) and (3): equatorial coordinates for the 1950.0 equinox.

Column (4): radial velocity in km s^{-1} , corrected for Galactic rotation.

Column (5): full width of 21 cm profile in km s^{-1} , measured at 50% of the mean flux.

Column (6): full width of 21 cm profile in km s^{-1} , measured at 20% of the peak flux.

Column (7): ellipticity = $(1 - b/a)$.

Column (8): half-light radius in kiloparsecs.

Columns (9) - (11): total apparent magnitudes.

comparable to those covered by the LSB galaxies, to ensure that any effects seen are caused by the surface brightness difference and not by differences in total luminosity or mass. Finally, it would be helpful to have some color information available for the comparison set, to see if any observed differences in the Tully-Fisher relation can be related to possible differences in stellar populations.

The Ursa Major cluster of galaxies satisfies this bill of particulars nicely. The magnitudes reported by Pierce & Tully (1988) are derived from surface photometry, and comparable color information is available. Both samples cover a similar range of Tully-Fisher parameters, and the Ursa Major cluster has no special problems of internal structure or projection effects. Pierce & Tully (1988) used isophotal magnitudes within the outermost fitted isophote without adding an extrapolation of the disk model as we did for our LSB set. This extrapolation increased the uncertainties in our total magnitudes slightly as compared with the isophotal magnitudes. However, for two galaxies of equal total luminosity, the one with the lower central surface brightness will have a larger fraction of its total light outside of any given isophotal level. Use of the extrapolated totals avoided this source of possible bias and justified the larger random uncertainties. We have included the uncertainties associated with the extrapolation in our estimates of the total photometric uncertainties (see 4.3.3).

The Coma cluster sample of Bernstein et al. (1994), was also used; indeed, the comparison with this Coma sample was what first inspired this study. However, the Coma sample fails to meet two of the criteria: Bernstein et al. (1994) obtained only *I* magnitudes, and their sample covers different ranges in both H I profile width and luminosity. *B* magnitudes for most of the Coma sample were reported by Fukugita et al. (1991), but those magnitudes were measured from photographic plates, so the

color information is not as precise as for the other samples. To ensure consistency with the LSB sample, we also removed from the Ursa Major sample of Pierce & Tully (1988) 3 galaxies with $i < 45^\circ$, leaving 23 galaxies in that sample. Bernstein et al. (1994) used the same minimum ellipticity of 0.3 for their sample of Coma galaxies, so we eliminated none from the Coma set, which includes 17 galaxies in B and 18 galaxies in I . The profile widths and magnitudes of the comparison sets were used as reported by Pierce & Tully (1988) for Ursa Major and Bernstein et al. (1994) for Coma. Because these two groups used different adjustments to account for the effects of inclination on profile width and magnitude, it was necessary to adjust the data for the LSB galaxies separately for each comparison.

In adjusting the LSB data for comparison to the Ursa Major set, we followed the system used by Pierce & Tully (1988) who had in turn adopted adjustments proposed by Tully & Fouqué (1985). First, we obtained the “rotational profile width” W_r from the measurement of $W_{20} = W_{20}^{raw}/(1+z)$ as

$$W_r^2 = W_{20}^2 + W_t^2 - 2W_{20}W_t[1 - e^{-\alpha}] - 2W_t^2e^{-\alpha}, \quad (4.1)$$

where W_t is the velocity component due to random thermal motions, $\alpha = (W_{20}/W_c)^2$, and W_c is a scaling parameter chosen to provide a smooth transition between a linear summation of the rotation and dispersion terms (for giant galaxies) and quadrature summation (for dwarf galaxies). For consistency with Tully & Fouqué (1985) and Pierce & Tully (1988), we adopted $W_t = 38 \text{ km s}^{-1}$ and $W_c = 120 \text{ km s}^{-1}$. Given the profile width constraint applied in the selection of LSB galaxies for this study, this formula closely approximates a linear subtraction of 38 km s^{-1} . This rotational width W_r is set to its edge-on value as $W_{rc} = W_r / [\sin i]$. We note that equation 4.1 may not be applicable to LSB galaxies; in systems with lower surface mass density, the restoring force is reduced and deviations from circular

motion are likely to be more prominent than assumed in equation 4.1. We emphasize that we are applying equation 4.1 here solely for consistency of treatment with Pierce & Tully (1988). Second, galaxy total magnitudes in B were corrected to face-on values by subtracting the net internal extinction due to inclination $A_B^{i-0} = A_B^i - A_B^0$. A_B^i is found by

$$A_B^i = -2.5 \log \left[f(1 + e^{-\tau \sec i}) + (1 - 2f) \left(\frac{1 - e^{-\tau \sec i}}{\tau \sec i} \right) \right], \quad (4.2)$$

where $\tau = 0.55$ is the assumed optical depth and $f = 0.25$ is the unobscured fraction of the disk facing the observer, and $A_B^0 = 0.27$ from the preceding equation with $i = 0$. For consistency with Pierce & Tully (1988), we assumed that extinctions in R and I were 61% and 44% of that in B . Finally, to make the inclination-corrected apparent magnitudes directly comparable to those for the Ursa Major set, we adjusted the LSB galaxy magnitudes by $5 \log(v/1324)$, where v is the LSB galaxy's radial velocity from Table 4.1 and 1324 km s^{-1} is the systemic velocity of the Ursa Major cluster given by Pierce & Tully (1988).

In adjusting the LSB data for comparison to the Coma set, we followed the procedures outlined by Bernstein et al. (1994). The inclination-corrected (*i.e.*, edge-on) profile width was determined simply as $W_c = W_{50}^{raw} / [(1 + z) \sin i]$. Internal extinction corrections to the I apparent magnitudes followed the empirical scaling derived from the Coma comparison set of $\Delta I = 1.4 \times e$, where e is the ellipticity. We derived an internal extinction correction in B of $\Delta B = 1.9 \times e$ by applying the same empirical method of Bernstein et al. (1994) to the Coma galaxies' B magnitudes reported by Fukugita et al. (1991). That method involves fitting a Tully-Fisher relation to the uncorrected magnitudes, plotting the residuals from that relation as a function of ellipticity, then fitting a straight line to that plot and using the slope of the line as the correction factor. Again, we applied these extinction corrections

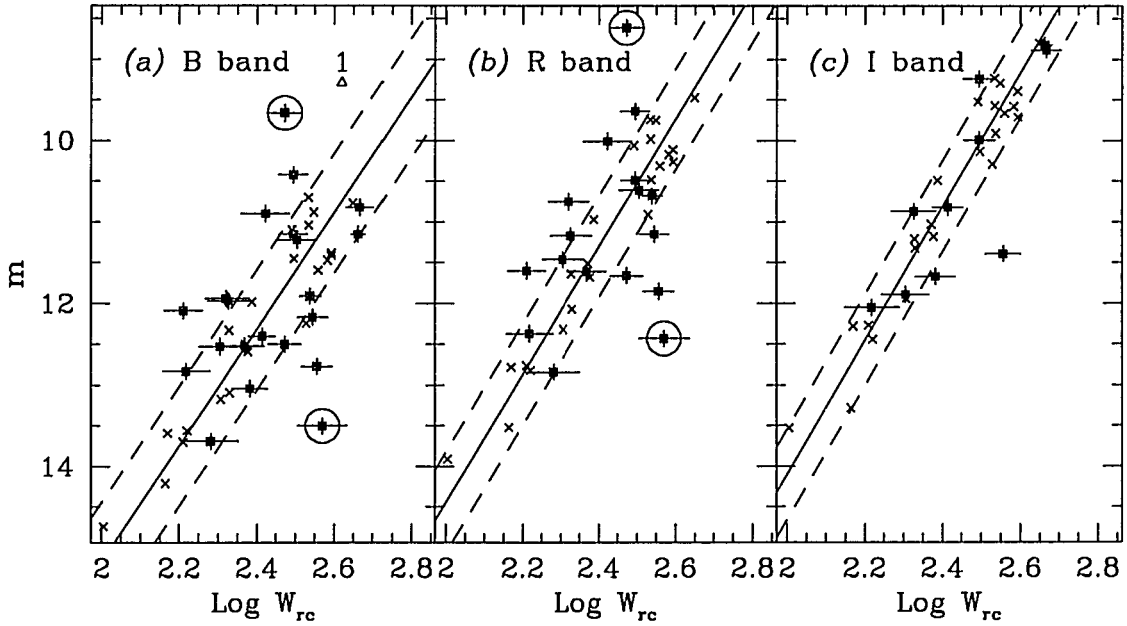


Figure 4.1: Tully-Fisher relations in B , R , and I . Dark squares represent the LSB spirals, and crosses represent the Ursa Major comparison galaxies. The solid lines are double-regression fits to the Ursa Major galaxies, and the dashed lines show the 2σ range around those fits. The labelled triangle shows the position of Malin 1. The open circles mark the LSB galaxies excluded from the “restricted” sample because of their radii.

determined from the Coma galaxies to the LSB sample solely to ensure consistency of treatment with Bernstein et al. (1994). Finally, the inclination-corrected apparent magnitudes of the LSB galaxies were adjusted by $5 \log(v/7000)$ to achieve the same zero point as the Coma galaxies.

4.3 Comparison Of Tully-Fisher Relations

4.3.1 Luminosity—Profile Width Correlations

Figure 4.1 shows the comparison of the Ursa Major and LSB Tully-Fisher

Table 4.2: Tully–Fisher Correlation Coefficients

Sample	<i>B</i>		<i>R</i>		<i>I</i>	
	<i>r</i>	<i>s</i>	<i>r</i>	<i>s</i>	<i>r</i>	<i>s</i>
LSB(complete)	−0.38	−0.35	−0.33	−0.19	−0.83	−0.84
LSB(restricted)	−0.55	−0.35	−0.51	−0.40
Ursa Major	−0.94	−0.87	−0.97	−0.89	−0.97	−0.90
Coma	−0.90	−0.90	−0.99	−0.99

Note: r is the Pearson linear correlation coefficient, and s is the nonparametric Spearman rank correlation coefficient.

relations in B , R , and I , and Figure 4.2 shows the comparison of the Coma and LSB Tully-Fisher relations. The LSB galaxies are clearly less tightly correlated than either the Ursa Major or Coma galaxies. Coefficients of the correlation between luminosity and profile width for the various samples are given in Table 4.2; coefficients are shown for both parametric linear correlation and non-parametric Spearman rank correlation. The coefficients for the LSB galaxies are reported both for the full sample and (in B and R) after excluding the galaxies with the largest and smallest half-light radii (the “restricted sample”). In the I band, the null hypothesis that the correlations of the LSB and Ursa Major galaxies are the same can be rejected at the 96% confidence level; in the other wavebands, this null hypothesis can be rejected at confidence levels $> 99\%$. For the LSB galaxies, the luminosity-profile width correlation is stronger in I than in B or R , but the differences are not highly significant, in the sense that the null hypothesis that the correlations are the same can be rejected at only about the 80% confidence level for the complete LSB sample, or about the 90% confidence level for the restricted LSB sample. The reduction of scatter in the Tully-Fisher relation with increasing wavelength has been noted before, beginning with Aaronson et al. (1979), and is

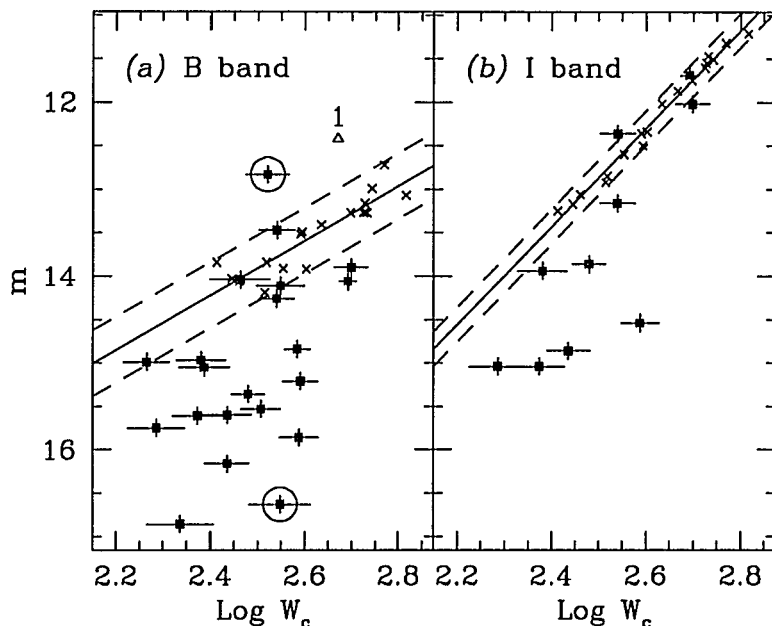


Figure 4.2: Tully-Fisher relations in B and I for the LSB spirals (dark squares) and the Coma comparison galaxies (crosses). The solid lines show the forward fit to the Coma galaxies, and the dashed lines show the 2σ range around that fit. Coma I data and fit are from Bernstein et al. 1994. Coma B magnitudes are those reported by Fukugita et al. 1991 for the same galaxies covered by Bernstein et al. 1994. The triangle shows the position of Malin 1. The open circles mark the LSB galaxies excluded from the “restricted” sample because of their radii.

usually taken as indicating that shorter wavelengths are more strongly affected by internal extinction and the luminosity of bright but relatively scarce young stars.

4.3.2 Slopes of the Luminosity—Profile Width Relations

Table 4.3 shows the fit parameters for the luminosity-profile width relations of the various samples. The entries designated “forward” are the results of standard least-squares fits which treat profile width as the independent variable and minimize the residuals in luminosity. The entries designated “double” are the results of double-

regression fitting which simultaneously minimizes residuals in both luminosity and profile width. Because the profile width has larger relative measurement uncertainties, these uncertainties dominate the weighting in these fits and cause the results to closely resemble those of a “reverse” fit (*i.e.*, one where luminosity is the independent variable and profile width is the dependent variable). Two fits are reported for the Ursa Major sample; these are the forward and double-regression fits obtained by us on the sample without the three galaxies with $i < 45^\circ$. The exclusion of these three galaxies changed the double-regression slope from the value reported by Pierce & Tully (1988) by an amount smaller than the error bars on either fit.

The forward and double-regression fit parameters for the LSB galaxies bracket the parameters for the Ursa Major comparison set, and the differences in all cases are larger than the formal errors. To test the significance of these differences, a reduced χ^2_ν was calculated as a measure of goodness-of-fit to the LSB galaxies for each of the lines fitted to the LSB galaxies and to the Ursa Major galaxies. F tests were applied with the null hypothesis that the reduced χ^2_ν 's are indistinguishable. In all cases and in all filters, the confidence with which the null hypothesis could be rejected was $< 50\%$, so there is no statistical significance to the difference in fit parameters, in the sense that Tully-Fisher lines fitted to the Ursa Major galaxies represent the “true” trend among the LSB galaxies about as well as lines fitted to the LSB galaxies directly. We also tested for a shift in the Tully-Fisher zeropoint between the LSB and Ursa Major samples by fitting a line to the LSB galaxies but forcing the slope to be the same as that derived from the fit to the Ursa Major sample. In all such cases, the differences between the Ursa Major and LSB zeropoints were smaller than their uncertainties.

The slopes derived for the Coma galaxies in I by Bernstein et al. (1994) and in B

Table 4.3: Tully-Fisher Fit Parameters

Sample/ Filter	Forward Fit			Double Regression Fit		
	a	b	σ	a	b	σ
LSB _r ^a						
B	-3.52 ± 0.17	20.56 ± 0.43	0.701	-10.74 ± 2.06	38.10 ± 5.02	1.178
R	-3.59 ± 0.22	19.83 ± 0.53	0.713	-13.18 ± 2.94	42.88 ± 7.07	1.326
I	-6.85 ± 0.22	27.35 ± 0.54	0.667	-9.84 ± 1.76	34.69 ± 4.31	0.792
UMaj ^b						
B	-6.36 ± 0.04	27.59 ± 0.09	0.385	-7.14 ± 0.50	29.46 ± 1.22	0.407
R	-7.35 ± 0.02	28.95 ± 0.06	0.327	-7.85 ± 0.42	30.15 ± 1.00	0.338
I	-7.75 ± 0.02	29.41 ± 0.06	0.321	-8.21 ± 0.41	30.51 ± 0.99	0.331
Coma ^c						
B	-3.14 ± 0.40	13.58 ± 0.04	0.185
I	-5.65 ± 0.20	12.29 ± 0.10	0.100

Note: The Forward fits are standard least-squares fits that minimize residuals in luminosity. The Double Regression fits simultaneously minimize residuals in both profile width and luminosity. In all cases, a denotes the slope of the fitted line, b denotes the intercept, and σ denotes the rms error of the fit.

^aFits to the restricted sample of LSB galaxies were of the form $mag = a \times \log w + b$.

^bParameters reported here differ slightly from those reported by Pierce and Tully (1988) because three galaxies included in their fit were excluded here for having inclinations $i < 45^\circ$. Fits were of the form $mag = a \times \log w + b$.

^cParameters for fits to the Coma sample in I are those reported by Bernstein et al. (1994). The fit in B was performed using magnitudes reported by Fukugita et al. (1991). In both filters, the fit was of the form $mag = a \times (\log w - 2.602) + b$.

by us from the magnitudes of Fukugita et al. (1991) are lower than any of the slopes derived from the Ursa Major sample and lower than the double-regression slopes derived from the LSB sample. There is no obvious reason why the Tully-Fisher relation for the Coma set should be so different from that of the other two. One possible explanation is the different redshifts of the Coma and Ursa Major samples. The Coma galaxies have considerably higher recessional velocities than those in the Ursa Major cluster, and claims have previously been made for a decrease in the the Tully-Fisher slope with increasing redshift, as summarized by Djorgovski et al. (1988). However, the LSB galaxies cover a very broad range of recessional velocities that overlaps the velocities of both the Ursa Major and Coma samples, and yet their slopes are statistically indistinguishable from those of the Ursa Major set. Another possibility may be cluster membership. As Bernstein et al. (1994) note, all the galaxies in their Coma sample are probably in free expansion and not bound to the Coma cluster; the Ursa Major galaxies selected by Pierce & Tully (1988) are almost certainly bound members of that cluster. The LSB galaxies are field galaxies that come from all around the celestial equator, but in the luminosity-profile width plane they resemble the Ursa Major cluster galaxies more than the field galaxies of the Coma sample, so it is difficult to ascribe the slope difference to cluster membership. A third property that distinguishes the Coma sample is the range of profile widths represented there. The Coma sample extends to higher profile widths than do either the Ursa Major or LSB samples, and it does not have any galaxies with profile widths as low as the lowest-width members of the other two. Some authors, including Aaronson & Mould (1983), Aaronson et al. (1986), and Mould et al. (1989) have presented evidence of nonlinearity in the Tully-Fisher relation. However, the slope difference between the Ursa Major and Coma samples is more severe than any previously claimed curvature of the Tully-Fisher relation at

high profile widths. Also, in the region of profile width where the Coma and LSB samples overlap, most of the LSB galaxies lie well below the trend of the Coma sample, thus suggesting that the difference is a shift of both the slope and zeropoint of the line and not simply a curvature at higher profile widths. Further investigation is needed to determine why the Tully-Fisher slopes of these samples are so different.

4.3.3 Scatter in the LSB Luminosity — Profile Width Relation

Examination of the error budget demonstrates that the LSB galaxies exhibit a large intrinsic scatter around the Tully-Fisher trend. First, we have conservatively assumed a 0.1 magnitude error in the LSB total magnitudes, based on the comparison of B band frames taken of the same galaxies on different nights and with different CCDs. The internal uncertainties for any single measurement, which include the effects of the extrapolation to total magnitudes, are considerably smaller than this, but the external deviations among measurements of the same galaxy on different nights are typically $0.08 \sim 0.1$ mag, due in part to the large effect of a slight error in estimating the sky brightness. When all or most of a galaxy's area has flux levels less than 10% that of the sky, a very small error in determining the sky flux results in a large error in the galaxy's total magnitude. Our procedure for estimating the sky levels in four different parts of the image allows us to estimate the possible sky level errors that could result from residual flatfielding errors. These remaining flatfielding errors are typically $\sim 0.3\%$, and never larger than 1.0%. The change in magnitude that would result from a sky error of a few tenths of a percent varies with the size of the galaxy on the frame, but it typically is $0.05 \sim 0.07$ mag. Combining this potential sky error in quadrature with the internal uncertainties yields a total

error of $0.08 \sim 0.1$ mag, which is consistent with the external deviations for those galaxies with multiple observations.

Second, we have assumed a conservative error of 15 km s^{-1} in the profile width of LSB galaxies with high S/N H I profiles ($S/N > 20$), and we scaled this number up with decreasing S/N . We also assumed an uncertainty of 5° in the inclinations, or 0.06 in ellipticity. Again, this assumed uncertainty is larger than the internal errors in the ellipticity of any one galaxy, but it reflects the potentially large systematic effects of a small error in the sky estimate. The resulting uncertainties in edge-on $\log W_{rc}$ or $\log W_c$ values have both a mean and a median value of 0.047, which imply typical uncertainties in the luminosities of $B \simeq 0.32$ mag, $R \simeq 0.37$ mag, and $I \simeq 0.38$ mag using the slopes derived from the Ursa Major fits. Adding these values in quadrature to the assumed 0.1 mag photometric uncertainty yields total measurement uncertainties for the LSB galaxies of $B \simeq 0.34$ mag, $R \simeq 0.38$ mag, and $I \simeq 0.39$ mag.

As seen in Table 4.3, the rms deviations of the LSB galaxies from their forward-fit Tully-Fisher relations are $B \simeq 0.70$ mag, $R \simeq 0.71$ mag, and $I \simeq 0.67$ mag. Subtracting the total measurement uncertainties in quadrature yields estimates of the intrinsic scatter as $B \simeq 0.61$ mag, $R \simeq 0.60$ mag, and $I \simeq 0.54$ mag, which are quite large despite the very conservative estimates of the measurement uncertainties. In contrast, Bernstein et al. (1994) found that their data on the Coma sample were consistent with *no* intrinsic scatter in I , and Pierce & Tully (1988) found their Ursa Major data to be consistent with an intrinsic scatter of only 0.1 mag in R and I and 0.15 mag in B .

4.4 Discussion

To the extent that the Tully-Fisher relation reveals trends in the M/L ratios of spiral galaxies, our data on the LSB galaxies are consistent with the conclusion that LSB field spirals in general have similar M/L ratios to the spirals in the Ursa Major cluster, as we have found no significant difference between the relations for the two samples. There is apparently a significant difference between the Tully-Fisher relations of the LSB spirals and those of the field spirals in the vicinity of the Coma cluster, but there is also a difference between the Tully-Fisher parameters and hence the M/L ratios of the Coma and Ursa Major samples. As noted above, there is no clear reason why the Coma sample of Bernstein et al. (1994) should be so different from the other two. If the environment has anything to do with the rotation speed or luminosity of a spiral galaxy as suggested by Rubin et al. (1988) and Whitmore et al. (1988)), it would be natural to expect the LSB galaxies, which are drawn from the general field, to more closely resemble another set of field galaxies than a sample drawn from a bound cluster, but instead the converse seems to hold.

As noted above, the LSB galaxies exhibit a large intrinsic scatter (0.61 mag in B , 0.60 mag in R , and 0.54 mag in I) around the baseline Tully-Fisher relation established by the Ursa Major sample. We first considered whether this intrinsic scatter could be produced by peculiar velocities. The mean radial velocity of the LSB sample is 7625 km s^{-1} , with a range of $2648 \leq v_{\text{rad}} \leq 23528 \text{ km s}^{-1}$. The largest peculiar velocities reported to date are $\sim 600 \text{ km s}^{-1}$, *e.g.*, Lauer & Postman (1994). Peculiar velocities this large would imply a mean fractional uncertainty in the redshift distances of 0.072, which in turn translates into a magnitude uncertainty of about 0.15 mag. Subtracting this worst-case estimate in quadrature still leaves intrinsic scatters of 0.59 mag in B , 0.58 mag in R and 0.52 mag in I . The real

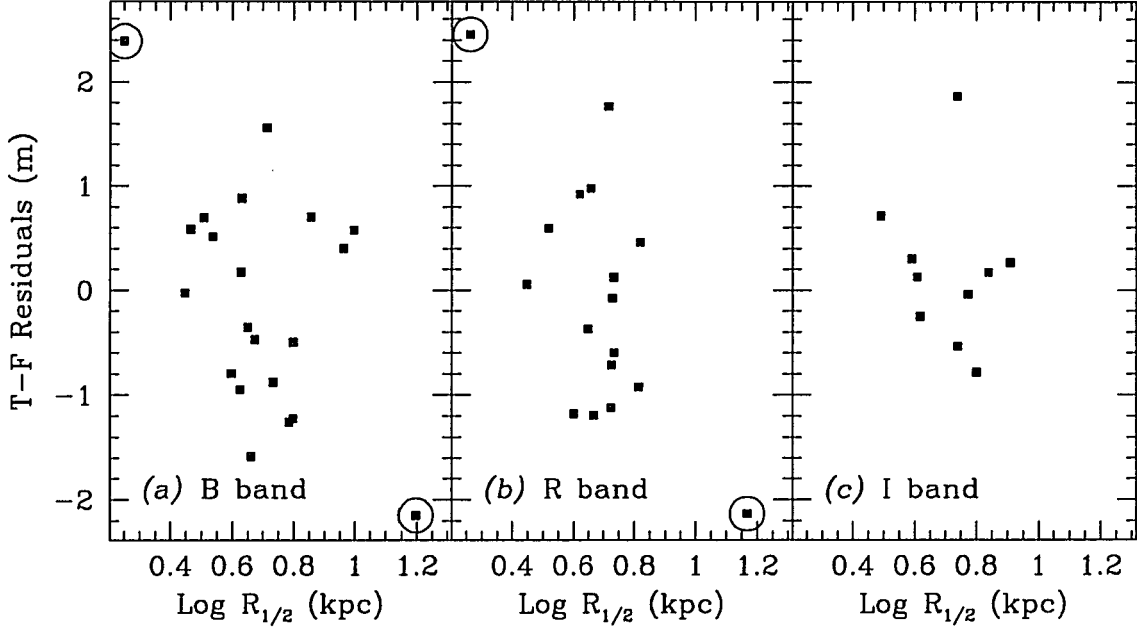


Figure 4.3: Residuals of the LSB spiral galaxies from our Tully-Fisher double-regression fits to the Ursa Major comparison sample, as a function of half-light radius. $R_{1/2}$ is in kpc, assuming $H_0 = 100 h_{100} \text{ km s}^{-1} \text{ Mpc}^{-1}$. The sense of the residuals is that a positive residual indicates a galaxy luminosity lower than predicted. The open circles mark the LSB galaxies excluded from the “restricted” sample because of their radii.

contribution of peculiar velocities is likely to be even less than this estimate. Thus most if not all of the intrinsic scatter must be due to real variations in the properties of the LSB galaxies themselves.

4.4.1 Intrinsic Scatter and Half-Light Radius

We next investigated the relationship between the Tully-Fisher residuals and the physical size of the LSB galaxies. Figure 4.3 shows this relation, with size represented by the half-light radii of the galaxies in kpc assuming $H_0 = 100 h_{100} \text{ km s}^{-1} \text{ Mpc}^{-1}$; the sense of the residuals is that galaxies that are

underluminous with respect to the Tully-Fisher trend line have positive residuals. We used our double regression fits to the Ursa Major sample to define the trend line for calculating the residuals. To quantify this relation, we have computed parametric and nonparametric correlation coefficients, quoted here as (Pearson Linear Correlation Coefficient; Spearman Rank Correlation Coefficient). Using the full sample of LSB galaxies in each filter, the coefficients are B : $(-0.49; -0.33)$, R : $(-0.64; -0.41)$, and I : $(-0.17; -0.35)$. These coefficients suggest a modest trend for small galaxies to be underluminous and large galaxies to be overluminous with reference to the Tully-Fisher trend line, but this suggestion must be treated very cautiously. It is apparent from Figure 4.3 that the “trend” is mostly due to two galaxies, the smallest (0918–0028) and the largest (1226+0105). These two galaxies are observable only in the spring, and thus were not observed in I . When these two galaxies are excluded from the B and R samples, the correlation coefficients drop precipitously to B : $(-0.04; -0.10)$ and R : $(-0.14; -0.14)$. Thus, the restricted sample (*i.e.*, the sample without these two galaxies) shows no statistical relation between physical size and deviation from the Tully-Fisher trend.

It is intriguing that the two galaxies that are the most extreme outliers in physical size are also the most extreme outliers from the Tully-Fisher trend line. The galaxy with the largest half-light radius is LSB 1226+0105, which was described in detail by Sprayberry et al. (1993). It is a member of the giant, gas-rich class of LSB spiral galaxies typified by Malin 1. For illustration, we have also plotted the position of Malin 1 on Figures 4.1 and 4.2, using data reported by Bothun et al. (1987) and Impey & Bothun (1989). We note that there is some uncertainty about the position of Malin 1. Bothun et al. (1987) were able to measure the surface brightness profile only to 1.5 scale lengths from the center, so a large extrapolation to total magnitude was required (about 0.9 mag). Also, Impey & Bothun (1989)

estimated an inclination $i \approx 45^\circ$ largely from circumstantial arguments and noted that the inclination was highly uncertain. At its nominal values of luminosity and inclination, Malin 1 is approximately 1.1 mag overluminous, but it has a half-light radius $R_{1/2} > 50$ kpc and would therefore be well off the scale of Figure 4.3. If the inclination of Malin 1 were as low as 30° , its position in Figure 4.1 would shift horizontally to $\log W_{rc} = 2.78$ and its overluminosity would decrease to 0.35 mag. Malin 2, as reported by Bothun et al. (1990), is also a member of this class, but it has an inclination $i < 45^\circ$ and so was not plotted here. Because so much of the luminosity of these giant disks lies in regions of very low surface brightness, use of an isophotal magnitude system suitable for higher surface brightness galaxies would reduce the measured luminosities for the LSB galaxies substantially.

The location of these two giant disks in the luminosity-profile width plane leads to an interesting conundrum. In one sense, it is reasonable that their large sizes and low densities should cause them to lie above the trend. Since the rotation velocity is related to enclosed mass and radius as $v^2 \propto GM(r)/r$, v should go down as r increases or M decreases. On the other hand, the slow rotation speeds and large radii should also imply a very long baryonic cooling time and hence very slow star formation in such disks, as predicted by Hoffman et al. (1992). These considerations would suggest that the luminosities of these disks should be low, implying that they should fall closer to or even below the general Tully-Fisher trend. The conundrum is that these disks have very high total stellar contents despite their anemic luminosity densities, large radii and long cooling timescales. Further investigation of the star formation processes and stellar populations of these disks are clearly needed to resolve this riddle.

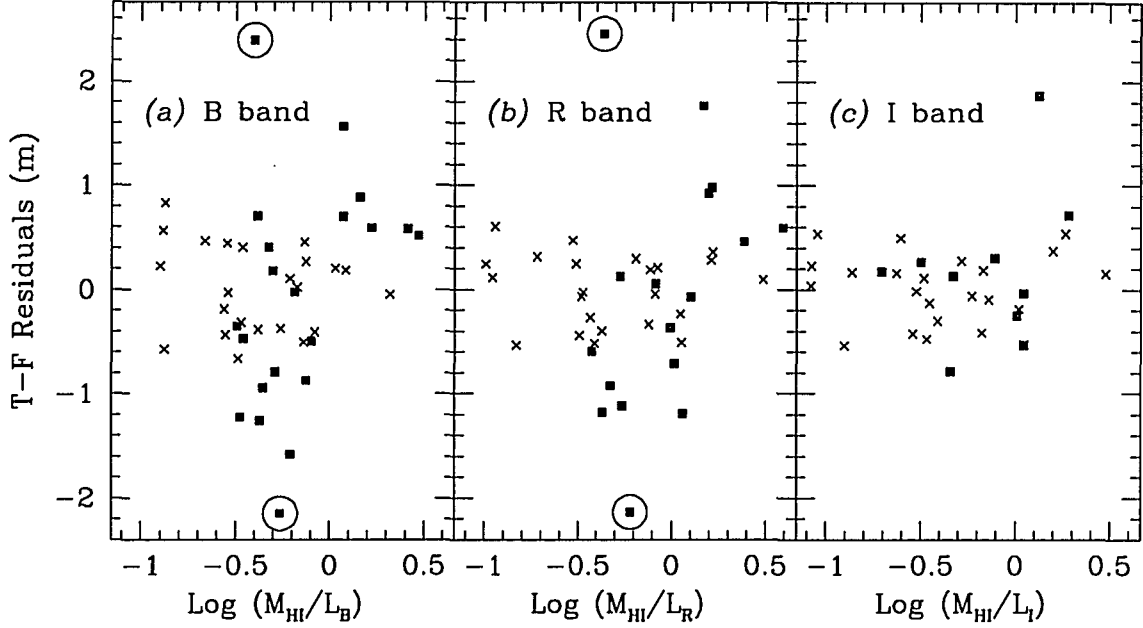


Figure 4.4: Residuals of the LSB spiral galaxies (dark squares) and the Ursa Major comparison galaxies (crosses) from the double-regression fits to the Ursa Major galaxies, as a function of gas richness. The sense of the residuals is that a positive residual indicates a galaxy luminosity lower than predicted. The open circles mark the LSB galaxies excluded from the “restricted” sample because of their radii.

4.4.2 Intrinsic Scatter and Galaxy Evolution

We also explored the relation between residuals from the Tully-Fisher trend and gas richness. Figure 4.4 shows the comparison of residuals versus the distance-independent ratio of H I mass to luminosity. The residuals were computed in the same manner as for Figure 4.3. There is some weak relationship between residuals and gas richness apparent in Figure 4.4. Again, we measured both parametric and nonparametric correlations, which are reported as (Pearson Linear Correlation Coefficient; Spearman Rank Correlation Coefficient). The strength of the correlations for the full samples of LSB galaxies are *B*: (0.37; 0.32), *R*: (0.35; 0.43), and *I*: (0.31; 0.30). In this comparison, excluding the two galaxies with outlier

radii (0918–0028 and 1226+0105) improves the correlation coefficients to B : (0.58; 0.51) and R : (0.64; 0.66). The improvements in both B and R are significant at about the 1σ level. As before, the sense of the residuals is that underluminous galaxies have positive residuals, so the positive correlation coefficients here imply that increasing gas richness is somewhat associated with more severe underluminosity. This association implies that the large intrinsic scatter of the LSB galaxies around the Tully-Fisher trend line may be related to their evolutionary state, in that the underluminous galaxies tend to be that way because they have not yet processed much of their gas into stars. It should be noted that luminosity enters into both sides of this correlation. If a galaxy’s luminosity is underestimated, both its Tully-Fisher residual and its gas richness will increase, thus artificially inflating the correlation coefficient. However, as noted in Subsection 4.3.3, the rms of the residuals is larger than the combined measurement errors and very much larger than the measurement errors in the luminosity alone. Even if all the residuals were reduced by a quadrature subtraction of the luminosity uncertainty, the correlation coefficient would not change significantly.

To explore further the issue of evolution, we also examined the relation between H I mass (M_{HI}) and profile width. Figure 4.5 shows this relation, with the corresponding relations for the Ursa Major and Coma samples also. Gas masses for the Ursa Major sample are from the survey of Fisher & Tully (1981), and those for the Coma sample are from the references cited by Bernstein et al. (1994). Estimates of M_{HI} assume $H_0 = 100 h_{100} \text{ km s}^{-1} \text{ Mpc}^{-1}$. Correlation coefficients for the four samples, using the notation (Linear correlation coefficient; Spearman rank correlation coefficient) are LSB(complete): (0.36; 0.45), LSB(restricted): (0.64; 0.67), Ursa Major: (0.60; 0.56), and Coma: (0.30; 0.34). The difference in the correlation between the complete LSB sample and the restricted LSB sample is significant at

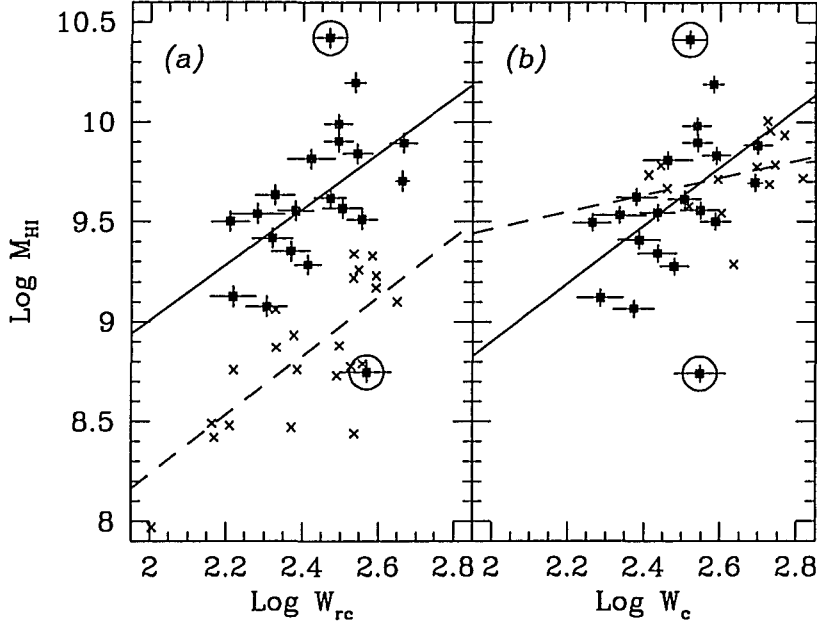


Figure 4.5: $\text{Log } M_{\text{HI}}$ as a function of profile width (the “21 cm Tully-Fisher relation”). M_{HI} is in units of solar mass, assuming $H_0 = 100 \, h_{100} \, \text{km s}^{-1} \text{Mpc}^{-1}$. In (a), the squares represent LSB galaxies, and the crosses represent the Ursa Major galaxies. In (b), the squares represent the LSB galaxies, and the crosses represent the Coma galaxies. The solid lines show the forward fits to the LSB galaxies, and the dashed lines show the forward fits to the comparison galaxies. The open circles mark the LSB galaxies excluded from the “restricted” sample because of their radii.

$\sim 1.5 \sigma$. Among the LSB galaxies, there are slight differences among the correlations of profile width against B , R , I , and M_{HI} , but the significance of the differences is $\lesssim 1 \sigma$ in all cases. Among the Ursa Major and Coma samples, however, the correlation between M_{HI} and profile width is weaker than the correlation between any measure of optical luminosity and profile width, and the differences are all significant at $\geq 3 \sigma$. Table 4.4 shows the parameters of forward fits to the M_{HI} —profile width relation for the restricted LSB, Ursa Major, and Coma samples. The fit for the restricted sample of LSB galaxies has an intercept that differs substantially from that of the Ursa Major sample, even though the slopes are comparable. The

Table 4.4: M_{HI} vs Log W Fit Parameters

Sample	a	b	σ
LSB (complete)	1.06 ± 0.07	7.02 ± 0.18	0.347
LSB (restricted)	1.38 ± 0.08	6.25 ± 0.18	0.217
Ursa Major	1.19 ± 0.05	6.39 ± 0.13	0.269
Coma	0.43 ± 0.09	8.61 ± 0.24	0.164

Note: All fits here are forward fits, *i.e.*, standard least-squares fits that minimize residuals in M_{HI} . a denotes the slope and b denotes the intercept, as $M_{HI} = a \times \log W + b$.

LSB galaxies are clearly offset towards higher H I masses, even though there was no apparent offset in luminosity in the optical Tully-Fisher relations (compare Figure 4.5(*a*) with Figure 4.1). The Ursa Major galaxies generally have large angular sizes, so it is possible that their H I masses are underestimated due to partial resolution by the telescope beam. However, Fisher & Tully (1981) estimated this correction for all the galaxies detected in their survey, and the average correction for these Ursa Major galaxies is 11%. The offset in H I mass between the LSB and Ursa Major samples is 0.75 dex, or about a factor of 5, so it is highly unlikely that beam size effects could be responsible for any significant part of the offset.

Thus, gas mass is as strongly related to rotation speed as is optical luminosity for the LSB galaxies, but the same does not hold for either the Ursa Major or Coma samples. This difference suggests that atomic gas may be a more significant component of total mass among LSB galaxies than for more visible spirals. Thus, LSB galaxies may be well described as unevolved, with considerable raw material still available for processing into stars. This finding is consistent with previous work by McGaugh & Bothun (1994) who found field LSB galaxies to be generally bluer

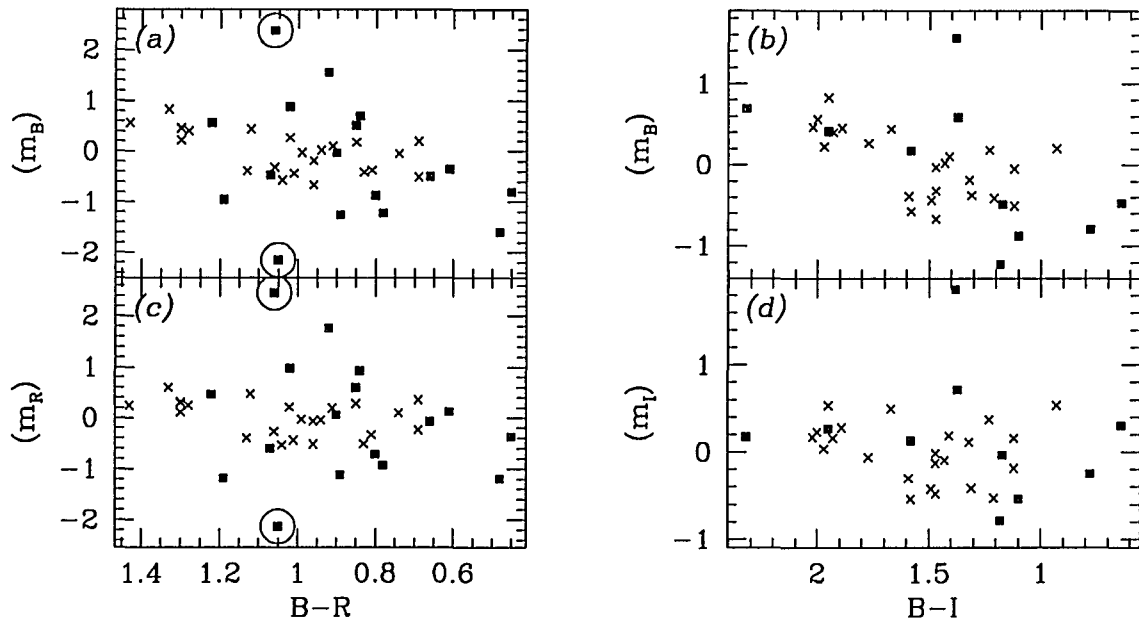


Figure 4.6: Residuals of the LSB spiral galaxies (dark squares) and the Ursa Major comparison galaxies (crosses) from the double-regression fits to the Ursa Major galaxies, as a function of galaxy total color. (a): B residuals vs. $B-R$; (b): B residuals vs. $B-I$; (c): R residuals vs. $B-R$; (d): I residuals vs. $B-I$. The sense of the residuals is that a positive residual indicates a galaxy luminosity lower than predicted. The open circles mark the LSB galaxies excluded from the “restricted” sample because of their radii.

than more visible galaxies and argued that the most likely cause was slow, continuous star formation. Furthermore, the mostly unsuccessful efforts by Schombert et al. (1990) (no detections out of 19 observations) and Knezek (1993) (3 detections out of 17 observations) to detect molecular gas in LSB galaxies suggest that star formation in LSB galaxies generally does not occur in the giant molecular clouds seen in more visible spirals.

With this in mind, we examined our results for evidence that differences in stellar populations between LSB and HSB galaxies could account for the large differences in Tully-Fisher scatter. Figure 4.6 shows the residuals in B , R , and

I plotted against $B-R$ and $B-I$. As can be seen there, the R and I residuals are uncorrelated with color for either the LSB or Ursa Major galaxies; the parametric and nonparametric correlation coefficients are R : (0.19; 0.25) and I : (0.19; 0.31) for the restricted LSB sample, and R : (0.37; 0.32) and I : (0.20; 0.20) for the Ursa Major sample. However, B residuals are modestly correlated with color in both galaxy samples; the coefficients for the B vs. $B-R$ correlation are restricted LSB: (0.40; 0.42) and Ursa Major: (0.59; 0.56), and the coefficients for the B vs. $B-I$ correlation are LSB: (0.59; 0.66) and Ursa Major: (0.59; 0.59). The sense of these correlations is that increasing redness of color is weakly associated with more severe underluminosity. Figure 4.7 shows the $B-R$ color as a function of profile width for the LSB and Ursa Major samples, with best-fit straight lines drawn to highlight the general trend in each sample. Both samples get redder with increasing profile width, but the mean color for the LSB sample of $B-R = 0.87$ is 0.16 mag bluer than the mean color for the Ursa Major sample of $B-R = 1.03$ (the standard error of the mean for each sample is 0.03 mag). Pierce & Tully (1992) noted a similar difference in $B-I$; they found the Ursa Major galaxies to be about 0.25 mag redder on average than their six local calibrator galaxies. These differences suggest that the stellar populations found in the Ursa Major sample are different, possibly due to a deficiency of gas in the galaxies inhabiting the dense cluster environment. However, the similarity and weakness of correlations of residuals against color for the LSB and Ursa Major samples suggest that any differences in stellar populations between the two samples probably do not account for the differences in their scatters in the Tully-Fisher plane.

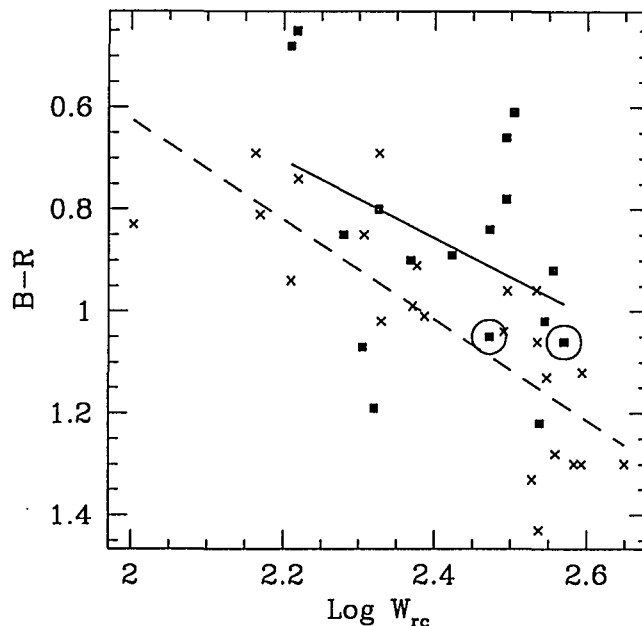


Figure 4.7: $B-R$ total galaxy color as a function of H I profile width for the LSB spiral galaxies (dark squares) and the Ursa Major comparison sample (crosses). The open circles mark the LSB galaxies excluded from the “restricted” sample because of their radii. The solid line shows the best-fit straight line for the LSB galaxies, and the dashed line shows the best-fit straight line for the Ursa Major galaxies.

4.5 Conclusions

We have reported total magnitudes and H I profile widths for a sample of field LSB spiral galaxies, and have compared these results to those of more visible galaxies using the familiar Tully-Fisher relation. We find that the field LSB spirals generally follow the same Tully-Fisher relation as more visible galaxies in the Ursa Major cluster, albeit with a considerably higher scatter. This similarity suggests that the LSB spirals examined here generally have similar total M/L ratios to those of the Ursa Major spirals, although the higher scatter suggests that the range of M/L ratios may be larger among LSB galaxies. We also find that both the LSB and Ursa Major samples fall along substantially different Tully-Fisher relations from

that defined by a sample of field galaxies in the direction of the Coma cluster, but we can find no convincing explanation for the difference.

Among the LSB galaxies, the weak trend of Tully-Fisher residuals to increase with increasing gas richness suggests that differences in evolutionary status among LSB galaxies may account for some part of the higher scatter. Differences in luminosity-profile width correlations among the B , R and I filters suggest that differences in stellar populations may also play a role. Further, a relation between M_{HI} and profile width that, while modest, is stronger than the B Tully-Fisher relation, suggests that atomic gas may be a larger fraction of total mass for LSB galaxies than for the Ursa Major comparison sample. Finally, the two giant Malin 1-class LSB spirals for which suitable data are available are both substantially overluminous for their rotation speeds, a fact that is difficult to reconcile with their low luminosity densities and presumed long cooling timescales.

Chapter 5

PROPERTIES OF THE CLASS OF GIANT LOW SURFACE BRIGHTNESS SPIRAL GALAXIES

We have obtained CCD surface photometry and optical spectroscopy for a sample of eight giant low surface brightness (LSB) spiral galaxies discovered in the course of a large survey for LSB galaxies. We find that these LSB giants have disks of larger scale length and lower central surface brightness than other spiral galaxies, although none has parameters as extreme as the prototype Malin 1. We find that the integrated colors of these LSB giants are redder than the integrated colors of smaller LSB galaxies, and that the LSB galaxies of all sizes follow a relation between redder colors and increasing disk scale length. Two of these eight LSB giants have active nuclei with the broad permitted lines characteristic of a Seyfert 1 nucleus, and one has the narrow lines of a Seyfert 2. The colors and absorption line indices of the bulges of these giants are indistinguishable from those of HSB spirals, suggesting that their bulges have similar stellar populations and evolutionary histories. We also

observed four and detected three of these galaxies in the 21 cm line of H I. These LSB giants generally have high total H I masses, although none is as extreme as Malin 1. Finally, the small-scale environments around these galaxies reveal several nearby companions. These LSB giants are at least as likely as smaller LSB galaxies to have close companions, and their average number of neighbors approaches that of HSB galaxies.

5.1 Introduction

Ever since the earliest searches for low surface brightness (LSB) galaxies (see Longmore et al 1982), some of the most interesting discoveries have come quite by accident. Impey et al. (1988) were looking for LSB dwarf galaxies in the Virgo cluster when they discovered the largest spiral galaxy yet known, Malin 1, whose properties are described by Bothun et al. (1987) and Impey & Bothun (1989). Malin 1's disk has a projected *central* surface brightness of $\mu_B(0) = 26.5 \text{ mag arcsec}^{-2}$, which is fainter than the limiting detection isophote of most surveys based on ordinary Schmidt camera survey plates. It was found only because Impey et al. (1988) happened to be looking in the right direction with deep IIIa-J plates that were photographically amplified to enhance LSB features. Without the amplification, only the prominent bulge would have been visible, and Malin 1 would likely have been dismissed as an ordinary background elliptical. Similarly, Davies et al. (1988) were conducting a deep CCD survey for very LSB galaxies in the cluster A1367 when they discovered GP 1444 on one of their nearby "blank" sky fields that had been taken for use as a secondary flat-field. GP 1444 has a projected disk central surface brightness of $\mu_R(0) = 26.2 \text{ mag arcsec}^{-2}$, but its physical scale length is

not known because no redshift has yet been measured. Since then, two “Malin 1 cousins” have been discovered through deliberate searches for LSB objects. F568-6, described by Bothun et al. (1990), was found during a visual search for LSB galaxies on the POSS-II plates by Schombert & Bothun (1988), and 1226+0105, described by Sprayberry et al. (1993), was found in a visual-plus-machine-scan search of UK Schmidt Telescope survey plates. All four galaxies have normal bulges and very LSB disks. In addition, Malin 1, F568-6 and 1226+0105 have physically large disks with L^* or greater total luminosities despite their very low luminosity densities. All three also have large H I masses and normal or higher ratios of M_{HI}/L_B .

The discovery of such objects raises a number of interesting questions about galactic formation and evolution: Under what conditions do such galaxies coalesce? What kinds of stars populate such low-density disks? Are the mass densities as low as the luminosity densities? How does the local environment affect the evolution and appearance of the disk? Most of these questions can be best addressed statistically, by examining a fair sample of giant LSB disk galaxies to determine typical properties. In this paper, we present a sample of eight giant LSB spiral galaxies, culled from a much larger set of LSB galaxies of all sizes developed through our visual-plus-automated search of UK Schmidt survey plates in the region defined by $-3^\circ \leq \delta \leq 3^\circ$ and $|b| \geq 30^\circ$ (this survey will hereafter be referred to as the “APM survey”). We also use this sample to begin the process of answering some of these questions. In Section 5.2, we describe the sample and how it was selected from the larger set of LSB galaxies. Section 5.3 lays out the surface photometric data and includes our analysis of the profiles and colors of the giant LSB spirals. Section 5.4 presents our 21 cm H I observations of three of these giant disks and compares the results to the properties of disks with higher surface brightness. Section 5.5 presents the data developed from optical spectroscopy. Section 5.6 contains our analysis of the small-scale

environments of these giant disks and compares those results to an earlier analysis of the environments around LSB galaxies generally. Finally, Section 5.7 summarizes our conclusions. Throughout this paper, all distance-dependent quantities are calculated assuming $H_0 = 100 h_{100} \text{ km s}^{-1} \text{ Mpc}^{-1}$ and $q_0 = 0.5$.

5.2 Discovery and Selection

The galaxies described here were discovered as part of the APM survey for LSB galaxies in 786 deg^2 centered on the celestial equator. The details of this survey are described in Chapter 2. Those aspects pertinent to the discovery of giant LSB disks are described in Sprayberry et al. (1993). We performed followup observations of a morphologically representative subset of the objects found in this survey, obtaining optical spectra of 264 of the survey galaxies, H I profiles of 190, and CCD images of 112. In order to focus on the properties of the giant LSB disks, we chose an empirical but arbitrary cutoff that separated the giant LSB disks from the higher surface brightness disks typically found in other field surveys. This paper discusses all galaxies having a “diffuseness” index defined as $\mu_B(0) + 5 \log(\alpha^{-1}) > 27.0$, where $\mu_B(0)$ is the disk B central surface brightness in mag arcsec^{-2} and α^{-1} is the disk scale length in h_{100}^{-1} kiloparsecs (see Figure 5.3). This cutoff eliminates many of the galaxies found by our LSB survey, but it ensures a homogenous sample of objects with very large, very low surface brightness disks. The galaxies chosen by this selection are listed in Table 5.1. We note that this list includes 1226+0105, which was previously described by Sprayberry et al. (1993). We have included it in all the discussions here as well because it is a member of the sample of giant LSB disks found through our APM survey. There are small differences between the values for

Table 5.1: Giant LSB Disk Galaxies

Name (1)	RA (2)	Dec (3)	v_{hel} (4)	B_T (5)	M_B (6)	$B - V_T$ (7)	$V - R_T$ (8)
0052-0119	0:52:35.5	-1:19:01	13197	14.76 ± 0.05	-20.91	0.80 ± 0.07	0.36 ± 0.07
0221+0001	2:21:27.5	+0:01:33	37263	16.70 ± 0.02	-21.37	0.70 ± 0.02	0.38 ± 0.01
0237-0159	2:37:38.7	-1:59:18	12701	15.47 ± 0.04	-20.12	0.92 ± 0.05	0.57 ± 0.04
0400+0149	4:00:12.6	+1:49:36	3817 ^a	13.97 ± 0.02	-18.96
1034+0220	10:34:52.9	+2:20:57	21335	16.40 ± 0.04	-20.37	0.73 ± 0.05	0.51 ± 0.05
1226+0105	12:26:39.2	+1:05:39	23655 ^a	16.10 ± 0.07	-20.90	0.65 ± 0.09	0.45 ± 0.06
1300+0144	13:00:42.6	+1:44:12	12264 ^a	17.48 ± 0.03	-18.03	0.53 ± 0.04	0.62 ± 0.04
2327-0244	23:27:58.2	-2:44:18	9520	14.48 ± 0.01	-20.46	0.73 ± 0.01	0.58 ± 0.01

Notes:

Columns (2) and (3): Coordinates are for the 1950.0 equinox.

Column (4): Heliocentric velocity in km s^{-1} .

Column (5): Total apparent B magnitude.

Column (6): Absolute B magnitude assuming $H_0 = 100 h_{100} \text{ km s}^{-1} \text{ Mpc}^{-1}$.

Column (7): Total $B - V$ color.

Column (8): Total $V - R$ color.

^aThese velocities are derived from 21 cm spectroscopy and have uncertainties of $\sim 20 \text{ km s}^{-1}$. All other velocities are derived from low-resolution optical spectroscopy and have uncertainties of $\sim 250 \text{ km s}^{-1}$.

some of the parameters reported for this galaxy by Sprayberry et al. (1993) and those reported here; these difference are due to improved analysis techniques and are discussed in the text where relevant.

5.3 Photometric Properties

5.3.1 Observations and Data Reduction

CCD images were obtained at the Steward Observatory 2.3m telescope on Kitt Peak. Three different CCDs were used over the course of our survey: a TI 800×800 CCD, a Loral 2048×2048 CCD, and a Loral 800×1200 CCD. All three CCDs have 15 μm pixels, and all observations were performed in direct imaging mode with 2×2 on-chip binning to yield a pixel scale of 0.3 arcsec pixel⁻¹. All but one of the galaxies described here was observed through Johnson *B* and *V* and Kron-Cousins *R* filters; the galaxy 0400+0149 was observed only through the Johnson *B* filter. Standard stars from the lists of Christian et al. (1985), Odewahn et al. (1992), or Landolt (1992) were observed at intervals each night for photometric calibrations. Grayscale reproductions of the *B* CCD images appear in Figure 5.1.

The CCD images were bias-subtracted and flat-fielded using standard IRAF tasks. Photometric and structural parameters of the galaxies were then determined for all galaxies using the following steps. First, sky values and their uncertainties were measured using the corners of the image or four other large regions well away from the galaxy. Sky surface brightnesses in *B* ranged from 21.7 to 22.4 mag arcsec⁻². Second, the sky was subtracted from the image as a constant or as a flat plane if there was a smooth gradient in the background across the image. Third, elliptical isophotes were fit to the galaxy image. Fourth, a two-dimensional radial profile of average isophotal surface brightness versus isophotal semi-major axis was plotted, an exponential model was fit to regions of the radial profile that appeared to be well beyond any bulge or central condensation, and an $r^{1/4}$ model was fit over the central few isophotes to the difference between the measured profile

and the exponential model. Fifth, the total galactic intensity (*i.e.*, including both bulge and disk) was determined by summing the actual pixel intensities inside the outermost isophote, and then extrapolating the exponential fit only from this last isophote to infinity. This extrapolation typically increased the galactic magnitude by < 0.1 mag. Finally, the total intensity and surface intensities were transformed to total magnitude and surface brightnesses using zero points and color terms derived from the standard star observations.

Corrections for Galactic reddening were taken from the maps of Burstein & Heiles (1982) and k -corrections from the tabulations of Coleman et al. (1980). Surface brightnesses and magnitudes were corrected for cosmological expansion by factors of $(1+z)^4$ and $(1+z)^2$, respectively. These corrected total magnitudes are reported in Table 5.1. For those galaxies observed in B , V and R on the same night, the isophotes were fit only to one filter, and the same isophotes were used as elliptical apertures for summing intensities in the other filters. This procedure ensured that both the radial color profiles and the total colors of the galaxies are uniformly measured. One of the galaxies (0040+0149) was observed on the last night of the survey in B only, so there is no color information available for it. Each galaxy's inclination was estimated by taking the simple average of the ellipticities of those isophotes used in fitting the exponential disk model. This average was converted to an inclination angle assuming that an edge-on disk would have an intrinsic ellipticity of 0.8, using the method of Holmberg (1958).

5.3.2 Disk and Bulge Parameters

Figure 5.2 shows the radial surface brightness profiles for the eight giant LSB disks. The profiles and models are plotted without correction for inclination. The galaxy

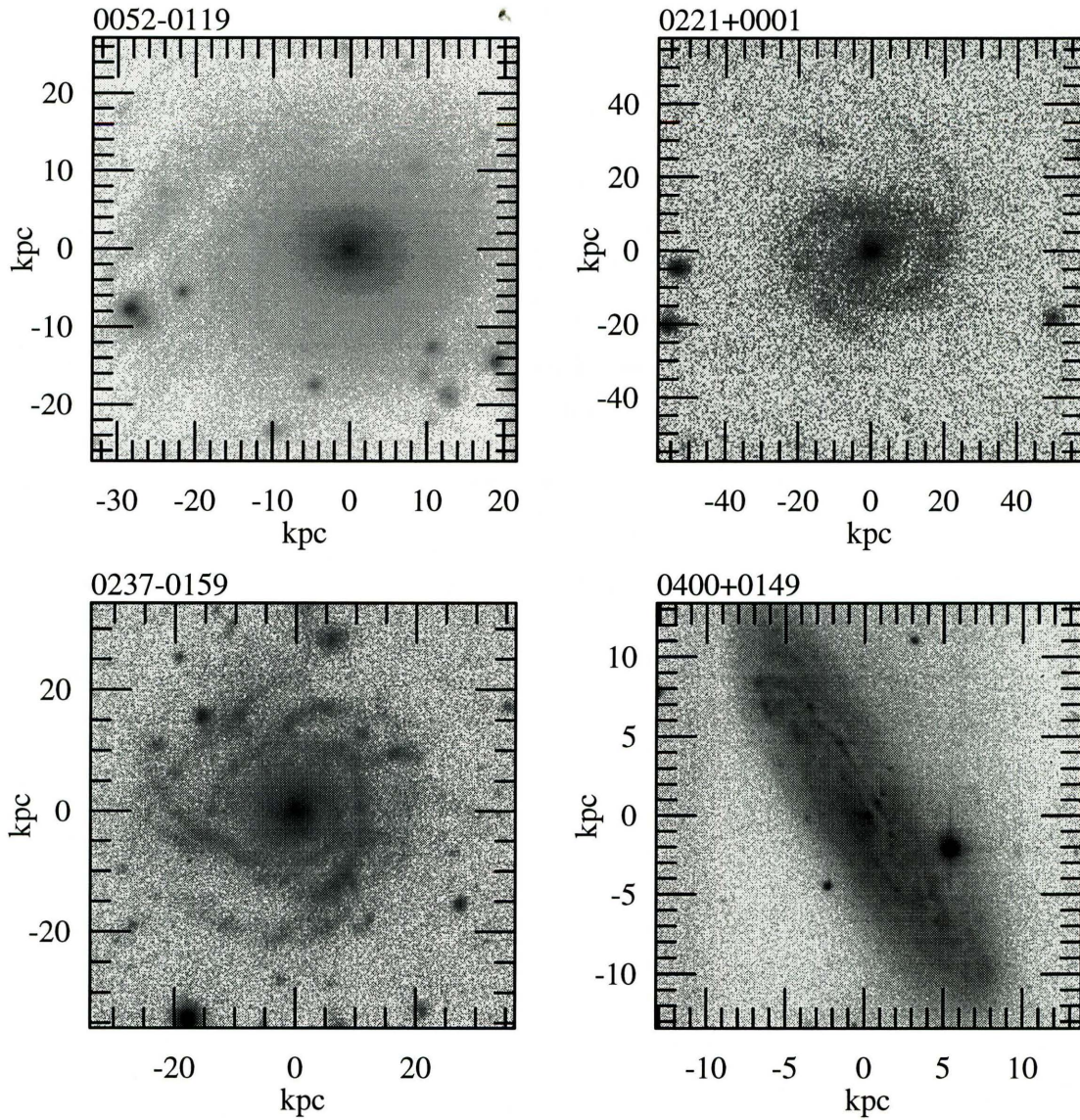


Figure 5.1: Grayscale reproductions of B CCD image sections showing giant LSB spirals. North is up, and East is to the left. Images are sky-subtracted and shown on a logarithmic intensity scaling to enhance the visibility of LSB features. Scale bars assume $H_0 = 100 h_{100} \text{ km s}^{-1} \text{ Mpc}^{-1}$ and $q_0 = 0.5$. The faintest visible features are about $25 \text{ mag arcsec}^{-2}$ due to the limitations of the reproduction technique.

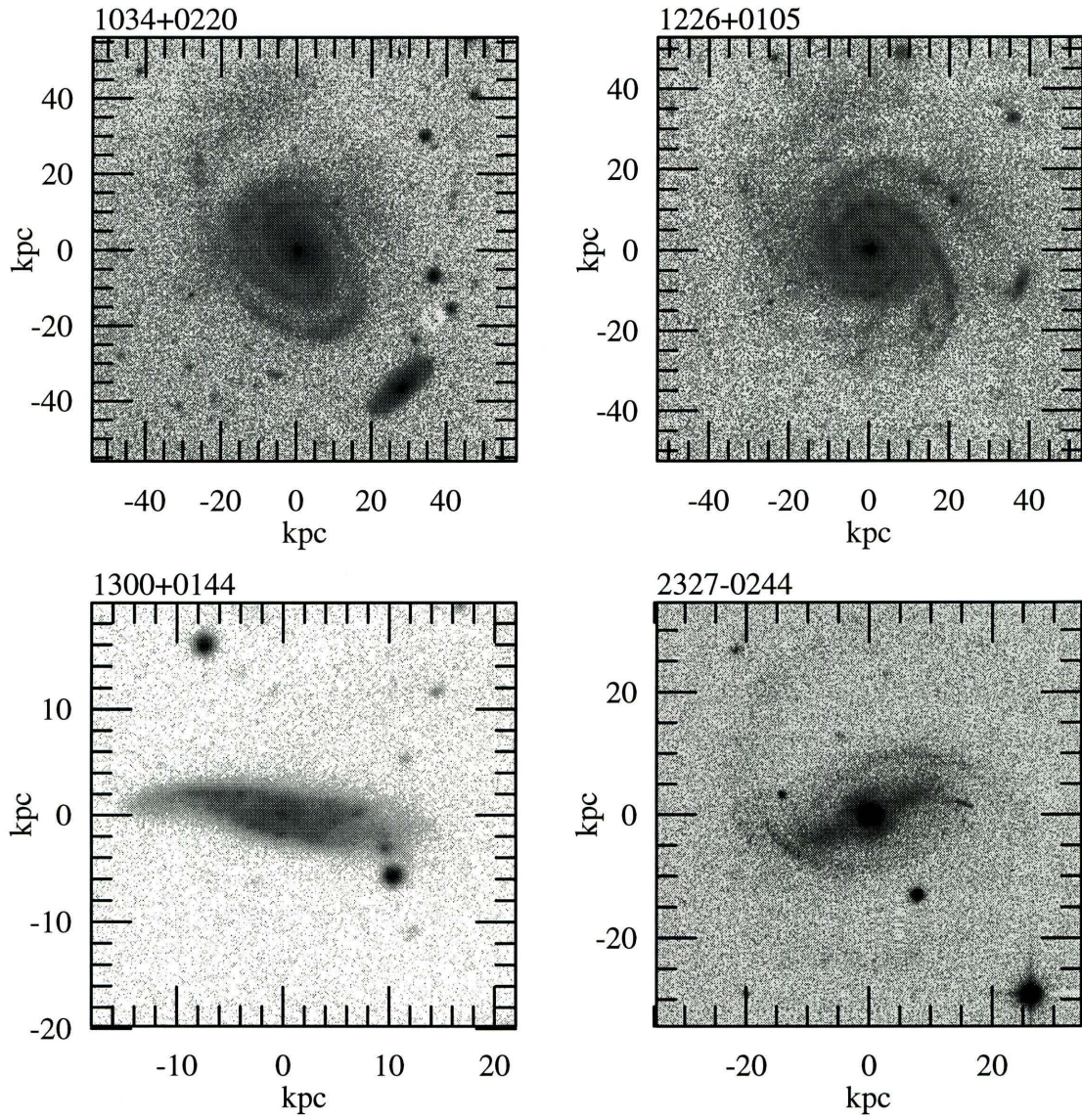


Figure 5.1: Continued.

1300+0144 is obviously not well fit by a simple bulge-disk model. Its measured profile appears at first glance to be concave upward over its entire length, suggesting that it is dominated by a large bright bulge. However, visual inspection shows the bulge to be quite small, extending only ~ 6 arcseconds from the center. This galaxy is very close to edge-on ($i = 71^\circ$), and it has a much larger degree of visible structure than any of the other eight galaxies. It exhibits two bright spiral arms, a faint bar, and a very LSB outer disk. We have chosen conservatively to fit the disk model to the range from 5 to 12 h_{100}^{-1} kpc, and to limit the bulge model fitting to the region interior to 4 h_{100}^{-1} kpc.

The model parameters are listed in Tables 5.2 and 5.3. For the disk components, we report the fitted central surface brightness $\mu_B(0) = \mu_B(r = 0)$ corrected for inclination, and the exponential scale length. For the bulge components, we report r_{eff} , the radius enclosing one-half the total bulge luminosity, and the effective surface brightness $\mu_B(r_{eff}) = \mu_B(r = r_{eff})$. The disk central surface brightnesses have been corrected for inclination by subtracting $2.5 \log(\cos i)$. This correction assumes no internal extinction within the disks. Additional corrections for internal extinction depend upon a model for the amount and distribution of dust within the disks, and we have no information on which to base such a model or to support a conclusion that these giant LSB disks follow similar models to those that hold for HSB spirals (see for example Giovanelli et al. 1994). No correction was applied to the bulge models because the bulges are assumed to be spheroidal and hence much less affected by inclination. Tables 5.2 and 5.3 also list the integrated colors of each component.

Accurate estimation of the sky value is critical when trying to measure surface brightnesses that are themselves a tiny fraction of the sky brightness. As long as the galaxy is significantly smaller than the CCD field of view (as is the case for all these

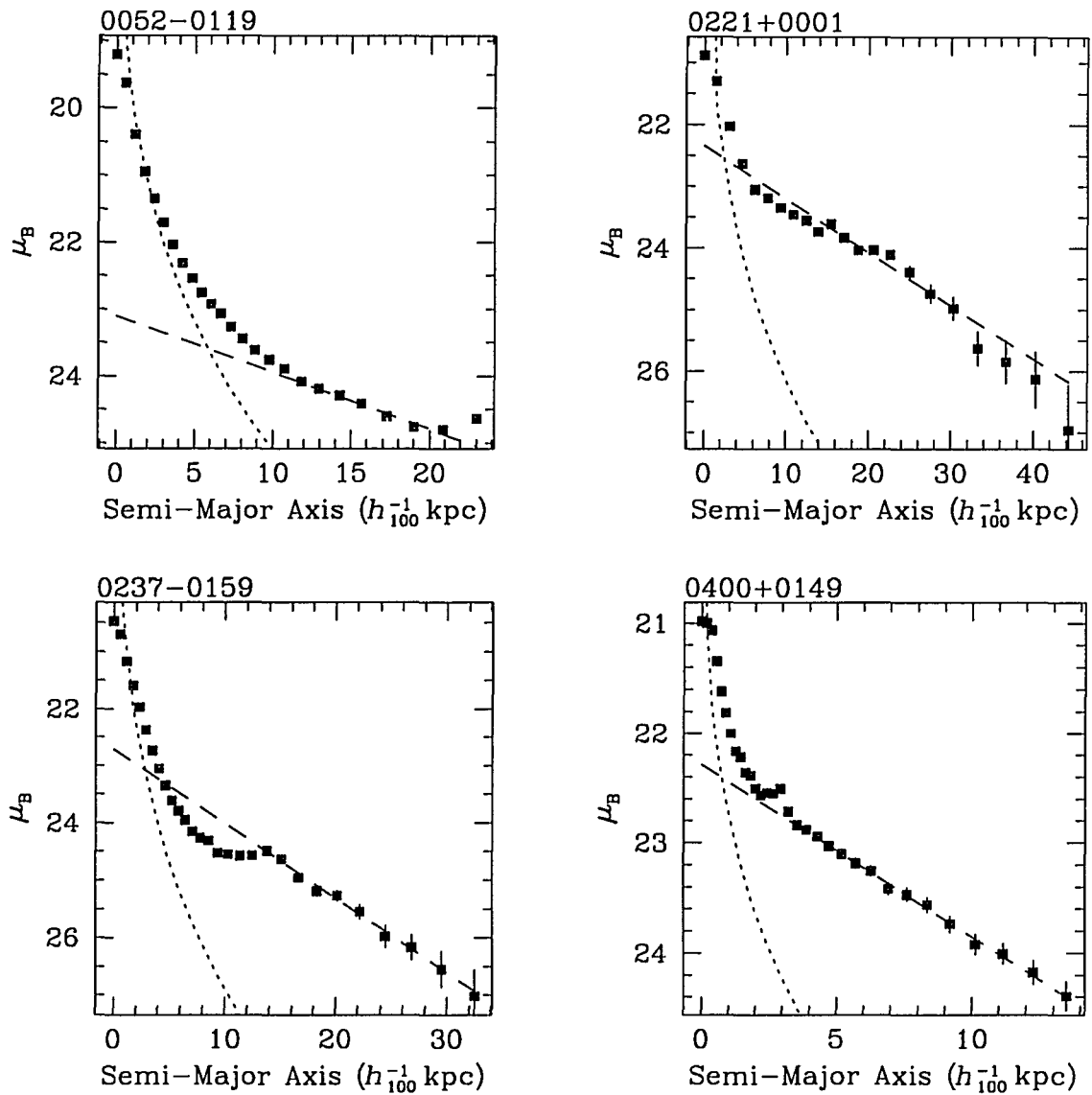


Figure 5.2: Radial surface brightness profiles for the eight giant LSB disk galaxies without adjustment for inclination. The error bars show the effect of the maximum plausible systematic error in the sky value. The fitted disk models are shown as dashed lines, and the fitted bulge models are shown as dotted curves.

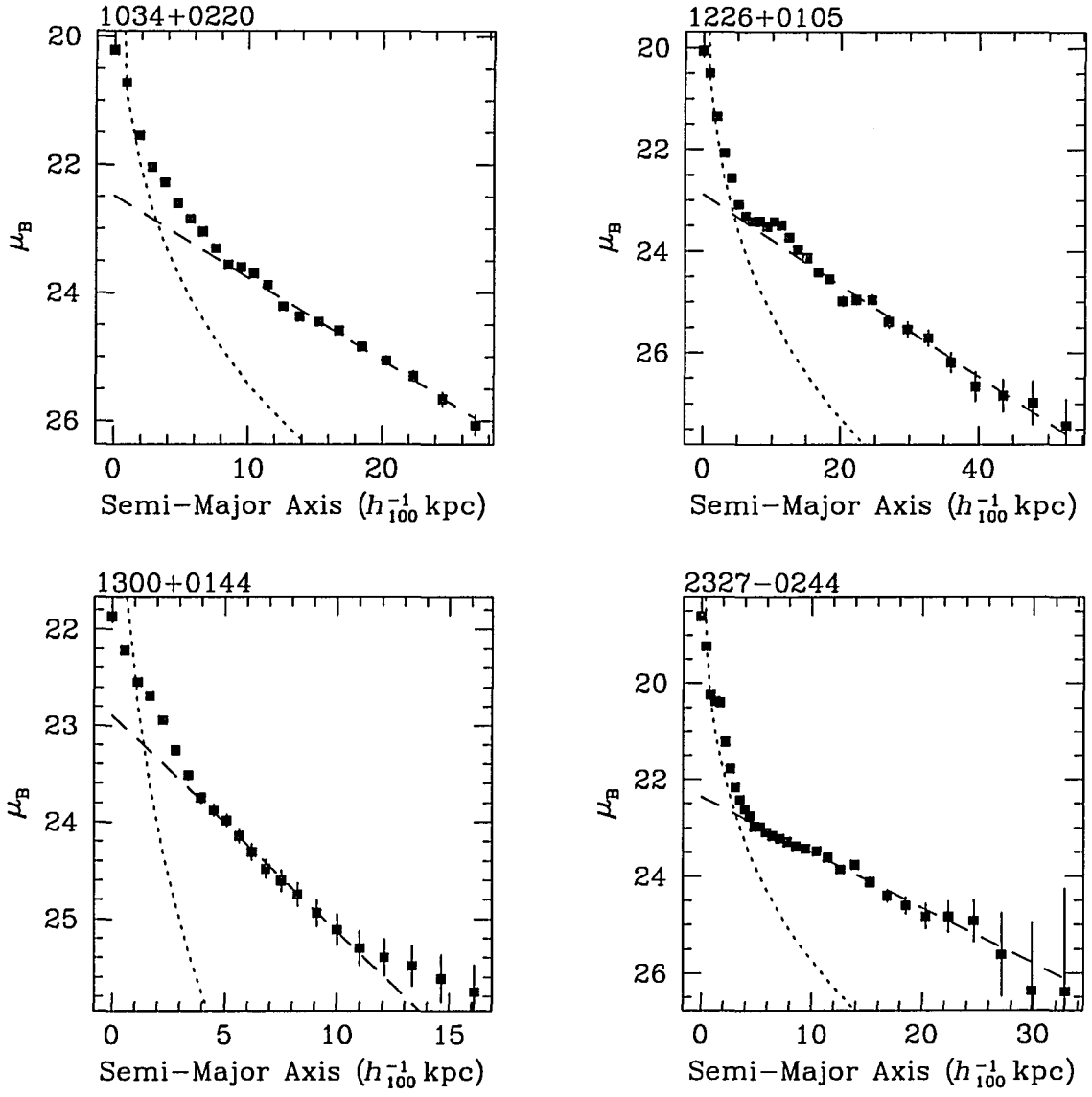


Figure 5.2: Continued.

Table 5.2: Disk Model Parameters

Galaxy (1)	$\mu_B(r=0)$ (2)	α^{-1} (3)	$B-V$ (4)	$V-R$ (5)	i (6)
0052-0119	23.40 \pm 0.09	12.84 \pm 0.82	0.76 \pm 0.29	0.34 \pm 0.30	40
0221+0001	22.63 \pm 0.04	12.51 \pm 0.28	0.65 \pm 0.09	0.41 \pm 0.05	40
0237-0159	22.98 \pm 0.06	8.34 \pm 0.18	0.69 \pm 0.12	0.51 \pm 0.12	38
0400+0149	24.03 \pm 0.02	6.95 \pm 0.08	78
1034+0220	22.94 \pm 0.07	8.43 \pm 0.24	0.60 \pm 0.16	0.45 \pm 0.16	49
1226+0105	23.33 \pm 0.14	12.10 \pm 0.58	0.50 \pm 0.26	0.48 \pm 0.18	48
1300+0144	24.17 \pm 0.04	4.85 \pm 0.12	0.63 \pm 0.12	0.57 \pm 0.12	72
2327-0244	23.16 \pm 0.01	9.47 \pm 0.08	0.88 \pm 0.03	0.60 \pm 0.02	61

Notes:

Column (2): Projected disk central surface brightness in B mag arcsec $^{-2}$.

Column (3): Disk exponential scale length in h_{100}^{-1} kpc.

Columns (4) and (5): Integrated total disk colors in magnitudes.

Column (6): Disk inclination in degrees.

Table 5.3: Bulge Model Parameters

Galaxy (1)	$\mu_B(r=r_{eff})$ (2)	r_{eff} (3)	$B-V$ (4)	$V-R$ (5)	B/D (6)
0052-0119	21.47 \pm 0.10	2.36 \pm 0.10	0.89 \pm 0.23	0.48 \pm 0.26	0.71
0221+0001	22.67 \pm 0.24	2.49 \pm 0.31	1.56 \pm 0.48	0.62 \pm 0.16	0.14
0237-0159	21.17 \pm 0.19	1.23 \pm 0.10	1.05 \pm 0.35	0.62 \pm 0.14	0.42
0400+0149	26.32 \pm 0.04	9.54 \pm 0.30	0.83
1034+0220	23.66 \pm 0.07	4.66 \pm 0.18	1.24 \pm 0.17	0.30 \pm 0.12	0.57
1226+0105	22.82 \pm 0.13	3.59 \pm 0.20	0.89 \pm 0.25	0.51 \pm 0.13	0.51
1300+0144	22.99 \pm 0.60	1.25 \pm 0.32	0.85 \pm 0.45	0.86 \pm 0.37	0.71
2327-0244	22.14 \pm 0.04	2.38 \pm 0.05	0.72 \pm 0.09	0.00 \pm 0.07	0.59

Notes:

Column (2): Bulge effective surface brightness in B mag arcsec $^{-2}$.

Column (3): Bulge effective radius in h_{100}^{-1} kpc.

Columns (4) and (5): Integrated total bulge colors in magnitudes.

Column (6): Bulge-to-disk luminosity ratio.

objects), the ability to measure the sky accurately is largely limited by the accuracy with which the CCD images can be flat-fielded. The sky intensity in these images was estimated by finding the modes of the pixel intensity distributions in the four corners or other regions well away from the galaxy, discarding the highest and lowest of these four values, and then adopting the average of the remaining two values as the sky intensity. This procedure allowed us to make a rough estimate of the remaining flat-fielding error from the difference between the adopted sky intensity and the most distant extremum among the four modal values. This difference was adopted as the maximum systematic error in the sky intensity. The profiles in Figure 5.2 are marked to show the effects of systematic errors in the sky estimate. The error bars indicate the systematic effect on the profile of changing the sky level estimate by the maximum likely error, as determined by the difference between the adopted sky intensity and the most extreme outlier among the four corner values. The sizes of these error bars reflect to a large extent the accuracy of the flat-fielding on the individual images. The estimated possible systematic error was typically $0.1\% \sim 0.3\%$ of the sky level. The internal uncertainties in the surface brightnesses are smaller than the point sizes.

Tables 5.2 and 5.3 show that these galaxies are indeed both LSB and large. The average B central surface brightness $\mu_B(0)$ of the giant LSB disks is 23.2 ± 0.2 mag arcsec $^{-2}$, and the average scale length α^{-1} is 9.8 ± 1.1 h_{100}^{-1} kpc. In contrast, the field survey of Kent (1985) found for Hubble types Sa–Sd an average $\mu_B(0)$ of 21.6 ± 0.1 mag arcsec $^{-2}$ and an average scale length of 3.3 ± 0.3 h_{100}^{-1} kpc. These giant LSB disks are on average 2σ fainter in $\mu_B(0)$ and 3σ larger in scale length than galaxies found in standard catalogs like the NGC. Figure 5.3 illustrates this difference. The other galaxies plotted are from field surveys by Kent (1985), van der Kruit (1987), and de Jong & van der Kruit (1994), and from other studies of

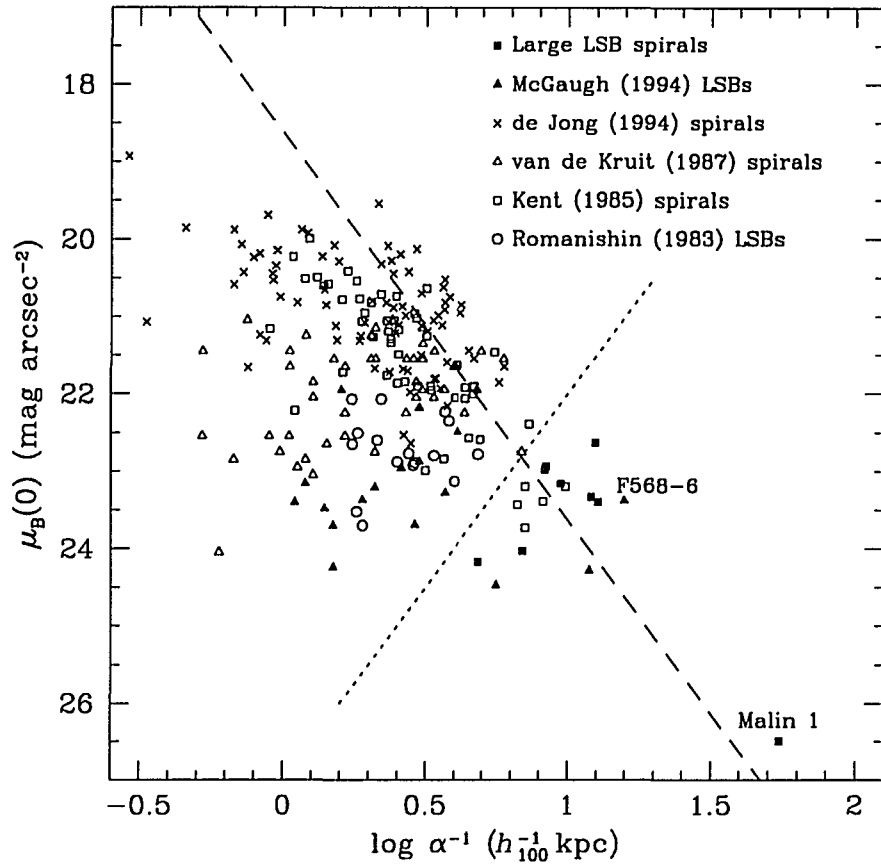


Figure 5.3: Central surface brightness as a function of scale length for six samples of disk galaxies. The dotted line marks the cutoff in “diffuseness index” of $\mu_B(0) + 5 \log(\alpha^{-1}) = 27.0$ used to define a giant LSB disk. The dashed line is a line of constant disk luminosity set to the assumed parameters of an L^* disk, $\mu_B(0) = 21.65 \text{ mag arcsec}^{-2}$, $\alpha^{-1} = 3.5 h_{100}^{-1} \text{ kpc}$, and $M_B = -19.7$.

LSB galaxies by Romanishin et al. (1983) and McGaugh & Bothun (1994). We note that Kent (1985) reported only r band surface photometric information; we converted his results to B using the color term recommended by Kent (1984). Since de Jong & van der Kruit (1994) did not derive central surface brightnesses and scale lengths, we calculated those quantities from the magnitude, D_{25} (diameter at the 25 mag arcsec $^{-2}$ isophote), and μ_{UGC} (surface brightness at the UGC diameter) values they reported. We checked our calculations by comparison of the derived

disk parameters to their published profiles, and we dropped the galaxies where the calculations appeared to be significantly affected by irregularities in the profile shapes. We have also indicated the positions of two previously reported examples of giant LSB disks using the information from Bothun et al. (1987) for Malin 1 and the information from McGaugh & Bothun (1994) for F568-6. The dotted line depicts the cutoff in “diffuseness index” $\mu_B(0) + 5 \log \alpha^{-1} > 27.0$ used to define a “giant LSB disk.” The dashed line is a line of constant disk luminosity, set to the assumed disk parameters of an L^* spiral galaxy of $\mu_B(0) = 21.65 \text{ mag arcsec}^{-2}$ and $\alpha^{-1} = 3.5 h_{100}^{-1} \text{ kpc}$ from Bothun et al. (1990). These parameters yield a disk $M_B = -19.7$, which is the value of an L^* galaxy disk derived by Efstathiou et al. (1988) for our adopted distance scale. We note that three of the LSB galaxies studied by McGaugh & Bothun (1994) (including F568-6) and five of the NGC galaxies studied by Kent (1985) qualify as giant LSB disks under the definition used here; these galaxies and their pertinent parameters are listed in Table 5.4.

Figure 5.3 shows that the giant LSB disks fall within the range of luminosity defined by the higher surface brightness disks; it is their luminosity *densities* that are extraordinary. Bothun et al. (1990) found a B luminosity density within one scale length of $15 h_{100}^2 L_\odot \text{ pc}^{-2}$ for F568-6, Sprayberry et al. (1993) reported a B density within one scale length for 1226+0105 of $10 h_{100}^2 L_\odot \text{ pc}^{-2}$, and Bothun et al. (1987) found that Malin 1 had a *central* B density of only $3 h_{100}^2 L_\odot \text{ pc}^{-2}$. In contrast, the canonical L^* disk has a B luminosity density within one scale length of $75 h_{100}^2 L_\odot \text{ pc}^{-2}$. If the disk M/L_B ’s of these giant LSB disks are comparable to that of an L^* disk, then the implied mass densities would also be very low. Arguments originally made by Quirk (1972) and Talbot & Arnett (1975) and later supplemented by Kennicutt (1989) and Impey & Bothun (1989) suggest that disk evolution will be quite slow at such low mass densities. However, the M/L_B ’s of

Table 5.4: Giant LSB Spiral Galaxies From Other Studies

Galaxy (1)	B_T (2)	M_B (3)	$\mu_B(0)$ (4)	α^{-1} (5)	Reference (6)
UGC 6614	14.43	-19.67	24.28	11.9	McGaugh & Bothun (1994)
F568-6	14.57	-21.17	23.38	15.8	McGaugh & Bothun (1994)
UGC 9024	14.74	-17.84	24.47	5.6	McGaugh & Bothun (1994)
NGC 2770	12.94	-18.47	23.20	9.8	Kent (1985)
NGC 4017	13.03	-19.62	23.20	10.0	Kent (1985)
NGC 5533	13.88	-19.10	23.73	7.1	Kent (1985)
NGC 5905	13.00	-19.75	23.39	8.2	Kent (1985)
NGC 5987	13.24	-19.26	23.43	6.7	Kent (1985)

Notes:

Column (2): Total extrapolated magnitude of disk only.

Column (3): Absolute magnitude of disk only, assuming $H_0 = 100 \text{ } h_{100} \text{ km s}^{-1} \text{ Mpc}^{-1}$.

Column (4): Disk B central surface brightness in mag arcsec^{-2} .

Column (5): Disk scale length in $h_{100}^{-1} \text{ kpc}$.

giant LSB disk galaxies are uncertain; different studies have found that they can have both higher (Romanishin et al. 1982) and lower (Chapter 4) M/L 's than normal galaxies. Clearly, further work is needed on the mass-to-light ratios of these giant disks.

Figure 5.3 also illustrates the extraordinary nature of Malin 1. To date only one galaxy with a lower central surface brightness has been reported. Davies et al. (1988) measured $\mu_R(0) = 26.2$ for GP 1444, but they could not determine its physical scale length because no redshift has been measured. All other giant LSB disks have substantially shorter scale lengths than Malin 1 and brighter central surface brightnesses. However, given the present state of the reported surveys for LSB galaxies, it is impossible to determine whether the gap in parameter space between Malin 1 and everything else truly reflects the underlying distribution of galaxies or is an artifact of the selection effects of galaxy surveys. Both Malin 1 and GP 1444 were found by accident, using detection systems significantly more sensitive to LSB features than standard Schmidt telescope photographic survey plates. Deep CCD surveys will be needed to fill in and perhaps extend the distribution of galaxy disks in this parameter space.

5.3.3 Colors

The average $B-V$ and $V-R$ colors for seven of our giant LSB disk galaxies (*i.e.*, all but 0400+0149, for which we did not obtain colors) are listed in Table 5.5, along with the average colors of three comparison sets from the literature. The colors for the giant LSBs and the set of de Jong & van der Kruit (1994) are the integrated colors as described in Section 5.3.1. The colors for the sample of McGaugh & Bothun (1994) are measured through a large isophotal aperture, and the colors

Table 5.5: Average Colors and Surface Brightness Parameters

Sample (1)	N (2)	$\langle B-V \rangle$ (3)	$\langle V-R \rangle$ (4)	$\langle \mu_B(0) \rangle$ (5)	$\langle \alpha^{-1} \rangle$ (6)
Giant LSB disks	7	0.73 ± 0.05	0.50 ± 0.04	23.23 ± 0.19	9.78 ± 1.09
McGaugh et al (1994)	12	0.49 ± 0.04	...	23.14 ± 0.20	3.29 ± 0.82
Romanishin et al (1983)	15	0.43 ± 0.04	0.60 ± 0.02	22.76 ± 0.12	2.82 ± 0.25
de Jong et al (1994)	30	0.75 ± 0.03	0.53 ± 0.02	21.08 ± 0.14	2.53 ± 0.23

Notes:

All uncertainties are σ/\sqrt{N} .

Column (2): Number of galaxies in the sample.

Columns (3) and (4): Average total integrated colors in magnitudes.

Column (5): Average projected disk central surface brightness in B mag arcsec $^{-2}$.

Column (6): Average disk exponential scale length in h_{100}^{-1} kpc.

for the set of Romanishin et al. (1983) are measured through fixed photoelectric apertures. For the sets of McGaugh & Bothun (1994) and Romanishin et al. (1983), only those galaxies that have both colors and disk model parameters are included in the color averages. The giant LSB disks are indistinguishable in both $B-V$ and $V-R$ from the set of de Jong & van der Kruit (1994) despite the differences in scale length and central surface brightness. In $B-V$ the giant LSB disks are considerably redder than the set of McGaugh & Bothun (1994) and slightly redder than the set of Romanishin et al. (1983). In $V-R$ the giant LSB disks are slightly bluer than the set of Romanishin et al. (1983).

Figure 5.4 shows $B-V$ color as a function of the “diffuseness index” for the four sets of galaxies. Here F568-6 is plotted using data from Bothun et al. (1990), as McGaugh & Bothun (1994) did not report colors for that galaxy. We note that the one giant LSB spiral for which McGaugh & Bothun (1994) did report colors, UGC 6614, has $B-V = 0.72$, exactly the same as the average of our seven giant

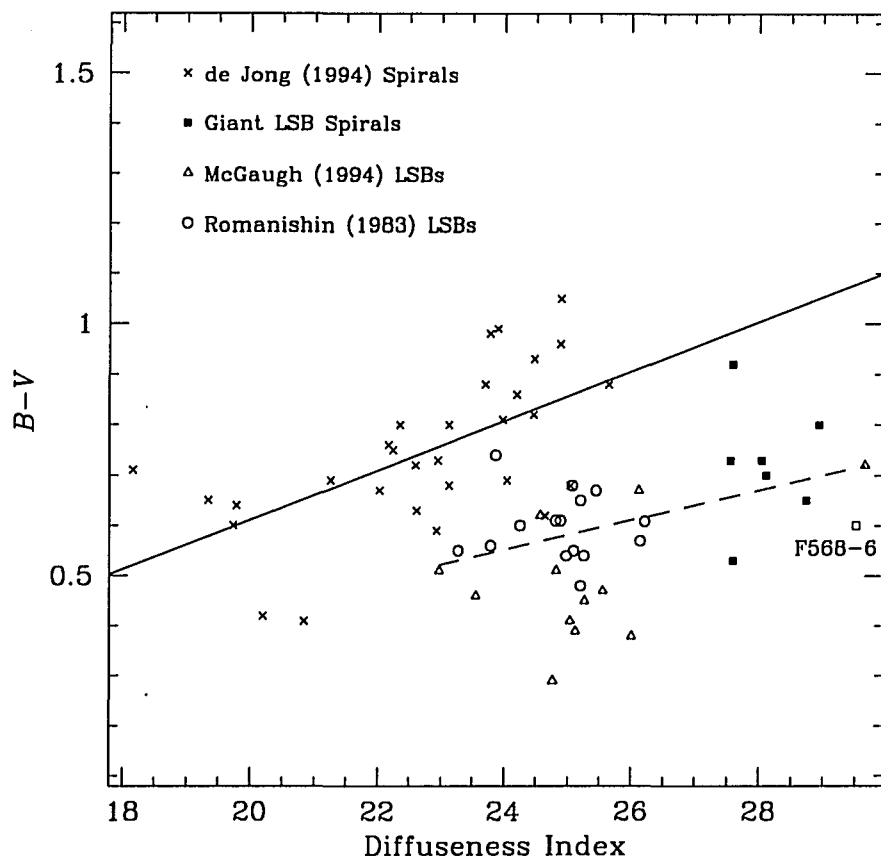


Figure 5.4: $B-V$ color as a function of diffuseness index for four samples of disk galaxies. The solid line shows the best-fit line to the data of de Jong & van der Kruit (1994), and the dashed line shows the best-fit line to the combined total of the three LSB samples.

LSB spirals with colors. The solid line is a least-squares fit to the same subset of the HSB sample of de Jong & van der Kruit (1994) that appeared in Figure 5.3, and the dashed line is a least-squares fit to the combination of the three LSB samples. Both HSB and LSB galaxies tend to be redder at larger values of the “diffuseness index,” although by definition the HSB and LSB galaxies overlap only over a small range of the “diffuseness index.” The typical separation between the two trend lines is $\Delta(B-V) = 0.28$, but this difference is only marginally significant. The rms scatters around the HSB and LSB trend lines are each 0.12 mag, respectively,

and their correlation coefficients are 0.61 and 0.39 at the 99.9% and 98% confidence levels, respectively. Nonetheless, there are clear suggestions in Figure 5.4 that LSB galaxies are in general about 0.25 mag bluer in $B - V$ than are HSB galaxies, and that galaxies of both types tend to be redder with increasing values of the “diffuseness index.”

The colors plotted in Figure 5.4 are the total colors for each galaxy, *i.e.*, they include both the disk and the bulge for each galaxy. Thus it might be supposed that the apparent trend is simply due to the increasing dominance of the generally red bulges as the disks become more diffuse. If this were the case, there should be correlations between the “diffuseness index” and the bulge-to-disk luminosity ratio B/D , or between the total galactic color and B/D . No such correlations are present: in both cases, and for all galaxy samples studied here that have suitable data, the confidence that the correlation is different from zero is always $\leq 40\%$.

It is also possible that this trend could be due to fading of the disks after star formation has mostly ended. However, as Figure 5.3 shows, the giant LSB spirals cover the same range of disk central surface brightness as the smaller LSB galaxies studied by McGaugh & Bothun (1994) and Romanishin et al. (1983). The giant LSB spirals have higher “diffuseness” indices solely because of their longer scale lengths. If the substantially redder colors (see Figure 5.4) of the LSB giants are due to fading, then they must have had considerably higher surface brightnesses in the past, and they must have formed no new stars for a long time. This scenario implies that these giant LSB spirals are quite different objects from smaller LSB galaxies, which are believed to have blue colors as a result of slow, continuous star formation (McGaugh & Bothun 1994).

McGaugh & Bothun (1994) discuss possible explanations for the generally blue

colors of LSB galaxies and conclude that the most likely explanation is a combination of late formation and slow but continuous star formation. This scenario can be generalized to explain the weak trend of redder color with increasing diffuseness seen in Figure 5.4. The giant LSB disks differ from the smaller LSB galaxies of McGaugh & Bothun (1994) in scale length but not in central surface brightness, implying that the large galaxies have similar densities but larger radii and larger total masses. The larger galaxies should therefore have somewhat longer collapse and formation timescales due to their longer free fall timescales. McGaugh & Bothun (1994) demonstrate in their Appendix that galaxies undergoing slow continuous star formation will be redder if they begin forming stars earlier, and the difference in turn-on time will determine the color difference. If LSB galaxies generally are undergoing slow continuous star formation, then giant LSB spirals thus should be redder than their smaller LSB counterparts because they have a larger proportion of older stars.

5.4 Neutral Hydrogen Properties

H I properties of three of these galaxies were measured by 21 cm observations at the 305m radio telescope of the Arecibo Observatory in May 1992 and January 1993. Data reduction and calibration were performed on-site using the observatory's standard GALPAC software package. H I profiles for the three galaxies appear in Figure 5.5, and their H I properties are summarized in Table 5.6 along with the properties of Malin 1 and F568-6 for comparison. One other galaxy, 1034+0220, was observed from Arecibo, but the observation was ruined by severe interference. The other four giant LSB spirals are either too far south or at too high a redshift

Table 5.6: HI Properties of Giant LSB Disk Galaxies

Galaxy (1)	v_{hel} (2)	W_0 (3)	Log M_{HI} (4)	D_{25} (5)
0400+0149	3817	499	9.49	3.17
1226+0105	23655	338	10.26	0.76
1300+0144	12264	397	9.98	0.55
Malin 1	24750	420	11.04	...
F568-6	13830	674	10.40	1.12

Notes:

Column (2): Heliocentric radial velocity in km s^{-1} . Uncertainties are $\approx 20 \text{ km s}^{-1}$.

Column (3): Corrected profile width in km s^{-1} . Uncertainties are $\approx 28 \text{ km s}^{-1}$.

Column (4): Log of H I mass in $h_{100}^{-2} M_{\odot}$. Uncertainties are ≈ 0.05 dex.

Column (5): Diameter at the 25 B mag arcsec $^{-2}$ isophote, in arcmin.

to be observed from Arecibo.

All three galaxies have profiles indicative of rotating spiral disks, although none exhibit the classic double-peaked structure. Following Haynes & Giovanelli (1984), we derived the corrected line width as $W_0 = [W_{50} + W_{20}] / [2(1+z) \sin i]$, where W_{50} is the width measured at 50% of the mean flux across the profile and W_{20} is the width measured at 20% of the peak flux. The line width given here for 1226+0105 differs slightly from that given by Sprayberry et al. (1993) due to an improved estimate of the inclination used here. The line width shown in Table 5.6 for Malin 1 is that given by Impey & Bothun (1989), and that for F568-6 is from Bothun et al. (1990).

The H I masses given in Table 5.6 for two of these galaxies should be regarded as lower limits because of the possibility that they have been partially resolved by the telescope beam. The D_{25} values given in Table 5.6 are the diameters at the $\mu_B = 25 \text{ mag arcsec}^{-2}$ isophote, and the H I disk is often considerably larger than the optical disk. The spirals studied by Szomoru et al. (1994) have an average H I-

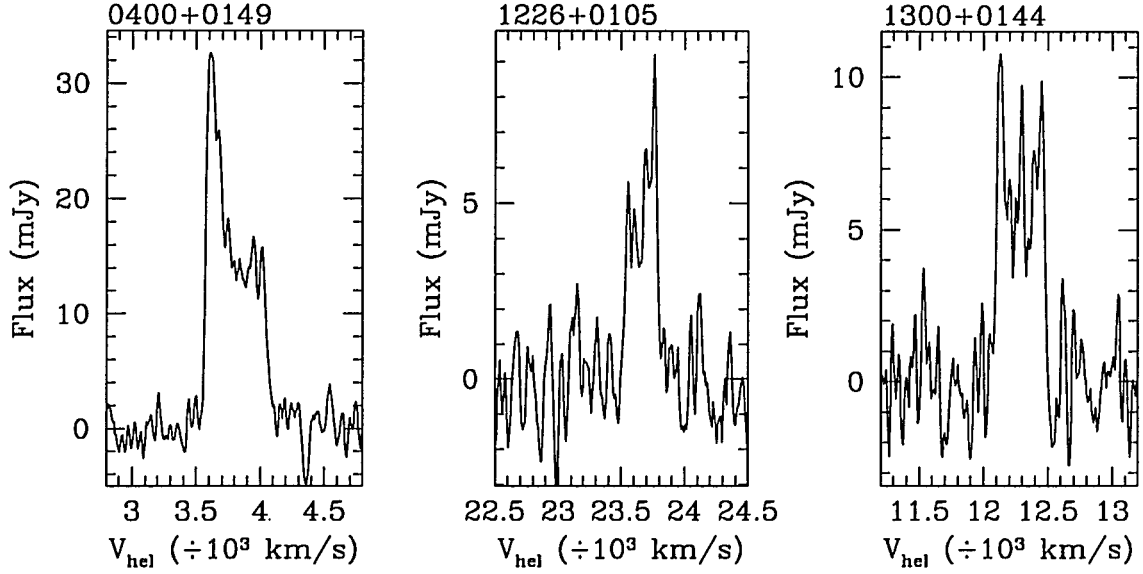


Figure 5.5: H I profiles for three of the giant LSB disk galaxies. All profiles have been smoothed to a resolution of $\approx 20 \text{ km s}^{-1}$ and baseline-subtracted. Velocities are heliocentric.

to-optical diameter ratio of $\langle D_{\text{HI}}/D_{25} \rangle = 2.5$, and van der Hulst et al. (1993) found a similar relationship for a sample of LSB galaxies drawn from the UGC. D_{25} for 0400+0149 is as large as the $3.3'$ Arecibo beam, so significant flux is clearly being missed if the H I disk extends past D_{25} . It is possible that the H I disk of 1226+0105 is also partially resolved, if it extends $\gtrsim 4$ times further than D_{25} .

We have plotted B luminosity against H I mass in Figure 5.6. Because of the likelihood that significant flux from 0400+0149 has been missed due to its large angular size, we have plotted both its measured position and the position it would have if its H I mass were two times larger. It is clear that the giant LSB disks generally have average or higher H I masses, and they tend to have low B luminosities for their gas masses, but only Malin 1 is truly exceptional in either regard.

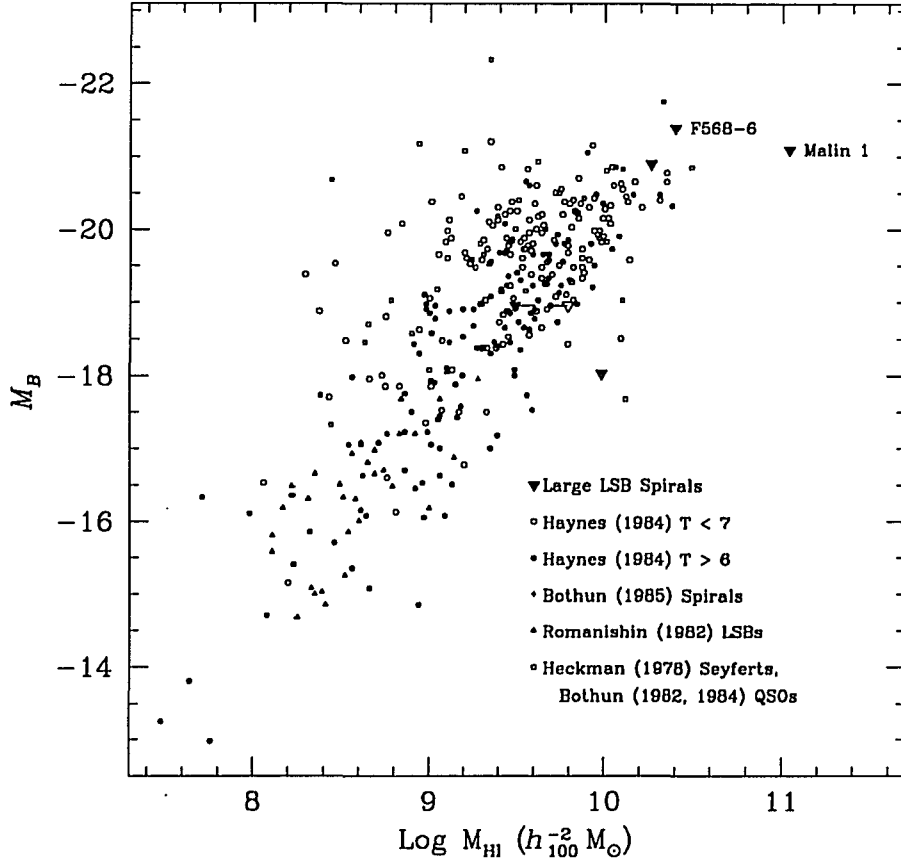


Figure 5.6: B absolute magnitude as a function of total gas mass. The dashed line connects the measured position of 0400+0149 (the solid triangle) with the position it would have if its H I mass were a factor of two larger (the hollow triangle). M_B and M_{HI} assume $H_0 = 100 \, h_{100} \, \text{km s}^{-1} \text{Mpc}^{-1}$.

5.5 Spectroscopic Properties

Low-resolution optical spectra were obtained of all eight giant LSB disk galaxies at the Multiple Mirror Telescope using the Red Channel Spectrograph. For all but one of the galaxies, the detector was a TI 800×800 CCD, and the instrumental setup used a $1.5'' \times 180''$ slit with the 150 line mm^{-1} grating. This configuration yields an effective resolution of $\sim 20 \, \text{\AA}$, with wavelength coverage from 3800 \AA to 7400 \AA . The galaxy 0221+0001 was observed with a Loral 800×1200 CCD as the detector,

which allowed use of the 300 line mm^{-1} grating. In conjunction with the $1.5'' \times 180''$ slit, the wavelength coverage was still 3800 \AA to 7400 \AA , but the effective resolution was $\sim 10 \text{ \AA}$. Exposure times ranged from 10 minutes to one hour. Several standard stars from the list of Massey et al. (1988) were observed each night. Data reduction and spectrophotometric calibration were accomplished with standard IRAF tasks. One-dimensional spectra were extracted from the two-dimensional longslit images using a variance-weighted sum of the pixels above sky along the spatial direction. The resulting spectra appear in Figure 5.7. All these spectra are of the galactic bulges; the low disk surface brightnesses render spectroscopy of the disks impossible at a 4-meter class telescope.

5.5.1 Emission Lines and Active Nuclei

The emission line fluxes and equivalent widths are summarized in Table 5.7. All three LSB giants previously described in the literature contain Seyfert 1 nuclei; the present sample includes one of those previously described AGN (the galaxy 1226+1015, see Sprayberry et al 1993) and two more objects that very likely are also AGN. The galaxy 2327–0244 shows broad $\text{H}\alpha$ emission with a FWZI of $\approx 11000 \text{ km s}^{-1}$, which places it near the middle of the range of line widths Seyfert 1 nuclei as described by Osterbrock (1977). The galaxy 0040+0149 also shows strong emission in $\text{H}\alpha$ and the forbidden lines of [O III] and [S II] in its nuclear spectrum. The FWZI of its $\text{H}\alpha$ line is $\approx 3800 \text{ km s}^{-1}$, suggesting that it is most likely a Seyfert 2.

The luminosity function of Meurs & Wilson (1984) predicts that only $\sim 2\%$ of galaxies with blue luminosities like those of these giant LSB disks should have Seyfert nuclei, and fewer 1% should have the broad lines characteristic of a Seyfert 1.

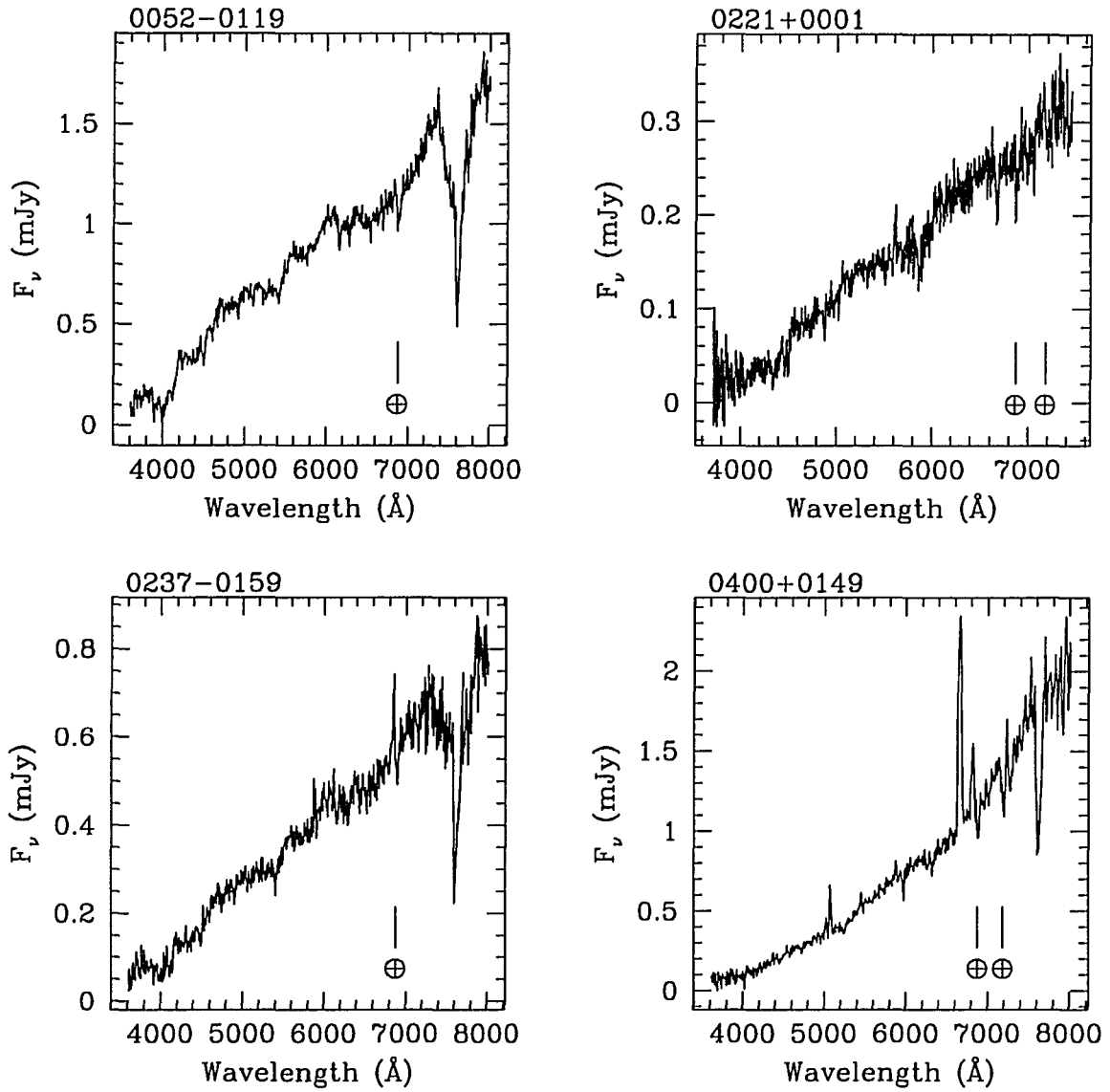


Figure 5.7: Optical spectra of the eight giant LSB galaxies. All spectra are of the bulge or central condensation. Observed wavelengths are plotted; absorption features due to Earth's atmosphere are marked. Resolution is ≈ 20 Å for all except 0221+0001, which has resolution of ≈ 10 Å.

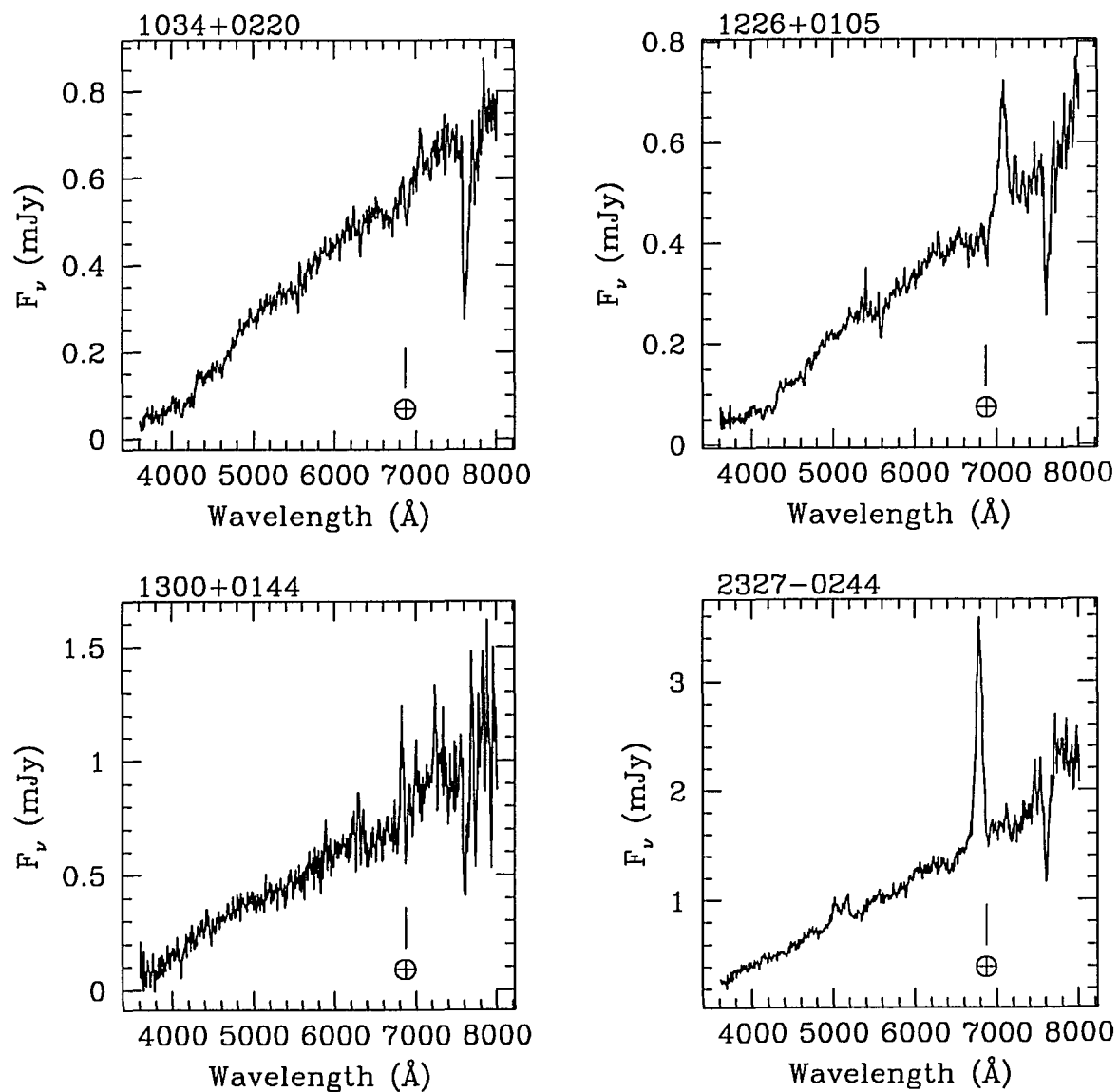


Figure 5.7: Continued.

Table 5.7: Emission Line Equivalent Widths and Fluxes

Galaxy	[O II]		[O III]		[O III]		H α		[S II]	
	Log f	EW	Log f	EW	Log f	EW	Log f	EW	Log f	EW
(1)	(2)		(3)		(4)		(5)		(6)	
0052-0119
0221+0001
0237-0159	-14.48	6.00
0400+0149	-14.55	7.76	-14.08	19.27	-13.38	56.70	-14.01	14.04
1034+0220	-14.76	11.05	-14.38	9.39	-14.77	3.84
1226+0105	-15.05	10.19	-14.97	4.39	-14.67	7.46	-13.75	53.79	-14.70	5.69
1300+0144	-13.85	32.65	-14.09	14.06
2327-0244	-14.57	3.46	-14.03	9.98	-12.91	116.10

Notes:

EW denotes equivalent width in Å. f denotes flux in units of $\text{erg cm}^{-2} \text{s}^{-1}$.

Column (2): Unresolved doublet $\lambda\lambda$ 3726, 3728.

Column (3): λ 4959.

Column (4): λ 5007.

Column (5): λ 6563. Includes any [N II] that may be present; resolution was not sufficient to separate H α from [N II].

Column (6): Unresolved doublet $\lambda\lambda$ 6716, 6730.

Here, out of a sample of ten galaxies (eight in this article plus Malin 1 and F568-6), there are four Seyfert 1's and one likely Seyfert 2. If these giant LSB disks were drawn from the same population as the galaxies used by Meurs & Wilson (1984) to derive their luminosity function, then the simple Poisson probability of finding five Seyferts out of a sample of ten would be $\sim 2.2 \times 10^{-6}$. Plainly, it is dangerous to draw sweeping conclusions from such a small sample. We tentatively conclude that active nuclei are much more common in giant LSB disk galaxies than in higher surface brightness disk galaxies. It is not clear why these giant disks should be especially prone to having active nuclei. Only one (2327-0244) has an obvious bar, so the predisposition is probably not based on morphology. They do tend to be rich in neutral hydrogen gas with reference to the published H I contents of HSB galaxies with similar disk luminosities, as Figure 5.6 shows, implying a large supply of fuel available for feeding the nucleus, but only Malin 1 is exceptional in this regard. Finally, the LSB giants are not unusually bulge-dominated. The average bulge-to-disk luminosity ratio for the LSB giants is 0.56 ± 0.07 , and the average for the spirals (types Sa-Sd) studied by Kent (1985) is 0.61 ± 0.20 . The presence of a bright nucleus undoubtedly aids in the identification of these LSB spirals, especially in eyeball scans of photographic survey plates, so this unusually high incidence may partly be due to a selection effect. The extent of this selection bias is not determinable from the present sample.

5.5.2 Absorption Lines and Metallicities

Table 5.8 lists the equivalent widths of the absorption features visible in the spectra, along with the magnitudes (defined as $-2.5 \log[S_v^f/S_v^c]$, where f and c refer to the feature and the adjacent continuum) of the CN 39 and Mg_b indices of

Table 5.8: Absorption Line Equivalent Widths and Indices

Galaxy	Ca II K λ 3934	Ca II H λ 3968	G band λ 4300	Mg I λ 5175	Na I D λ 5895	Mg _b	CN39
(1)	(2)	(3)	(4)	(5)	(6)	(7)	(8)
0052-0119	10.54	6.52	8.45	11.05	3.59	0.23	0.90
0221+0001	10.19	15.33	10.56	13.16	4.99	0.30	0.51
0237-0159	13.42	7.76	8.23	12.54	4.34	0.21	0.61
0400+0149	4.04	7.46	...	5.97	3.94	0.18	0.18
1034+0220	5.28	9.06	4.04	7.74	3.57	0.11	0.45
1226+0105	5.60	8.57	4.51	5.52	1.34	0.22	0.30
1300+0144	6.80	12.32	5.61	6.95	...	0.19	0.08
2327-0244	1.51	3.87	3.32	0.14	0.00

Notes:

Columns (2) — (6): Equivalent widths in Å.

Columns (7) and (8): Line indices in magnitudes, as defined by Boroson (1980).

Boroson (1980). Mould (1978) showed that the Mg_b index is sensitive to metallicity. Figure 5.8 shows the Mg_b index plotted against blue luminosity for the bulges of the giant LSB spirals, along with the comparable data for the ellipticals and the bulges of HSB spirals studied by Boroson (1980). The bulges of HSB and giant LSB spirals are indistinguishable from one another in the luminosity-metallicity plane. Figure 5.9 shows the CN 39 index plotted against the Mg_b index for the same three sets of galaxies. Again, the bulges of HSB and giant LSB spirals cover the same region of this parameter space. Both types of disks generally have CN 39 indices lower than those of the ellipticals at comparable levels of Mg_b.

The relative weakness of CN 39 indicates the presence of a blue continuum which dilutes this index more than Mg_b. Boroson (1980) proposed that this blue continuum came from a population of younger, hotter stars than were present in the ellipticals. While it appears likely from the photometric evidence in subsection 5.3.3

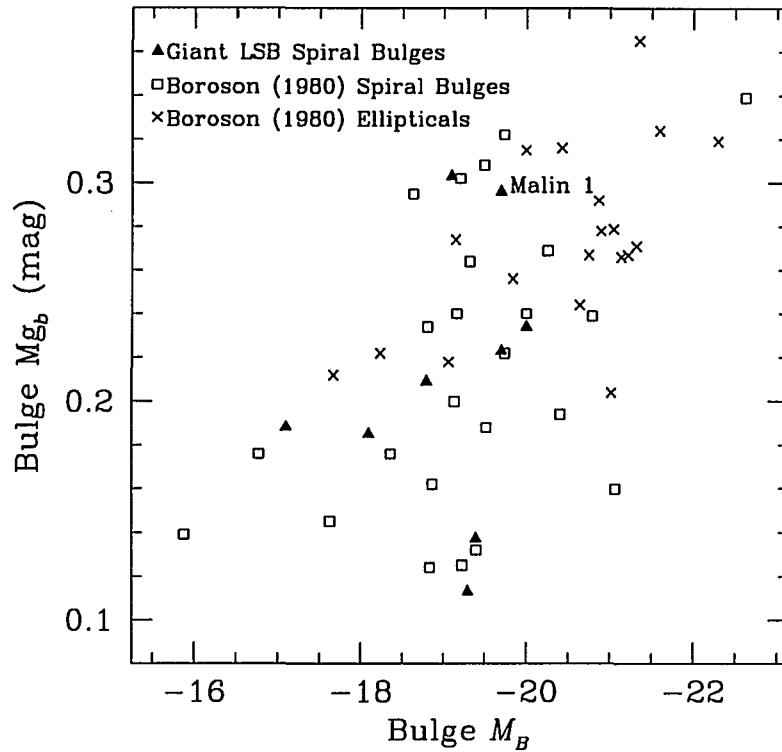


Figure 5.8: Bulge Mg_b plotted against bulge absolute magnitude for the giant LSB spirals and the spirals and ellipticals studied by Boroson (1980). The bulge absolute magnitudes assume $H_0 = 100 \text{ } h_{100} \text{ km s}^{-1} \text{ Mpc}^{-1}$.

that the giant LSB galaxies do include some younger stars in their population mix, two considerations make quantitative estimates of the proportion of blue stars very uncertain. First, a substantial fraction of these giant LSB spirals have active nuclei (subsection 5.5.1) which could provide an alternate source for the blue continuum in those objects. All of the LSB giants with AGN have weak CN 39, but there are other LSB giants with CN 39 as weak or weaker that do not have AGN. Second, as Burstein et al. (1984) made clear, the Mg_b index is sensitive to differences in age, CNO abundance, and hot star content as well as differences in metallicity. The strongest statement that can safely be made is that there are no apparent photometric or spectroscopic differences between the bulges of these giant LSB spirals and those of

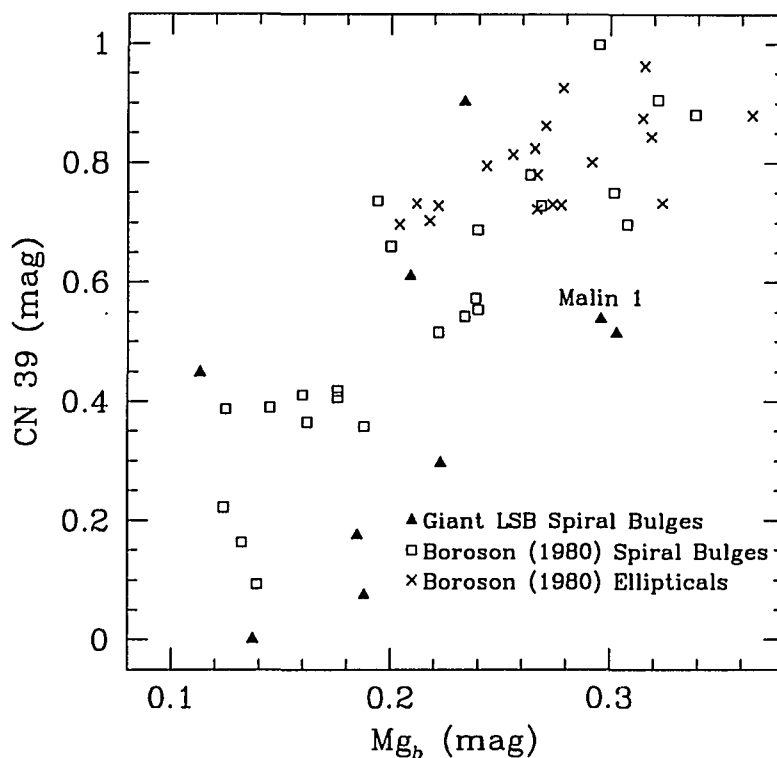


Figure 5.9: CN 39 plotted against Mg_b for the LSB spiral bulges, along with the HSB spiral bulges and ellipticals of Boroson (1980).

better studied HSB spirals. The differences noted in Section 5.3 must therefore be due entirely to differences in their disks and disk stellar populations.

5.6 Small Scale Environments

The influence of environment on the formation and evolution of LSB galaxies has been the subject of several recent papers. Hoffman et al. (1992) modeled the formation of giant LSB disks and concluded that such objects could only form as rare (3σ) high-density peaks surrounded by equally rare low-density background regions. Their models correctly predicted that these galaxies would have normal spiral bulges

and large unevolved disks with normal rotation speeds. They concluded that giant LSB disks should be rare and should be found only in voids. Bothun et al. (1993) examined the small scale environments around LSB disks of all sizes, using galaxies from the APM survey and from the POSS-II survey of Schombert & Bothun (1988) and Schombert et al. (1992). They searched the redshift catalog maintained by the Center for Astrophysics (hereafter referred to as “ZCAT”) for neighbors to the LSB galaxies and for neighbors to HSB galaxies in several carefully defined comparison samples. They found that LSB disks on average have significantly fewer near neighbors than HSB disks, and that the average distance to the nearest neighbor of an LSB galaxy was significantly greater than the average nearest-neighbor distance for an HSB galaxy. Zaritsky & Lorrimer (1993) found a similar deficit of close companions in a study of a more limited set of LSB galaxies and concluded that LSB galaxies remained LSB because they did not have opportunities for tidal interactions to trigger episodes of rapid star formation. With this background in mind, we examined the immediate environments around the giant LSB disks described here.

5.6.1 Qualitative Commentary

Two of the eight giant LSB disks from the APM survey have close companions. The galaxy 1034+0220 is accompanied by a small ($\approx 24''$) edge-on S0 or Sa located $0.8'$ to the southwest, or $45 h_{100}^{-1}$ kpc at the distance of 1034+0220. The companion, which we dub 1034+0220x, can be seen in Figure 5.1 to the SW of the primary galaxy. The two are close enough together that optical spectra and CCD images could be taken of both simultaneously. The spectra confirm that 1034+0220x is indeed a companion: the velocity separation between the two is only 198 km s^{-1} . Furthermore, the spectra reveal that the bulges of the two galaxies have quite similar

stellar populations. 1034+0220x has an apparent magnitude of $B = 17.8$. The major axis of 1034+0220 is aligned in the direction of the companion.

The galaxy 0052–0119 also has a close companion visible in the 4' square APM scan, which we call 0052–0119x. The companion 0052–0119x is 2.1' south-southeast from its large LSB neighbor, or $77 h_{100}^{-1}$ kpc at the distance of 0052–0119. Using ZCAT, we confirm that the two galaxies are likely neighbors, with a velocity separation of 337 km s^{-1} . The apparent magnitude of 0052–0119x is $B = 15.9$, which we measured from the APM scan because the angular separation from 0052–0119 is too great for both galaxies to be seen on the CCD frame. There is no apparent alignment of 0052–0119 toward 0052–0119x, the major axis of the parent being oriented 75° away from the companion. Nevertheless, there are several small, bright, blue regions around the outer edge of 0052–0119, predominantly on the side facing the companion. These bright spots account for the brightening of the outermost isophote, visible in Figure 5.2. These objects may be small regions of star formation triggered by the interaction with 0052–0119x. Tidal effects in both 1034+0220 and 0052–0119 are either subtle or absent. Neither galaxy shows any evidence of a bar, of a tidal cutoff in its surface brightness profile, or of widespread star formation. Based on the results of Bothun et al. (1993), about one-quarter of LSB galaxies should have companions within $0.5 h_{100}^{-1}$ Mpc, in accord with our detection of close companions in two out of eight cases.

Recent evidence in the literature reveals large scale structure in the vicinity of 1226+0105. Morris et al. (1993) conducted a redshift survey in the immediate area around 3C273 to see whether associations could be established between galaxies and Lyman α absorption features in the quasar spectrum. One result was the discovery of a large concentration or “wall” of galaxies at a mean redshift of $z \approx 0.078$ (or

$cz \approx 23400 \text{ km s}^{-1}$) which covers the complete width and height of their search box. This wall is the second richest concentration of galaxies in their search volume, after the Virgo cluster. The southern boundary of their search box lies almost $30'$ north of 1226+0105, which corresponds to a projected distance of $1.8 h_{100}^{-1} \text{ Mpc}$ at the distance of 1226+0105. One galaxy from their survey lies within a projected separation of $5 h_{100}^{-1} \text{ Mpc}$ and within a radial velocity difference of $\pm 500 \text{ km s}^{-1}$ of 1226+0105, and 24 galaxies lie within a projected separation of $10 h_{100}^{-1} \text{ Mpc}$ and within a radial velocity difference of $\pm 1000 \text{ km s}^{-1}$. In addition, the most recent version of ZCAT contains four galaxies within $5 h_{100}^{-1} \text{ Mpc}$ and $\pm 500 \text{ km s}^{-1}$, two of which are *south* of 1226+0105. Although existing redshift catalogs do not contain any close companions to 1226+0105, it seems likely that it lies in or near a significant large-scale structure.

There is evidence in the literature suggesting that Malin 1 may also lie in the vicinity of some large structure. Huchra & Brodie (1987) conducted a spectroscopic survey in the area around M87 to study that galaxy's globular clusters. They also identified a number of background galaxies with $v_{\text{hel}} \sim 25000 \text{ km s}^{-1}$. Malin 1 lies $\sim 2^\circ$ North and East of their search area, but four of their background galaxies are within 1000 km s^{-1} and $10 h_{100}^{-1} \text{ Mpc}$ projected separation of Malin 1. It is possible that this grouping of background galaxies extends well past the edge of their search area and reaches the local region around Malin 1, and the truly bold might wish to speculate on whether these galaxies form a northern extension of the "wall" at $z \approx 0.078$ identified by Morris et al. (1993). The most which can be safely said is that a few galaxies are found in the extended neighborhood of Malin 1, and that further investigation of the area around Malin 1 is called for.

5.6.2 Quantitative Measures of Isolation

Following the approach of Bothun et al. (1993), we searched through ZCAT for all galaxies lying within projected separations of $2.5 h_{100}^{-1}$ Mpc and having radial velocities within $\pm 500 \text{ km s}^{-1}$ of each of the eight giant LSB disks described here. The use of separate search criteria for projected separation and radial velocity results in a search volume in the shape of a truncated cone $10 h_{100}^{-1}$ Mpc long and $5 h_{100}^{-1}$ Mpc in diameter at the center, with a slightly smaller diameter at the near end and a slightly larger diameter at the far end. We chose the larger search limits in radial velocity for three reasons: to avoid excluding possible members of groups due to the group velocity dispersion, to accomodate the larger uncertainties associated with radial velocities (as opposed to positions), and for consistency with the analysis of Bothun et al. (1993). To provide a larger sample, we performed similar searches around Malin 1 and the galaxies from McGaugh & Bothun (1994) and Kent (1985) which have “diffuseness” indices > 27.0 (*i.e.*, all galaxies lying below and to the right of the dotted line in Figure 5.3). To allow a direct comparison with Bothun et al. (1993), we used the 1991 October edition of ZCAT, even though it contains only 70% as many galaxies as the more recent version used above. Bothun et al. (1993) described possible biases against finding companions to the LSB galaxies in ZCAT resulting from the incompletenesses in sky coverage and redshift depth of the catalog. Incompletenesses of both kinds result from the fact that many of the galaxies in ZCAT with $v_{\text{hel}} > 10000 \text{ km s}^{-1}$ are found through deep but very narrow pencil-beam surveys. Bothun et al. (1993) dealt with the redshift-depth bias by limiting their analysis to LSB galaxies with $v_{\text{hel}} \leq 12000 \text{ km s}^{-1}$, where ZCAT is relatively complete. They dealt with the sky-coverage bias by carefully defining their HSB comparison samples and reporting the results separately for the two LSB

samples, since ZCAT's sky coverage in the region of the APM survey is much thinner than in the region of the POSS-II LSB survey. Unfortunately, many of the giant LSB disks whose environments we examine here have $v_{\text{hel}} > 12000 \text{ km s}^{-1}$, and eight of them are from the equatorial APM survey.

We have derived averages for the accumulated number of neighbors within each radius of projected separation, but only for the giant LSB disks with $v_{\text{hel}} \leq 12000 \text{ km s}^{-1}$. This restriction eliminates about half the giant LSB spirals from consideration, but it avoids the severe bias caused by the shallow velocity depth of ZCAT. Table 5.9 compares the averages for the giant LSB spirals to those derived for larger LSB samples by Bothun et al. (1993), and to their HSB comparison samples. The giant LSB spirals actually have *more* companions on average than do LSB galaxies generally. The averages for the giant LSBs more closely resemble those for the HSB comparison samples from Bothun et al. (1993). This pattern holds at all separations and in both velocity groupings, though the differences are at best marginally significant ($\lesssim 2\sigma$). The small size of the sample of giant LSB spirals prevents any strong conclusions about the richness of the neighborhoods inhabited by these galaxies. It is clear, though, that the giant LSBs do not have fewer companions than do normal-sized and dwarf LSB galaxies.

We have also computed nearest-neighbor distances for those giant LSB disks that have neighbors within $2.5 h_{100}^{-1} \text{ Mpc}$ projected separation and 500 km s^{-1} radial velocity. The mean projected distance to the nearest neighbor is $0.43 \pm 0.11 h_{100}^{-1} \text{ Mpc}$, where again the error estimate is σ/\sqrt{N} . For the giant LSBs with neighbors found in the ZCAT search (*i.e.*, all of those with neighbors except 0052–0119 and 1034+0220), the average projected distance to the nearest neighbor is $0.52 \pm 0.11 h_{100}^{-1} \text{ Mpc}$. In contrast, the average projected nearest-neighbor distances found

Table 5.9: Average Number of Neighbors

Sample	Number	Bin Radius (h_{100}^{-1} Mpc)			
		0.5	1.0	1.5	2.0
Giant LSB					
$v < 7000$	8	0.88 ± 0.61	3.62 ± 1.22	6.38 ± 2.19	8.62 ± 2.87
$v < 12000$	9	0.78 ± 0.58	3.22 ± 1.15	5.67 ± 2.06	7.67 ± 2.71
POSS LSB ^a					
$v < 7000$	89	0.46 ± 0.09	1.36 ± 0.20	2.52 ± 0.31	4.11 ± 0.46
$v < 12000$	130	0.24 ± 0.05	0.94 ± 0.14	1.82 ± 0.21	3.03 ± 0.32
APM LSB ^a					
$v < 7000$	85	0.43 ± 0.08	1.41 ± 0.20	2.44 ± 0.28	3.84 ± 0.44
$v < 12000$	180	0.19 ± 0.04	0.78 ± 0.10	1.50 ± 0.16	2.23 ± 0.22
POSS HSB ^a					
$v < 7000$	530	1.13 ± 0.06	2.35 ± 0.12	3.93 ± 0.18	5.74 ± 0.24
$v < 12000$	845	1.02 ± 0.05	2.14 ± 0.10	3.59 ± 0.15	5.23 ± 0.21
APM HSB ^a					
$v < 7000$	91	0.66 ± 0.11	1.82 ± 0.20	3.35 ± 0.38	4.53 ± 0.45
$v < 12000$	131	0.47 ± 0.07	1.57 ± 0.16	2.50 ± 0.23	3.76 ± 0.35

Notes:

Average cumulative number of neighbors within each projected separation, and within $\pm 500 \text{ km s}^{-1}$. Errors are σ/\sqrt{N} . All velocities are heliocentric.

^aFrom Bothun et al. (1993)

by Bothun et al. (1993) were $0.99 \pm 0.06 h_{100}^{-1}$ Mpc for the POSS-II sample of LSB galaxies, and $0.91 \pm 0.05 h_{100}^{-1}$ Mpc for the APM sample of LSB galaxies. They also reported average projected nearest-neighbor distances for the HSB comparison samples of $0.57 \pm 0.02 h_{100}^{-1}$ Mpc and $0.68 \pm 0.05 h_{100}^{-1}$ Mpc for the comparison sets in the POSS LSB survey region and the APM LSB survey region, respectively. Among those galaxies that have neighbors within $2.5 h_{100}^{-1}$ Mpc of projected separation and 500 km s^{-1} of velocity, the projected separations between the giant LSB disks and their nearest neighbors seem on average to be smaller than the projected separations between normal or dwarf LSB galaxies and their nearest neighbors. The current small sample indicates that extreme isolation is not necessary for the formation or survival of these apparently low-density objects.

5.7 Conclusion

We have presented data on eight giant LSB spiral galaxies discovered through an objective, machine-based search for LSB objects. These eight giants extend the region occupied by spiral disks in the $\mu(0)$ – $\log(\alpha^{-1})$ parameter space, but they do not fill in the entire range between more normal spirals and the extreme cases like Malin 1 and GP 1444. Images with fainter limiting isophotes than Schmidt sky survey plates will be necessary to fill that gap. The integrated colors of the giant LSB spirals are redder than those of smaller LSB galaxies, and LSB galaxies follow a trend of redder color with increasing “diffuseness” that parallels a similar (but generally redder and offset towards lower “diffuseness”) trend among HSB galaxies. Active nuclei are common but not ubiquitous among these LSB giants, occurring in five out of the ten such galaxies described to date. The colors and spectroscopic

indices of the bulges of these LSB giants are indistinguishable from those of normal spirals, suggesting that the bulge populations and evolutionary histories are similar. The LSB giants typically have both high gas masses and high ratios of M_{HI}/L_B , though only Malin 1 is exceptional on either count. Finally, the LSB giants do not dwell in strict isolation; they are at least as likely to have neighbors as are smaller LSB galaxies, and the projected separations between the giants and their neighbors are usually smaller.

Chapter 6

CONCLUSIONS AND FUTURE WORK

6.1 Summary of Findings

In Chapter 2 we described the process of identifying LSB galaxies from the UKST survey plates using a combination of APM and visual searches. We measured the apparent magnitudes of the identified LSB galaxies with a typical uncertainty of $\sigma = 0.20$ mag in B , using pixel-to-pixel transformations calibrated by CCD observations of 106 of the LSB galaxies. Through simulations of the APM detection process we developed a selection function for the APM survey that describes the probability that an LSB galaxy will be included in our catalog as a function of the galaxy's central surface brightness and scale length, and we demonstrated that this objectively determined selection function substantially corrects for the incompleteness in the catalog. Finally, we compared the distribution of central surface brightnesses in our catalog to that first described by Freeman (1970), and we argued that the distribution in our catalog is inconsistent with a gaussian

distribution of $\langle \mu_B(0) \rangle = 21.65 \pm 0.4 \text{ mag arcsec}^{-2}$.

We presented luminosity functions for the galaxies of the APM LSB survey in Chapter 3. The luminosity function of the LSB galaxies has a shape generally similar to the functions derived from other field galaxy surveys, except for an excess of both low luminosity and high luminosity galaxies and a shift of M_* towards brighter values. LSB galaxies represent about one-fourth to one-third the integrated number density of galaxies found by other field galaxy studies, and they represent about one-third to one-half the integrated luminosity density found in those studies. The luminosity function for LSB irregulars has a much steeper faint-end slope than the overall luminosity function, and this difference seems to account for the excess of low-luminosity galaxies in the overall function. LSB galaxies may therefore contribute to a resolution of the discrepancy between no-evolution models and the excess counts of faint blue galaxies, but they are not numerous enough to explain away the discrepancy entirely. Finally, the density of high luminosity galaxies in the LSB sample is equal to or greater than the density of such galaxies seen in other field surveys. This relatively high density of luminous LSB galaxies could resolve the recently-noted difference between the numbers of local luminous galaxies and luminous galaxies detected at moderate redshift by their association with absorption features in QSO spectra.

In Chapter 4 we reported total magnitudes and H I profile widths for a sample of field LSB spiral galaxies, and compared these results to those of more visible galaxies using the familiar Tully-Fisher relation. The field LSB spirals generally follow the same Tully-Fisher relation as more visible galaxies in the Ursa Major cluster, albeit with a considerably higher scatter. This similarity suggests that the LSB spirals examined here generally have similar total M/L ratios to those of the

Ursa Major spirals, although the higher scatter suggests that the range of M/L ratios may be larger among LSB galaxies. Both the LSB and Ursa Major samples fall along substantially different Tully-Fisher relations from that defined by a sample of field galaxies in the direction of the Coma cluster, but there is no convincing explanation for the difference. Among the LSB galaxies, the weak trend of Tully-Fisher residuals to increase with increasing gas richness suggests that differences in evolutionary status among LSB galaxies may account for some part of the higher scatter. Differences in luminosity-profile width correlations among the B , R and I filters suggest that differences in stellar populations may also play a role. Further, a relation between M_{HI} and profile width that, while modest, is stronger than the B Tully-Fisher relation, suggests that atomic gas may be a larger fraction of total mass for LSB galaxies than for the Ursa Major comparison sample. Finally, the two giant Malin 1-class LSB spirals for which suitable data are available are both substantially overluminous for their rotation speeds, a fact that is difficult to reconcile with their low luminosity densities and presumed long cooling timescales.

We presented data in Chapter 5 on eight giant LSB spiral galaxies. These eight giants extend the region occupied by spiral disks in the $\mu(0)$ – $\log(\alpha^{-1})$ parameter space, but they do not fill in the entire range between more normal spirals and the extreme cases like Malin 1 and GP 1444. Images with fainter limiting isophotes than Schmidt sky survey plates will be necessary to fill that gap. The integrated colors of the giant LSB spirals are redder than those of smaller LSB galaxies, and LSB galaxies follow a trend of redder color with increasing “diffuseness” that parallels a similar (but generally redder and offset towards lower “diffuseness”) trend among HSB galaxies. Active nuclei are common but not ubiquitous among these LSB giants, occurring in five out of the ten such galaxies described to date. The colors and spectroscopic indices of the bulges of these LSB giants are indistinguishable from

those of normal spirals, suggesting that the stellar populations and evolutionary histories of these bulges are similar to those of normal spirals. The LSB giants typically have both high gas masses and high ratios of M_{HI}/L_B , though only Malin 1 is exceptional on either count. Finally, the LSB giants do not dwell in strict isolation; they are at least as likely to have neighbors as are smaller LSB galaxies, and the projected separations between the giants and their neighbors are usually smaller. The luminosity function developed in Chapter 3 revealed that luminous LSB galaxies outnumber luminous HSB galaxies, suggesting that the Malin 1-type giants are an important part of the total galaxy population that has been overlooked until the last few years.

6.2 Some Ideas for Further Investigations

There is an interesting connection between the distribution of surface brightnesses presented in Chapter 2 and the number density of LSB galaxies determined in Chapter 3. The number of galaxies per bin of surface brightness increases monotonically with decreasing surface brightness over the entire range for which the APM survey is complete or correctable for incompleteness ($22 \lesssim \mu_B(0) \lesssim 25 \text{ mag arcsec}^{-2}$), but the overall space density of LSB galaxies is only 25% to 33% that of higher surface brightness galaxies. These two findings raise the question of what the distribution of surface brightnesses would look like for a complete sample of galaxies that was objectively corrected for surface brightness selection biases. Do the galaxies sampled by surveys like those of Loveday et al. (1992) have higher numbers per bin of surface brightness than the LSB galaxies? Or do they have comparable numbers but cover a much broader range of surface brightnesses?

Galaxies with $r^{1/4}$ profiles have maximum apparent diameters at much brighter levels of $\mu(0)$ than do galaxies with exponential profiles (Chapter 2), so it might be that the higher space densities of HSB galaxies can be explained by a broad range of surface brightnesses. On the other hand, spirals tend to dominate the survey of Loveday et al. (1992), so perhaps the surface brightness distribution has a peak somewhere in the range defined by the peak in apparent diameter for exponential profiles. The resolution of this question requires the development of a complete and unbiased sample of consistently selected galaxies. We hoped that such a sample could be constructed by combining the LSB galaxies from the APM survey with selected galaxies from existing catalogs such as ZCAT, but the inconsistencies noted in Chapter 3 in the types of data available and the manner in which they were collected limit the usefulness of such combined lists.

The stellar evolutionary histories of LSB galaxies, especially of the diffuse disks of the Malin 1-type giants, remains unclear. McGaugh & Bothun (1994) presented a plausible general outline, but much remains to be filled in. Information about chemical abundances in the diffuse regions, away from the sites of active star formation, would be very helpful, but direct spectroscopy of areas with $\mu_B \gtrsim 25 \text{ mag arcsec}^{-2}$ is probably impossible, at least with 4-meter class telescopes. Here the probable connection between QSO absorption lines and giant LSB galaxies might be used to advantage. If the excess of luminous galaxies responsible for QSO absorption features can reliably be linked to the luminous LSB galaxies locally, then the abundance information obtained from the QSO absorption line studies could shed light on the conditions in the diffuse regions of the disk. Further work is needed, first, to estimate more concretely the integrated number and luminosity densities of the galaxies responsible for QSO absorption features. Then the information available from the QSO spectra on the H I column density distribution of the absorbers could

be compared to the column density distribution locally, including the LSB giants to tie the LSB giants more directly to the absorber population. If such a link could be established, the chemical abundances of the absorbers, especially those with lower H I column densities, could be taken as representative of conditions in the giant disks at some time in the past as indicated by the absorber redshift, thus providing a direct measure of evolution in the disks of galaxies like Malin 1.

It would be most helpful to know not just the luminosity function of local galaxies but the bivariate brightness distribution, *i.e.*, the space density of galaxies as a simultaneous function of total luminosity and surface brightness (see Davies 1993). Knowledge of this bivariate distribution would clarify the link between local populations and QSO absorbers and would provide valuable and needed constraints on theories of galaxy formation (*e.g.*, Lacey & Silk 1991, and Lacey et al. 1993). The APM survey discussed here could be used as the foundation for developing such a distribution, although full estimates of the distribution would require a galaxy sample that includes the HSB galaxies deliberately excluded from this survey. As noted in Chapter 3, present galaxy redshift catalogs are not sufficiently homogeneous or complete in the region of the sky covered by the APM LSB survey to be combined directly with this survey for statistical purposes. Work on the techniques to develop the bivariate distribution should proceed in parallel with the collection of a complete, homogeneous sample of galaxies that spans the full range of detectable surface brightnesses. The development of digitized versions of the major photographic surveys (*e.g.*, Weir et al. 1992) should help enormously with the creation of such a sample.

Rao & Briggs (1993) studied the H I mass function for local galaxies and compared this function to the statistics of damped Lyman α absorption systems

in QSO spectra. Like Steidel & Dickinson (1994), they concluded that the overall cross-section of absorbers was two to five times higher at $z \sim 2.5$, implying that galaxies were either more numerous or larger (or possibly both) in the past. The results of Chapter 3 suggest that LSB galaxies, particularly the giant Malin 1-type disks, may fill in at least part of the missing cross-section for H I absorption. Development of an H I mass function for the LSB galaxies in the present survey would be the first step towards addressing this question, and such work can be done with the data in hand. More complete H I data, particularly for the giant disks described in Chapter 5 would of course be very helpful, but collection of such data will probably have to await the completion of the new Green Bank radio telescope because many of these interesting objects are outside the declination range of the Arecibo observatory.

The spatial correlation of LSB galaxies is another topic of considerable interest for the study of galaxy formation and evolution. Theories of biased galaxy formation predict that low mass galaxies should be less strongly clustered than more massive galaxies (Dekel & Silk 1986). Theories of the formation of LSB galaxies predict that they should form only in relative isolation from other galaxies (Hoffman et al. 1992). The first efforts to address these questions have been made by Bothun et al. (1993) who found that LSB galaxies on average have fewer near neighbors (*i.e.*, projected separation $< 2.5 h_{100}^{-1}$ Mpc and velocity separation $< 500 \text{ km s}^{-1}$) and larger distances to their closest neighbor than do HSB galaxies, and by Mo et al. (1994) who found that LSB galaxies have a correlation scale length comparable to that of HSB galaxies but a lower correlation amplitude. The present data set offers the possibility of linking the clustering analysis to consistently measured magnitudes and surface brightnesses, so that the clustering properties could be estimated as a function of luminosity and surface brightness. These estimates, taken in combination

with the color information and optical spectroscopy available for some of the APM LSB galaxies, should reveal a great deal about the effects of environment on the formation and evolution of these interesting objects. But, as Rix (1991) noted, "One thesis at a time... ."

Appendix A

GALAXIES FROM THE LSB SURVEY: BASIC DATA

The following table gives the basic data on the galaxies detected by the APM survey for LSB galaxies. Galaxies are listed in order of increasing right ascension.

Column (1) gives the object name.

Columns (2) and (3) give the right ascension as hh:mm:ss.s and the declination as d:mm:ss. The coordinates are for the 1950.0 equinox. The coordinates are accurate to < 1 arcsec.

Column (4) gives the measured central surface brightness in B , in units of magnitudes arcsec $^{-2}$. This surface brightness is measured as the average luminosity density within a circular aperture of 2 arcsec radius centered on the intensity peak of the galaxy. Galaxies with entries in Column 7 have central surface brightnesses determined from CCD observations, and the typical uncertainties in these values are 0.07 mag arcsec $^{-2}$. All other galaxies have central surface brightnesses measured from the APM scans with typical uncertainties of about 0.3 mag arcsec $^{-2}$.

Column (5) gives the effective radius of the galaxy in arcsec, defined as the radius of a circular aperture enclosing half the total luminosity. Typical uncertainties are about 2 arcsec.

Column (6) gives the apparent B magnitude of the galaxy measured within the limiting isophote of the UKST-APM scans (≈ 26 mag arcsec $^{-2}$). Galaxies with entries in Column 7 have magnitudes determined from CCD observations, and the typical uncertainties in these values are 0.05 mag. All other galaxies have magnitudes measured from the APM scans with typical uncertainties of about 0.25 mag.

Column (7) gives the overall $B-V$ color of the galaxy, measured within the limiting isophote of the UKST-APM scans. The $B-V$ color is only available for those galaxies having followup CCD photometry.

Column (8) gives the heliocentric radial velocity of the galaxy in km s $^{-1}$. Velocities are only available for galaxies having followup 21 cm radio or optical spectroscopy. The velocities are derived from the 21 cm radio observations for those galaxies having entries in both Columns (8) and (9); typical uncertainties in these velocities are 20 km s $^{-1}$. All other velocities are derived from the low-resolution optical spectroscopy; typical uncertainties in these velocities are 200 km s $^{-1}$.

Column (9) gives the log of the H I mass of the galaxy, for those galaxies detected in the 21 cm radio observations. Typical uncertainties are about 0.05 dex.

Column (10) gives the de Vaucouleurs T -type. The standard system of de Vaucouleurs (1959) and de Vaucouleurs et al. (1976) is used, subject to the following comments: (a) $T = 21$ denotes interacting galaxies or other peculiar morphologies; (b) a few objects classed as spirals but for which no further

subclassification was possible were assigned $T = 4$.

Table A.1: Basic Data for APM Survey Galaxies

Name (1)	RA (2)	Dec (3)	$\mu_B(0)$ (4)	r_{eff} (5)	m_B (6)	$B-V$ (7)	v_{hel} (8)	Log M_H (9)	T (10)
0012+0227	0:12:19.1	+2:27:26	22.3	4.9	17.3	5
0012-0001	0:12:21.3	-0:01:31	20.8	5.7	15.5	...	11336	...	3
0012+0218	0:12:25.9	+2:18:10	24.5	7.2	18.7	0.41	17941	10.028	10
0013-0034	0:13:24.6	-0:34:53	20.3	18.4	14.5	0.61	11806	10.178	5
0014+0115	0:14:03.1	+1:15:23	20.9	8.2	15.5	0.52	12233	9.640	4
0014+0119	0:14:05.9	+1:19:56	19.8	10.3	14.7	0.67	13407	9.724	5
0014+0210	0:14:07.2	+2:10:59	23.2	9.2	16.9	0.55	4135	8.795	10
0016+0001	0:16:10.3	+0:01:49	23.3	4.4	18.5	5
0016-0052	0:16:57.1	-0:52:47	22.6	5.9	16.1	10
0017+0115	0:17:49.0	+1:15:03	23.6	4.3	18.8	4
0018-0011	0:18:04.4	-0:11:41	23.7	6.0	18.3	10
0019-0036	0:19:16.0	-0:36:07	24.0	7.2	18.0	5
0023+0034	0:23:00.5	+0:34:11	21.8	6.2	16.2	4
0023+0044	0:23:51.1	+0:44:35	22.3	13.2	15.9	0.50	5366	9.320	7
0024-0106	0:24:33.9	-1:06:56	21.7	7.7	16.0	...	17101	...	21
0025+0221	0:25:13.1	+2:21:47	23.4	11.8	17.0	0.38	4069	8.585	10
0025+0306b	0:25:43.8	+3:06:25	22.0	23.0	14.7	0.57	4033	9.470	5
0025+0306a	0:25:47.5	+3:06:43	21.0	10.8	15.0	...	3854	...	3
0026+0200	0:26:13.8	+2:00:47	23.7	6.1	18.3	10
0026-0052	0:26:21.7	-0:52:10	24.9	9.4	18.1	10
0027+0134	0:27:13.9	+1:34:44	21.9	9.4	15.7	...	3436	8.648	7
0028-0151	0:28:14.7	-1:51:48	24.9	10.9	18.0	-5
0029+0037	0:29:09.4	+0:37:30	22.5	8.8	16.7	5
0029+0226	0:29:11.1	+2:26:22	24.8	10.8	17.9	10
0031+0224	0:31:01.8	+2:24:19	21.5	20.1	14.6	...	7136	...	5
0048+0009	0:48:08.9	+0:09:38	21.3	6.2	15.8	3
0048+0052	0:48:23.4	+0:52:51	21.2	7.3	15.6	3
0048-0219	0:48:45.9	-2:19:10	24.1	7.2	18.3	8
0049+0105	0:49:27.7	+1:05:24	24.2	6.1	18.9	9
0049-0031	0:49:37.8	-0:31:06	24.4	5.3	18.7	6
0050+0006	0:50:23.3	+0:06:59	21.2	4.8	16.3	0.35	10321	9.786	3
0050+0005	0:50:24.0	+0:05:49	20.0	2.8	16.2	0.34	10283	9.827	4
0050+0230	0:50:54.4	+2:30:11	20.7	7.4	15.3	0.54	5002	9.161	4
0051-0121	0:51:09.2	-1:21:21	21.6	7.2	15.9	5
0051-0227	0:51:48.5	-2:27:59	22.2	12.2	16.4	9

Table A.1: Continued

Name (1)	RA (2)	Dec (3)	$\mu_B(0)$ (4)	r_{eff} (5)	m_B (6)	$B-V$ (7)	v_{hel} (8)	Log M_H (9)	T (10)
0052+0029	0:52:05.9	+0:29:03	24.1	4.9	19.0	6
0052+0243	0:52:18.7	+2:43:48	21.4	8.8	15.9	0.26	27499	...	5
0052-0119	0:52:35.5	-1:19:01	19.9	11.9	14.9	0.89	13198	...	7
0056+0245	0:56:04.3	+2:45:33	21.9	8.9	16.0	...	5121	8.992	7
0056+0019	0:56:15.0	+0:19:04	21.3	12.2	14.3	...	5437	9.617	3
0056+0044	0:56:21.5	+0:44:06	22.1	6.1	16.7	10
0056+0020	0:56:21.9	+0:20:16	24.6	7.2	18.7	10
0059+0248	0:59:11.4	+2:48:47	21.7	11.8	15.6	-0.68	4379	8.917	5
0101+0124	1:01:02.7	+1:24:18	24.6	4.5	19.4	10
0103-0001	1:03:16.5	-0:01:31	21.7	4.6	16.6	3
0103+0030	1:03:33.2	+0:30:30	22.9	14.5	16.4	7
0104-0001	1:04:13.1	-0:01:23	24.3	5.2	18.9	5
0104+0140	1:04:19.7	+1:40:41	20.3	5.1	15.4	0.57	4708	8.744	3
0104-0101	1:04:23.2	-1:01:23	24.3	6.2	18.5	4
0104+0044	1:04:49.7	+0:44:06	24.1	8.9	17.3	10
0105+0047	1:05:12.4	+0:47:48	21.1	12.7	14.9	0.35	632	7.482	5
0105-0214	1:05:34.9	-2:14:34	23.8	14.4	17.2	10
0107-0231	1:07:08.6	-2:31:59	21.8	19.6	14.8	6
0108-0004	1:08:17.1	-0:04:04	21.7	9.5	15.5	...	5297	9.344	5
0108+0242	1:08:46.5	+2:42:28	22.3	8.9	16.4	5
0108+0243	1:08:50.4	+2:43:01	22.8	7.9	17.1	5
0109-0055	1:09:13.2	-0:55:48	21.7	8.1	15.2	2
0109-0053	1:09:17.9	-0:53:45	21.7	6.2	15.9	3
0110+0023	1:10:10.9	+0:23:39	22.0	5.6	16.7	5
0110+0046	1:10:16.6	+0:46:55	24.7	42.6	16.1	10
0110-0251	1:10:34.2	-2:51:54	23.6	5.4	18.5	4
0110+0034	1:10:36.1	+0:34:18	23.0	8.2	17.6	5
0111+0036	1:11:05.4	+0:36:36	23.4	18.2	16.1	10
0111-0019	1:11:58.0	-0:19:54	23.2	7.2	17.7	-5
0112+0055	1:12:03.3	+0:55:01	21.7	14.2	14.9	7
0112-0045	1:12:15.2	-0:45:36	21.5	8.9	14.9	21
0114+0056	1:14:01.8	+0:56:20	23.0	10.3	16.9	0.39	5093	8.930	7
0114+0204	1:14:14.3	+2:04:51	23.7	10.4	17.2	10
0115-0125	1:15:29.6	-1:25:46	23.8	8.4	18.1	8
0116-0158	1:16:56.5	-1:58:02	23.5	15.7	16.5	5

Table A.1: Continued

Name (1)	RA (2)	Dec (3)	$\mu_B(0)$ (4)	r_{eff} (5)	m_B (6)	$B-V$ (7)	v_{hel} (8)	Log M_H (9)	T (10)
0117+0231	1:17:20.7	+2:31:25	23.9	6.6	18.5	6
0117+0027	1:17:24.7	+0:27:37	23.2	8.4	17.4	0.48	4394	8.622	7
0117-0013	1:17:49.7	-0:13:54	24.8	6.8	19.2	4
0118-0004	1:18:39.4	-0:04:26	24.3	9.9	18.3	8
0118-0010	1:18:47.6	-0:10:17	21.2	10.4	14.9	0.41	3738	...	9
0118+0026	1:18:53.6	+0:26:56	24.0	4.5	19.2	6
0121+0148	1:21:21.6	+1:48:55	21.9	14.8	16.1	21
0121+0128	1:21:59.4	+1:28:15	21.7	40.2	13.0	...	5028	9.640	5
0122+0134	1:22:47.6	+1:34:52	23.9	4.8	18.9	4
0122+0129	1:22:56.8	+1:29:57	22.0	30.0	13.4	-2
0123+0055	1:23:05.6	+0:55:06	22.0	6.5	16.1	3
0123-0029	1:23:20.1	-0:29:43	24.6	33.4	17.1	-5
0123+0017	1:23:55.4	+0:17:21	23.6	9.3	17.5	...	5446	8.819	4
0124-0109	1:24:37.9	-1:09:26	24.4	4.4	19.4	6
0125-0006	1:25:09.2	-0:06:08	26.1	21.0	18.0	-5
0126-0157	1:26:21.0	-1:57:28	24.0	5.1	18.7	3
0126-0109	1:26:35.3	-1:09:17	24.8	7.5	19.0	4
0127+0234	1:27:54.1	+2:34:28	23.5	10.8	17.0	0.30	2111	8.066	4
0128+0036	1:28:01.7	+0:36:02	23.9	4.7	18.9	3
0128-0229	1:28:10.4	-2:29:20	23.9	8.1	18.0	9
0129-0029	1:29:17.0	-0:29:20	24.9	32.0	17.4	10
0130-0235	1:30:51.0	-2:35:59	26.3	57.2	16.1	10
0132-0024	1:32:06.0	-0:24:00	27.7	43.9	17.0	10
0132+0146	1:32:56.9	+1:46:36	22.6	16.1	16.1	0.40	2606	8.797	5
0134-0036	1:34:55.2	-0:36:21	24.2	5.1	19.2	10
0137+0220	1:37:09.3	+2:20:23	21.8	4.5	16.7	3
0139+0240	1:39:58.9	+2:40:41	24.4	26.0	16.9	...	1765	8.600	10
0141+0205	1:41:22.9	+2:05:56	21.6	10.0	15.0	3
0141-0039	1:41:45.2	-0:39:43	25.2	5.0	19.6	10
0142-0033	1:42:29.8	-0:33:06	22.4	9.4	16.4	0.43	5407	9.366	10
0143+0200	1:43:59.7	+2:00:27	24.2	4.9	19.0	9
0146+0244	1:46:36.7	+2:44:44	21.6	5.7	16.6	4
0147+0203	1:47:35.8	+2:03:47	22.9	17.7	15.5	...	1698	8.344	10
0150-0114	1:50:44.4	-1:14:03	24.1	3.9	19.3	4
0209-0202	2:09:45.1	-2:02:05	23.5	5.5	18.4	2

Table A.1: Continued

Name (1)	RA (2)	Dec (3)	$\mu_B(0)$ (4)	r_{eff} (5)	m_B (6)	$B-V$ (7)	v_{hel} (8)	Log M_H (9)	T (10)
0210-0042	2:10:22.1	-0:42:03	23.4	6.5	18.2	4
0211-0053	2:11:17.3	-0:53:37	23.6	5.0	18.5	2
0212-0031	2:12:58.4	-0:31:22	23.0	7.9	17.2	5
0213+0121	2:13:23.1	+1:21:48	23.8	7.4	18.3	5
0213-0056	2:13:25.3	-0:56:43	22.0	8.6	15.9	7
0217+0031	2:17:26.8	+0:31:40	25.0	27.6	17.2	10
0221+0001	2:21:27.5	+0:01:33	21.6	9.7	16.5	0.70	37263	...	5
0221+0034	2:21:49.8	+0:34:41	24.7	18.9	17.3	...	8996	9.248	7
0222-0050	2:22:01.4	-0:50:29	23.7	4.8	18.9	3
0222-0201	2:22:34.0	-2:01:59	25.2	51.9	16.7	10
0223-0033	2:23:33.3	-0:33:24	22.1	18.3	14.5	...	6433	9.826	5
0223+0125	2:23:37.2	+1:25:03	23.9	6.0	18.5	6
0223-0052	2:23:38.6	-0:52:32	23.8	3.9	19.2	5
0224+0238	2:24:11.4	+2:38:27	25.8	18.8	17.6	10
0224+0233	2:24:59.2	+2:33:46	26.4	18.6	18.1	10
0225-0134	2:25:39.8	-1:34:09	22.6	20.0	14.8	7
0225-0049	2:25:45.6	-0:49:50	25.0	13.2	18.0	...	1464	7.709	10
0227+0009	2:27:00.0	+0:09:03	23.7	9.9	18.2	5
0227+0040	2:27:01.1	+0:40:55	24.8	13.7	18.1	...	8503	9.535	10
0227-0242	2:27:25.3	-2:42:11	23.4	4.4	18.6	3
0227+0042	2:27:42.5	+0:42:56	23.1	20.6	15.4	...	1517	7.703	10
0229-0243	2:29:02.5	-2:43:00	24.0	9.1	17.6	8
0229+0235	2:29:05.2	+2:35:21	20.3	5.1	15.2	0.30	8235	...	2
0229+0234	2:29:05.9	+2:34:40	20.7	3.7	16.3	0.30	8157	...	10
0229-0158	2:29:06.9	-1:58:54	23.5	4.2	18.8	5
0229+0004	2:29:09.4	+0:04:22	21.8	12.1	15.5	0.45	6333	9.450	7
0229+0005	2:29:13.3	+0:05:29	23.5	4.3	18.7	6
0229-0115	2:29:17.6	-1:15:50	23.4	7.0	17.7	9
0229+0255	2:29:37.0	+2:55:23	24.0	7.0	18.9	-5
0230+0023	2:30:05.1	+0:23:51	20.2	6.8	14.7	0.54	6307	...	2
0230+0221	2:30:08.6	+2:21:29	23.4	3.6	18.8	3
0232+0102	2:32:24.1	+1:02:27	20.8	4.7	15.7	...	6806	...	2
0233+0012	2:33:26.9	+0:12:10	21.8	23.4	14.4	0.37	2615	8.893	5
0234-0206	2:34:54.4	-2:06:00	23.8	4.0	19.0	10
0235-0152	2:35:19.6	-1:52:53	22.8	24.6	16.4	10

Table A.1: Continued

Name (1)	RA (2)	Dec (3)	$\mu_B(0)$ (4)	r_{eff} (5)	m_B (6)	$B-V$ (7)	v_{hel} (8)	Log M_H (9)	T (10)
0236+0018	2:36:14.6	+0:18:18	23.6	30.9	16.4	...	1467	8.430	21
0237-0159	2:37:38.7	-1:59:18	20.9	17.4	15.3	0.67	12701	...	5
0237+0212	2:37:42.1	+2:12:45	20.5	4.9	15.6	0.51	6464	9.150	9
0237-0256	2:37:52.0	-2:56:30	21.3	24.9	14.7	...	7309	...	21
0238+0001	2:38:22.7	+0:01:55	22.6	6.3	17.3	5
0239+0049	2:39:52.8	+0:49:29	21.7	5.0	16.7	5
0240-0028	2:40:36.9	-0:28:27	22.7	10.5	16.5	0.57	630	...	-5
0240-0121	2:40:59.8	-1:21:16	24.6	22.4	17.2	10
0241-0049	2:41:19.7	-0:49:45	22.3	6.8	16.6	5
0243+0001	2:43:10.8	+0:01:21	23.8	8.2	18.0	5
0243+0301	2:43:13.1	+3:01:13	21.0	9.4	14.9	0.44	6811	9.365	4
0243-0027	2:43:14.1	-0:27:02	22.6	8.4	17.0	5
0243-0034	2:43:57.6	-0:34:31	22.3	4.9	17.1	4
0244-0028	2:44:04.1	-0:28:44	24.3	8.3	18.9	10
0244-0039	2:44:19.5	-0:39:46	22.5	3.0	18.1	9
0244+0117	2:44:40.6	+1:17:57	21.4	5.5	16.3	...	8323	...	9
0244-0127	2:44:59.2	-1:27:16	22.6	9.3	17.0	10
0245+0257	2:45:11.3	+2:57:24	20.2	5.4	15.0	...	6786	9.208	3
0246+0046	2:46:17.4	+0:46:55	20.8	10.5	14.5	...	7748	...	3
0246-0033	2:46:19.3	-0:33:27	23.2	14.1	16.6	...	2679	8.719	10
0246+0145	2:46:33.0	+1:45:29	23.5	29.6	16.8	...	2934	8.553	10
0248-0048	2:48:10.6	-0:48:29	23.9	13.3	17.2	21
0249+0146	2:49:45.0	+1:46:17	24.5	21.2	16.5	...	4293	8.867	10
0308+0107	3:08:44.0	+1:07:40	20.2	13.2	15.1	0.73	9599	...	21
0309-0309	3:09:24.4	-3:09:15	20.6	12.3	15.0	0.78	8128	...	4
0310-0112	3:10:20.3	-1:12:39	23.8	6.9	18.4	8
0311+0241	3:11:16.3	+2:41:39	20.4	6.1	15.3	0.48	9533	9.570	21
0311-0157	3:11:19.7	-1:57:38	21.6	6.3	16.1	...	8773	...	9
0311-0021	3:11:22.2	-0:21:40	23.6	8.4	17.6	6
0311-0129	3:11:46.9	-1:29:58	21.0	8.1	15.3	0.28	8079	...	9
0311-0259	3:11:52.1	-2:59:09	20.6	17.3	13.7	...	1731	...	10
0312+0219	3:12:56.1	+2:19:45	20.5	4.7	15.8	0.61	9934	...	10
0313+0148	3:13:23.0	+1:48:45	23.7	5.5	18.4	7
0313+0205	3:13:47.8	+2:05:07	23.8	4.9	18.9	4
0314+0005	3:14:32.2	+0:05:54	23.4	10.2	17.1	...	8119	9.305	10

Table A.1: Continued

Name (1)	RA (2)	Dec (3)	$\mu_B(0)$ (4)	r_{eff} (5)	m_B (6)	$B-V$ (7)	v_{hel} (8)	Log M_H (9)	T (10)
0314+0108	3:14:47.1	+1:08:51	23.2	7.4	17.8	-5
0316+0102	3:16:24.5	+1:02:57	23.6	5.5	18.6	5
0316-0100	3:16:46.7	-1:00:54	24.7	5.3	19.0	10
0317+0003	3:17:10.7	+0:03:33	23.8	4.8	18.7	5
0317-0246	3:17:20.9	-2:46:22	21.0	11.4	15.1	...	8616	...	3
0317-0121	3:17:48.4	-1:21:00	24.1	6.3	18.4	5
0318-0140	3:18:00.6	-1:40:01	22.4	8.9	16.7	4
0318-0101	3:18:12.9	-1:01:50	22.9	11.0	16.3	9
0318+0133	3:18:22.5	+1:33:43	23.5	5.0	18.4	4
0319+0015	3:19:14.2	+0:15:00	24.4	8.3	18.4	...	6548	9.240	10
0319+0033	3:19:29.6	+0:33:32	23.5	4.5	18.6	3
0320+0111	3:20:25.1	+1:11:17	19.1	8.4	14.6	0.69	10057	...	9
0321+0221	3:21:29.6	+2:21:52	20.9	4.6	16.2	0.39	9060	...	3
0323+0230	3:23:59.2	+2:30:21	23.4	6.5	18.1	7
0325+0135	3:25:37.2	+1:35:47	23.7	4.9	18.8	5
0326-0113	3:26:38.0	-1:13:02	23.5	5.5	18.3	4
0327-0128	3:27:31.8	-1:28:05	21.4	7.3	16.1	...	10364	...	5
0329-0216	3:29:11.2	-2:16:24	22.5	9.0	16.4	10
0330+0213	3:30:44.9	+2:13:00	23.2	4.2	18.6	4
0331-0032	3:31:16.2	-0:32:56	23.2	4.1	18.6	4
0331-0259	3:31:34.3	-2:59:09	20.8	5.7	16.3	5
0332-0209	3:32:10.7	-2:09:51	23.1	11.9	16.6	9
0332+0058	3:32:33.5	+0:58:36	23.2	8.3	17.3	5
0332-0102	3:32:34.2	-1:02:35	22.9	6.7	17.3	5
0334+0010	3:34:08.5	+0:10:22	22.5	7.9	16.4	5
0336+0212	3:36:19.7	+2:12:55	21.7	12.2	15.9	0.52	3144	8.617	10
0336-0018	3:36:28.8	-0:18:30	23.6	6.4	18.3	7
0337-0040	3:37:01.0	-0:40:23	22.3	14.5	15.8	0.61	7720	9.708	5
0337-0216	3:37:21.6	-2:16:27	20.2	9.0	14.4	...	10426	...	21
0338-0128	3:38:02.0	-1:28:13	21.3	8.1	15.8	0.57	7522	...	9
0338-0127	3:38:38.1	-1:27:41	19.6	13.3	14.0	0.92	7507	...	21
0339-0209	3:39:12.7	-2:09:42	22.4	30.6	15.3	...	8459	...	5
0339-0216	3:39:27.3	-2:16:51	23.7	5.1	18.4	6
0340-0201	3:40:19.2	-2:01:34	22.8	11.2	16.1	0.42	2811	...	4
0340-0200	3:40:39.0	-2:00:38	21.3	10.5	15.8	...	7463	...	5

Table A.1: Continued

Name (1)	RA (2)	Dec (3)	$\mu_B(0)$ (4)	r_{eff} (5)	m_B (6)	$B-V$ (7)	v_{hel} (8)	Log M_H (9)	T (10)
0341+0220	3:41:07.7	+2:20:44	23.5	5.7	17.9	9
0341+0133	3:41:37.2	+1:33:01	19.6	6.3	15.2	0.88	10586	...	21
0342+0240	3:42:04.3	+2:40:42	20.3	11.8	14.8	0.79	8928	...	5
0342+0107	3:42:38.9	+1:07:09	22.3	7.6	16.5	5
0342+0214	3:42:56.6	+2:14:24	23.0	3.8	18.5	4
0343+0200	3:43:09.9	+2:00:32	22.9	8.4	16.6	...	4278	9.096	9
0343-0217	3:43:20.1	-2:17:07	23.6	4.7	18.4	9
0344+0133	3:44:45.6	+1:33:33	20.6	5.6	15.9	0.73	10669	...	3
0345+0118b	3:45:07.8	+1:18:54	23.6	7.0	18.3	-5
0345+0118a	3:45:23.1	+1:18:43	23.3	7.3	17.6	-5
0346+0101	3:46:24.9	+1:01:11	22.2	12.6	15.6	...	4137	9.376	9
0346-0016	3:46:26.1	-0:16:06	23.6	7.4	17.8	-5
0346+0100	3:46:33.3	+1:00:39	20.2	10.6	14.4	0.33	4191	9.324	9
0349-0139	3:49:42.0	-1:39:24	20.5	15.6	14.2	0.66	4976	...	3
0349+0225	3:49:58.1	+2:25:32	22.9	4.0	18.0	8
0350+0041	3:50:51.8	+0:41:40	21.9	9.7	16.1	...	11362	9.602	5
0351-0017	3:51:14.2	-0:17:05	22.3	4.3	17.3	5
0351-0019	3:51:18.0	-0:19:19	21.2	6.8	15.3	10
0352+0152	3:52:06.2	+1:52:06	23.0	10.8	16.8	...	11255	9.969	5
0353+0154	3:53:02.0	+1:54:02	23.1	10.1	16.9	0.58	11076	...	6
0353-0125	3:53:05.3	-1:25:05	24.2	5.0	19.1	6
0353+0224	3:53:11.7	+2:24:00	27.8	30.2	17.7	10
0353-0004	3:53:11.8	-0:04:15	24.2	5.2	19.1	5
0354-0043	3:54:05.9	-0:43:25	24.7	6.0	19.2	-5
0354+0142	3:54:41.2	+1:42:26	23.6	7.1	18.1	9
0355-0031	3:55:26.2	-0:31:08	24.1	7.4	18.3	5
0357-0059	3:57:02.8	-0:59:46	24.5	4.5	19.7	5
0357-0229	3:57:34.0	-2:29:38	24.0	5.4	18.9	8
0357+0036	3:57:36.2	+0:36:13	23.6	22.9	16.6	...	3544	9.338	7
0358-0051	3:58:29.6	-0:51:25	23.1	18.5	16.0	0.79	4219	9.288	6
0359+0228	3:59:00.8	+2:28:01	24.2	8.3	18.4	9
0359-0203	3:59:59.0	-2:03:20	23.5	12.9	17.2	...	4611	...	9
0400+0149	4:00:12.6	+1:49:36	22.1	28.8	15.1	...	3817	9.489	6
0400-0212	4:00:41.7	-2:12:03	24.6	12.6	18.3	9
0401+0148	4:01:06.9	+1:48:03	23.5	5.3	18.1	4

Table A.1: Continued

Name (1)	RA (2)	Dec (3)	$\mu_B(0)$ (4)	r_{eff} (5)	m_B (6)	$B-V$ (7)	v_{hel} (8)	Log M_H (9)	T (10)
0401+0213	4:01:10.4	+2:13:38	24.8	13.7	18.3	10
0401+0146	4:01:21.5	+1:46:49	23.9	7.2	18.2	5
0402-0205	4:02:01.5	-2:05:04	25.3	16.3	18.4	6
0402-0157	4:02:20.8	-1:57:28	23.3	9.1	18.3	10
0402+0141	4:02:39.6	+1:41:03	25.4	9.7	18.5	10
0405+0214	4:05:57.0	+2:14:49	23.9	4.6	19.2	5
0405+0259	4:05:58.2	+2:59:30	23.2	13.5	16.9	...	7314	9.861	9
0406+0021	4:06:39.9	+0:21:34	24.0	19.1	17.8	10
0407+0209	4:07:05.5	+2:09:12	23.4	8.6	17.8	7
0411+0244	4:11:36.9	+2:44:13	18.7	2.0	15.1	...	11999	...	4
0411+0236	4:11:46.8	+2:36:21	20.9	12.9	15.2	...	3336	9.113	5
0411+0243	4:11:51.6	+2:43:10	24.0	15.6	17.2	...	3445	8.715	9
0910-0157	9:10:59.6	-1:57:34	22.4	6.1	17.3	...	8078	...	5
0911-0002	9:11:00.3	-0:02:44	20.7	3.2	16.7	...	20375	...	4
0911-0139	9:11:27.9	-1:39:10	22.7	12.2	17.0	...	6366	...	5
0913-0108	9:13:06.8	-1:08:18	20.6	6.9	15.7	0.78	16269	...	3
0913+0054	9:13:39.3	+0:54:34	20.4	8.2	15.5	0.61	11401	9.679	9
0914+0241	9:14:45.2	+2:41:26	24.2	10.4	18.1	...	19339	...	10
0915+0115	9:15:10.6	+1:15:56	21.8	6.5	16.3	...	8216	9.181	5
0917-0022	9:17:21.8	-0:22:46	22.5	8.4	16.4	...	8690	9.426	9
0918-0028	9:18:03.9	-0:28:01	21.0	8.1	15.0	0.65	3492	8.633	3
0918-0104	9:18:30.7	-1:04:21	23.4	4.6	18.6	6
0918+0147	9:18:58.5	+1:47:52	23.5	8.9	17.7	0.54	4978	8.876	10
0920-0042	9:20:16.4	-0:42:18	24.0	5.1	18.9	8
0920-0116	9:20:56.6	-1:16:19	21.8	7.1	16.6	0.47	18460	...	5
0921+0258	9:21:10.5	+2:58:08	22.3	14.1	16.4	...	5064	9.150	9
0921+0217	9:21:31.2	+2:17:53	20.9	4.1	16.4	...	7224	9.110	4
0922+0233	9:22:59.2	+2:33:30	24.0	5.4	18.8	9
0925-0009	9:25:26.2	-0:09:42	20.8	6.8	16.2	0.73	20452	...	5
0927+0225	9:27:05.7	+2:25:29	20.3	9.7	15.8	1.05	7123	...	5
0929+0147	9:29:02.8	+1:47:29	20.6	13.3	15.7	...	17324	10.033	5
0929+0246	9:29:47.4	+2:46:10	23.2	23.2	16.7	...	5233	9.330	10
0931+0036	9:31:30.1	+0:36:24	23.2	11.7	17.3	...	7027	9.118	9
0949+0036	9:49:04.6	+0:36:16	23.5	12.0	17.4	...	1897	8.140	10
0951+0214	9:51:24.1	+2:14:30	25.0	15.3	18.1	10

Table A.1: Continued

Name (1)	RA (2)	Dec (3)	$\mu_B(0)$ (4)	τ_{eff} (5)	m_B (6)	$B-V$ (7)	v_{hel} (8)	Log M_H (9)	T (10)
0951+0146	9:51:29.7	+1:46:36	25.3	5.8	20.1	10
0954+0125	9:54:38.4	+1:25:33	25.3	6.1	19.8	10
0954+0209	9:54:45.5	+2:09:25	21.1	9.3	15.6	...	9592	9.592	5
0954-0226	9:54:47.5	-2:26:27	24.3	4.3	19.7	4
0955+0145	9:55:31.2	+1:45:09	23.7	4.4	19.0	4
0955+0155	9:55:54.5	+1:55:59	24.9	18.3	17.2	...	1815	8.541	10
0956+0235	9:56:11.6	+2:35:12	23.6	11.0	17.9	...	1729	8.100	10
0956-0034	9:56:55.3	-0:34:19	25.8	19.3	18.1	1
0956-0105	9:56:58.4	-1:05:13	22.8	8.0	17.3	0.40	13303	...	4
0957+0049	9:57:05.5	+0:49:36	22.1	8.6	16.6	0.68	19762	...	21
0957-0154	9:57:09.7	-1:54:34	21.1	7.7	15.6	...	11040	...	3
0957+0052	9:57:25.3	+0:52:41	21.5	5.6	16.6	0.39	9735	...	9
1000-0118	10:00:54.0	-1:18:11	20.5	7.4	15.5	0.47	13624	...	21
1002-0130	10:02:03.1	-1:30:09	21.0	7.0	15.5	0.56	13532	...	10
1002+0036	10:02:06.8	+0:36:46	20.4	6.5	15.8	0.72	13042	...	3
1003+0151	10:03:08.3	+1:51:31	24.5	4.2	19.9	6
1006-0120	10:06:10.9	-1:20:49	24.4	5.6	19.5	7
1007+0121	10:07:54.6	+1:21:42	21.6	8.1	15.9	...	29213	10.688	5
1008+0208	10:08:22.8	+2:08:39	24.0	6.7	18.2	7
1008+0128	10:08:30.8	+1:28:14	21.1	8.7	15.5	0.42	9915	9.872	21
1008+0041	10:08:43.8	+0:41:26	21.9	19.6	14.0	...	3646	9.242	3
1010-0159	10:10:02.8	-1:59:30	22.9	9.1	17.0	7
1010+0052	10:10:19.9	+0:52:18	24.3	3.8	19.8	3
1012-0108	10:12:17.1	-1:08:17	21.8	8.3	15.5	...	9279	...	3
1013+0256	10:13:15.3	+2:56:35	22.4	3.7	17.8	5
1013-0232	10:13:31.5	-2:32:55	24.5	6.0	18.6	9
1015+0148	10:15:27.8	+1:48:43	22.7	9.9	16.7	...	13660	9.840	9
1016+0229	10:16:18.9	+2:29:41	22.2	7.1	16.5	0.54	13715	9.442	21
1016-0257	10:16:40.6	-2:57:48	22.2	7.6	16.7	...	8427	...	5
1017+0145	10:17:36.9	+1:45:52	23.6	6.5	18.1	9
1017-0110	10:17:37.5	-1:10:08	23.7	3.9	19.1	5
1019+0126	10:19:52.9	+1:26:38	25.0	10.7	18.2	-5
1021+0143	10:21:35.1	+1:43:15	24.0	5.0	19.0	5
1022+0234	10:22:58.4	+2:34:19	21.7	6.3	16.1	...	18728	...	3
1023-0224	10:23:00.5	-2:24:20	23.7	4.4	18.9	7

Table A.1: Continued

Name (1)	RA (2)	Dec (3)	$\mu_B(0)$ (4)	r_{eff} (5)	m_B (6)	$B-V$ (7)	v_{hel} (8)	Log M_H (9)	T (10)
1023-0159	10:23:05.5	-1:59:23	23.7	4.5	18.9	4
1023+0215	10:23:20.9	+2:15:32	21.6	7.7	15.8	...	19902	...	3
1024+0025	10:24:25.7	+0:25:46	23.8	4.5	19.0	6
1025-0040	10:25:08.0	-0:40:49	23.3	6.8	17.9	...	11623	...	-5
1027-0138	10:27:49.7	-1:38:39	20.4	4.1	16.0	...	12190	...	5
1028-0137	10:28:07.4	-1:37:42	22.1	8.3	16.2	...	8866	...	5
1029-0040	10:29:01.7	-0:40:59	22.3	7.9	16.5	5
1029-0114	10:29:39.7	-1:14:09	20.4	9.7	14.9	0.79	11305	...	21
1029+0248	10:29:51.8	+2:48:45	21.9	11.6	16.2	...	6593	9.453	5
1030+0252	10:30:46.0	+2:52:27	20.9	7.6	14.8	...	8825	9.651	3
1030+0141	10:30:47.3	+1:41:17	22.9	10.5	16.5	-5
1031-0024	10:31:06.1	-0:24:07	23.0	7.7	17.4	5
1032-0121	10:32:50.0	-1:21:37	23.2	9.2	17.0	10
1034+0234	10:34:49.0	+2:34:18	20.2	6.5	15.4	0.84	11849	...	21
1034+0220	10:34:52.9	+2:20:57	21.0	8.8	16.1	0.63	21335	...	5
1035+0238	10:35:17.7	+2:38:57	22.7	6.8	17.3	...	5637	8.886	10
1035-0222	10:35:35.8	-2:22:49	20.5	9.1	15.1	1.03	6250	...	21
1035+0014	10:35:51.6	+0:14:31	22.4	11.3	16.6	...	5656	9.344	5
1036+0148	10:36:13.7	+1:48:01	23.9	6.0	18.7	5
1036+0207	10:36:42.4	+2:07:15	23.1	9.2	17.1	...	8407	9.368	10
1036+0158	10:36:50.8	+1:58:45	21.9	11.9	15.0	...	710	7.615	10
1040-0236	10:40:32.9	-2:36:32	24.0	6.4	18.1	9
1040-0038	10:40:57.5	-0:38:11	24.1	4.5	19.0	8
1041-0041	10:41:32.4	-0:41:59	22.9	9.8	16.7	...	7759	...	5
1042+0231	10:42:05.4	+2:31:19	23.7	5.1	18.5	7
1042-0106a	10:42:23.1	-1:06:11	23.4	7.7	17.5	-5
1042+0154	10:42:26.7	+1:54:45	22.6	8.6	17.4	...	8448	9.407	9
1042+0020	10:42:35.1	+0:20:17	21.4	9.6	16.2	0.53	27185	...	10
1042+0214	10:42:47.7	+2:14:54	23.2	6.0	18.0	-5
1042-0242	10:42:54.6	-2:42:06	24.1	6.7	17.9	9
1042-0106b	10:42:55.9	-1:06:50	22.6	5.9	17.2	-5
1043+0221	10:43:14.9	+2:21:10	23.2	7.3	17.9	9
1043+0250	10:43:21.4	+2:50:57	23.4	6.5	18.0	10
1043+0018	10:43:40.9	+0:18:50	21.4	5.4	16.2	...	13966	9.501	9
1043-0227	10:43:55.6	-2:27:16	20.5	5.6	14.9	...	6425	...	3

Table A.1: Continued

Name (1)	RA (2)	Dec (3)	$\mu_B(0)$ (4)	r_{eff} (5)	m_B (6)	$B-V$ (7)	v_{hel} (8)	Log M_H (9)	T (10)
1043+0202	10:43:59.8	+2:02:17	22.7	6.8	17.5	...	1018	7.729	10
1045+0014	10:45:45.9	+0:14:31	21.8	7.4	16.2	...	11644	9.574	5
1047+0131	10:47:34.6	+1:31:47	23.1	7.8	17.4	...	1604	7.936	10
1048+0125	10:48:17.8	+1:25:49	21.7	8.7	15.2	...	11560	9.622	21
1048-0153	10:48:25.3	-1:53:03	19.8	10.9	13.3	0.36	4568	...	1
1050+0245	10:50:28.5	+2:45:34	24.7	11.4	17.4	...	1054	8.180	10
1050+0021	10:50:32.4	+0:21:24	24.4	4.7	19.3	8
1050+0253	10:50:44.0	+2:53:34	21.9	8.7	15.7	...	1037	8.024	10
1051+0201	10:51:09.9	+2:01:22	23.8	3.9	19.1	4
1051+0227	10:51:47.1	+2:27:36	23.5	7.1	17.9	-5
1056-0111	10:56:51.3	-1:11:25	23.8	5.3	18.6	9
1100+0200	11:00:04.3	+2:00:56	23.7	6.0	18.3	5
1101+0211	11:01:45.4	+2:11:24	24.1	10.9	18.2	...	7578	9.168	10
1102+0019	11:02:06.1	+0:19:38	24.1	13.5	17.3	-5
1103-0135	11:03:01.3	-1:35:35	23.7	19.0	16.3	9
1103+0010	11:03:07.3	+0:10:10	23.7	6.8	18.3	...	3360	9.735	10
1103+0007	11:03:12.8	+0:07:59	22.3	6.1	16.9	10
1104-0002	11:04:21.3	-0:02:31	22.4	7.0	17.0	...	9379	9.588	9
1104+0026	11:04:26.6	+0:26:37	23.6	4.6	18.8	9
1104+0038	11:04:34.5	+0:38:06	22.5	6.2	17.5	-5
1105-0240	11:05:30.4	-2:40:59	22.9	8.1	17.3	5
1105-0237	11:05:34.9	-2:37:24	21.8	7.5	16.4	...	10050	...	5
1105-0204	11:05:43.6	-2:04:40	24.0	4.4	19.1	5
1106+0032	11:06:06.2	+0:32:16	21.6	9.0	15.7	0.42	7639	9.686	9
1106+0256	11:06:19.9	+2:56:52	19.8	4.7	15.4	0.54	10757	9.100	21
1106-0200	11:06:30.3	-2:00:52	23.4	6.0	18.2	4
1106+0257	11:06:45.5	+2:57:12	21.1	4.9	16.9	5
1107+0053	11:07:55.4	+0:53:16	24.2	7.9	18.2	10
1108+0128	11:08:16.3	+1:28:49	22.2	7.1	16.5	10
1108+0121	11:08:20.5	+1:21:51	22.1	10.3	15.9	...	993	7.997	10
1108-0003	11:08:23.3	-0:03:27	24.1	5.8	18.8	9
1109-0210	11:09:09.8	-2:10:45	21.2	6.5	15.3	...	5500	...	1
1109-0255	11:09:50.0	-2:55:36	22.2	8.5	16.3	...	7764	...	10
1110-0017	11:10:14.1	-0:17:48	24.8	11.6	17.8	...	8472	9.372	9
1110-0017	11:10:14.1	-0:17:47	25.0	7.5	19.2	10

Table A.1: Continued

Name (1)	RA (2)	Dec (3)	$\mu_B(0)$ (4)	r_{eff} (5)	m_B (6)	$B-V$ (7)	v_{hel} (8)	Log M_H (9)	T (10)
1111-0220	11:11:07.7	-2:20:11	20.3	7.9	14.8	...	8296	...	5
1113+0107	11:13:15.4	+1:07:59	21.4	11.4	16.2	0.61	13444	...	21
1115-0042	11:15:52.0	-0:42:07	24.4	3.7	19.9	8
1116+0053	11:16:15.6	+0:53:34	21.5	5.8	15.9	...	8059	9.565	1
1116+0303	11:16:45.4	+3:03:54	24.0	5.1	18.9	-5
1118+0217	11:18:20.9	+2:17:59	24.1	6.3	19.1	6
1118+0225	11:18:35.0	+2:25:38	24.7	5.3	19.6	8
1119+0241	11:19:11.6	+2:41:43	23.8	21.1	16.6	...	2585	8.749	7
1120-0216	11:20:50.8	-2:16:17	24.2	3.5	19.6	4
1121+0058	11:21:35.2	+0:58:30	21.8	10.1	15.5	...	7784	9.679	5
1121-0135	11:22:00.0	-1:35:04	24.0	4.8	19.1	4
1122+0126	11:22:03.6	+1:26:36	25.1	5.5	19.6	9
1124-0104	11:24:00.4	-1:04:04	24.2	4.0	19.5	4
1124-0043	11:24:38.6	-0:43:09	21.9	12.9	15.2	...	963	8.101	10
1124-0047	11:24:45.2	-0:47:04	24.3	5.1	19.3	7
1125+0255	11:25:42.9	+2:55:46	19.9	9.3	14.1	0.31	6842	9.805	10
1125+0025	11:25:55.7	+0:25:09	23.0	6.2	17.6	...	15042	9.324	-5
1129+0056	11:29:15.5	+0:56:59	24.8	4.3	19.9	5
1129+0013	11:29:24.7	+0:13:32	22.3	8.8	16.3	...	11899	9.993	4
1130-0027	11:30:11.5	-0:27:52	22.1	9.9	16.2	...	6688	9.504	9
1132-0028	11:32:24.0	-0:28:45	22.4	8.6	16.7	...	5783	9.266	10
1132+0249	11:32:30.9	+2:49:40	21.3	12.0	15.3	0.37	5240	9.315	6
1149-0241	11:49:03.6	-2:41:13	23.1	5.1	18.2	4
1150-0058	11:50:18.2	-0:58:57	23.7	3.6	19.2	6
1151+0226	11:51:03.1	+2:26:39	23.6	4.5	18.8	7
1151-0122	11:51:09.0	-1:22:54	21.8	11.7	16.5	...	3402	...	5
1151-0012	11:51:38.3	-0:12:14	23.8	5.4	18.5	5
1151-0202	11:51:51.4	-2:02:25	20.4	15.7	13.8	...	2572	...	4
1153-0226	11:53:27.2	-2:26:35	19.6	9.7	13.2	...	5922	...	21
1154-0215	11:54:33.4	-2:15:14	23.4	4.3	18.6	4
1154+0203	11:54:48.6	+2:03:35	24.5	12.1	17.7	...	1980	8.151	10
1155-0153	11:55:27.3	-1:53:56	20.7	9.9	15.9	...	23512	...	5
1156-0110	11:56:12.4	-1:10:59	21.4	16.5	14.5	...	2882	...	9
1156+0254	11:56:20.4	+2:54:04	23.0	14.2	16.9	...	3233	8.719	5
1156-0218	11:56:36.5	-2:18:45	22.7	23.7	15.3	...	3554	...	4

Table A.1: Continued

Name (1)	RA (2)	Dec (3)	$\mu_B(0)$ (4)	τ_{eff} (5)	m_B (6)	$B-V$ (7)	v_{hel} (8)	Log M_H (9)	T (10)
1156+0142	11:56:50.9	+1:42:44	21.7	7.9	16.0	...	14131	9.766	5
1157-0040	11:57:02.6	-0:40:45	23.9	4.8	19.1	5
1157-0101	11:57:31.8	-1:01:51	23.6	8.9	17.4	-5
1158+0023	11:58:04.3	+0:23:20	24.4	5.4	19.0	10
1158-0101	11:58:37.2	-1:01:01	21.2	16.5	14.1	0.46	1533	8.449	10
1158+0220	11:58:44.6	+2:20:39	23.8	3.9	19.3	5
1159-0055	11:59:06.4	-0:55:32	23.9	11.8	17.8	-5
1159+0027	11:59:09.7	+0:27:43	23.6	6.1	18.9	5
1201-0240	12:01:08.1	-2:40:20	23.7	4.3	18.8	6
1204+0056	12:04:23.4	+0:56:29	24.1	5.7	18.8	9
1205+0058	12:05:30.3	+0:58:33	21.1	5.3	15.9	0.30	5870	8.971	10
1205-0215	12:05:32.3	-2:15:14	22.3	12.1	16.3	0.46	7510	...	5
1206-0214	12:06:27.9	-2:14:38	23.5	4.0	18.8	4
1208-0300	12:08:39.3	-3:00:08	24.1	4.1	19.6	4
1208+0120	12:08:47.6	+1:20:32	20.5	8.0	15.8	0.43	14100	9.720	21
1209+0137	12:09:25.9	+1:37:40	21.1	8.9	15.5	0.60	6272	9.464	4
1209-0019	12:09:29.3	-0:19:41	21.0	7.7	16.0	0.39	10544	9.412	9
1209+0136	12:09:30.1	+1:36:12	24.6	3.8	20.0	5
1209+0305	12:09:52.0	+3:05:18	23.0	13.4	15.4	...	883	7.942	10
1210+0115	12:10:10.2	+1:15:33	23.4	13.0	18.3	10
1210-0226	12:10:14.4	-2:26:47	20.6	6.9	15.5	0.73	11276	...	21
1210+0130	12:10:23.5	+1:30:29	25.3	15.3	18.6	-5
1210+0142	12:10:57.3	+1:42:24	25.4	4.3	20.2	10
1211+0156	12:11:33.1	+1:56:24	23.8	11.4	17.6	10
1211+0226	12:11:57.3	+2:26:40	21.7	14.9	15.7	0.91	22259	10.193	5
1212-0039	12:12:53.1	-0:39:42	22.4	12.2	16.7	0.15	21466	...	5
1213-0218	12:13:10.9	-2:18:48	25.8	4.5	20.3	9
1213+0221	12:13:12.1	+2:21:39	22.0	3.9	17.9	0.35	23252	10.090	4
1213+0127	12:13:30.8	+1:27:30	22.1	6.3	16.2	...	14976	9.756	1
1214-0110	12:14:04.8	-1:10:26	23.0	7.9	16.9	...	1110	...	10
1216-0207	12:16:24.8	-2:07:36	25.7	3.7	20.3	10
1216-0140	12:16:26.1	-1:40:10	25.0	4.9	19.7	9
1216+0029	12:16:52.2	+0:29:33	22.9	10.8	17.0	...	867	7.552	10
1217+0103	12:17:59.9	+1:03:54	22.4	17.1	15.1	...	2056	8.625	9
1221+0001	12:21:08.4	+0:01:10	23.9	8.1	18.4	-5

Table A.1: Continued

Name (1)	RA (2)	Dec (3)	$\mu_B(0)$ (4)	r_{eff} (5)	m_B (6)	$B-V$ (7)	v_{hel} (8)	Log M_H (9)	T (10)
1221-0106	12:21:27.4	-1:06:06	24.7	3.1	20.5	4
1221+0128	12:21:31.4	+1:28:00	22.2	8.3	15.9	...	7982	9.276	9
1221+0020	12:21:56.9	+0:20:52	23.7	10.1	17.6	...	4650	9.164	10
1223-0052	12:23:36.1	-0:52:45	22.5	4.4	17.3	1
1223-0101	12:23:38.0	-1:01:41	22.3	15.7	15.0	...	2137	...	10
1223+0117	12:23:45.6	+1:17:49	22.7	6.2	17.1	...	1473	7.591	9
1223-0058	12:23:48.8	-0:58:34	22.0	12.5	16.2	0.43	2018	8.317	10
1224-0037	12:24:30.7	-0:37:50	22.4	11.2	15.5	...	2229	...	9
1224-0145	12:24:45.4	-1:45:11	24.2	16.7	17.7	9
1225+0152	12:25:12.9	+1:52:32	22.8	26.2	16.3	...	1298	8.669	10
1225+0153	12:25:28.2	+1:53:03	21.9	3.5	17.4	...	22376	...	3
1226+0022	12:26:30.2	+0:22:49	23.1	13.6	16.2	-5
1226-0212	12:26:38.8	-2:12:45	22.3	9.7	17.4	5
1226+0105	12:26:39.2	+1:05:39	20.9	12.9	15.7	0.53	23655	10.261	5
1226+0119	12:26:48.0	+1:19:58	22.2	11.5	15.2	...	6958	9.620	9
1227-0101	12:27:12.4	-1:01:06	22.8	12.1	17.0	10
1227+0254	12:27:40.6	+2:54:03	22.4	14.4	15.2	...	1635	8.356	10
1228+0157	12:28:30.3	+1:57:07	22.5	11.9	15.6	...	1105	7.749	10
1228+0116	12:28:43.1	+1:16:13	25.1	11.1	18.3	...	2289	8.198	10
1230-0015	12:30:34.2	-0:15:28	24.1	25.0	16.5	...	3279	8.656	10
1230-0005	12:30:35.9	-0:05:58	24.4	9.1	18.4	-5
1247+0002	12:47:30.7	+0:02:17	26.4	11.6	19.6	-5
1247+0231	12:47:34.4	+2:31:11	24.4	10.2	17.9	-5
1249+0233	12:49:49.9	+2:33:34	25.0	10.4	19.1	...	6911	8.912	10
1250-0058	12:50:15.1	-0:58:09	25.4	5.5	19.9	-5
1250+0200	12:50:16.0	+2:00:20	24.6	7.7	19.0	-5
1250-0009	12:50:50.0	-0:09:07	23.2	11.5	16.8	0.54	16667	...	21
1250+0212	12:50:50.9	+2:12:09	24.3	9.4	18.4	-5
1251+0218	12:51:19.9	+2:18:14	25.8	11.1	19.4	10
1251+0010	12:51:31.3	+0:10:10	23.9	12.4	17.9	...	688	...	-5
1251+0122	12:51:59.0	+1:22:46	25.5	5.7	20.3	8
1252+0214	12:52:24.4	+2:14:57	25.6	11.3	18.8	10
1252+0230	12:52:52.8	+2:30:06	22.3	9.7	16.9	...	14073	...	5
1254-0015	12:54:01.6	-0:15:27	27.3	8.0	20.4	10
1254+0117	12:54:26.9	+1:17:52	23.8	19.7	17.0	...	4489	9.287	5

Table A.1: Continued

Name (1)	RA (2)	Dec (3)	$\mu_B(0)$ (4)	τ_{eff} (5)	m_B (6)	$B-V$ (7)	v_{hel} (8)	Log M_H (9)	T (10)
1257+0219	12:57:25.0	+2:19:09	22.9	13.1	16.1	...	874	7.606	10
1258+0014	12:58:25.2	+0:14:26	22.7	26.7	14.0	...	1294	...	9
1258-0145	12:58:25.3	-1:45:01	26.3	12.0	19.4	10
1300+0055	13:00:09.9	+0:55:55	22.8	9.5	16.7	...	12176	9.486	5
1300+0228	13:00:21.8	+2:28:14	25.8	11.1	19.3	-5
1300+0144	13:00:42.6	+1:44:12	22.4	7.5	17.0	0.61	12264	9.983	5
1301+0259	13:01:06.0	+2:59:39	21.9	9.7	16.9	...	20516	...	5
1301+0218	13:01:10.9	+2:18:28	24.3	10.7	17.9	-5
1301-0143	13:01:42.1	-1:43:56	25.7	5.6	20.3	6
1303-0125	13:03:07.8	-1:25:38	26.1	4.4	21.1	5
1304+0054	13:04:04.9	+0:54:42	26.5	11.2	19.5	10
1307+0112	13:07:31.2	+1:12:52	24.2	9.7	18.2	...	5842	...	10
1309+0229	13:09:01.4	+2:29:16	25.6	3.9	20.8	7
1309-0035	13:09:19.8	-0:35:35	24.0	5.4	18.6	4
1309+0051	13:09:28.1	+0:51:27	22.9	10.3	16.7	...	5700	9.189	10
1310+0013	13:10:11.1	+0:13:28	22.3	8.5	16.6	6
1310-0019	13:10:31.7	-0:19:46	21.7	9.7	15.9	...	12040	9.839	5
1310+0118	13:10:40.8	+1:18:53	23.7	4.7	19.0	4
1310+0118	13:10:40.8	+1:18:53	25.5	5.1	20.4	5
1315+0029	13:15:35.7	+0:29:07	21.0	12.8	15.3	...	9497	9.943	9
1317+0128	13:17:24.0	+1:28:31	25.1	5.4	19.3	10
1319+0200	13:19:10.4	+2:00:58	24.3	20.0	17.6	21
1320+0147	13:20:59.5	+1:47:45	21.7	11.1	14.6	-5
1321+0137	13:21:07.6	+1:37:19	21.5	6.7	15.9	...	16954	9.644	9
1321+0118	13:21:11.9	+1:18:09	23.4	10.2	16.5	5
1323+0243	13:23:43.1	+2:43:06	24.1	15.8	16.8	...	1137	...	10
1325-0205	13:25:20.2	-2:05:31	23.7	5.1	18.9	5
1325+0232	13:25:39.4	+2:32:17	23.0	12.1	16.3	...	1221	...	10
1325+0109	13:25:41.5	+1:09:25	23.9	4.7	19.0	7
1326+0109	13:26:53.0	+1:09:39	23.3	17.9	16.1	...	3267	8.744	10
1327+0148	13:27:23.0	+1:48:06	22.8	10.7	16.0	...	1049	7.495	10
1327-0141	13:27:42.0	-1:41:26	24.4	5.5	19.0	8
1327-0020	13:27:58.0	-0:20:49	20.0	5.2	14.9	...	15908	...	21
1329+0226	13:29:01.2	+2:26:39	23.2	9.0	17.4	...	1395	...	-5
1329-0106	13:29:52.7	-1:06:48	23.0	12.5	17.0	-5

Table A.1: Continued

Name (1)	RA (2)	Dec (3)	$\mu_B(0)$ (4)	τ_{eff} (5)	m_B (6)	$B-V$ (7)	v_{hel} (8)	Log M_H (9)	T (10)
1330-0046	13:30:31.3	-0:46:47	18.2	8.9	11.7	...	3624	...	3
1331-0002	13:31:41.8	-0:02:01	23.0	10.0	17.2	...	3768	8.513	10
1349-0152	13:49:29.1	-1:52:47	21.6	10.6	15.7	0.40	4625	...	21
1349+0039	13:49:57.5	+0:39:51	20.3	3.9	16.5	...	29156	...	5
1350+0022	13:50:10.8	+0:22:35	20.2	4.3	15.4	...	4605	8.838	9
1350+0230	13:50:59.7	+2:30:20	24.8	11.4	18.5	...	4507	8.620	10
1351-0103	13:51:12.0	-1:03:46	23.1	6.2	17.7	-5
1352-0131	13:52:04.4	-1:31:05	23.7	9.2	18.0	-5
1353+0156	13:53:10.3	+1:56:50	23.3	5.1	18.1	10
1353+0202	13:53:37.7	+2:02:26	23.2	8.3	17.4	...	4738	8.956	10
1353-0153	13:53:58.8	-1:53:05	23.6	3.9	19.0	4
1354-0100	13:54:15.0	-1:00:43	23.5	4.8	18.8	9
1354-0051	13:54:23.9	-0:51:30	23.2	8.5	17.8	5
1356-0258	13:56:49.3	-2:58:02	19.1	6.1	13.3	...	7256	...	21
1357-0017	13:57:09.6	-0:17:00	23.5	10.1	17.7	...	4255	8.741	9
1358-0015	13:58:08.8	-0:15:51	21.0	6.9	15.5	...	3403	...	9
1358-0228	13:58:51.3	-2:28:19	22.4	9.6	15.6	...	9069	...	9
1358+0212	13:58:54.9	+2:12:49	22.8	12.2	16.9	10
1359-0106	13:59:19.6	-1:06:08	24.3	7.9	18.6	10
1400-0018	14:00:46.7	-0:18:34	20.4	7.2	14.2	...	7440	...	1
1401+0205	14:01:01.9	+2:05:50	23.9	5.8	18.9	8
1401+0103	14:01:10.9	+1:03:11	20.8	6.9	15.0	...	12582	...	9
1401+0108	14:01:30.4	+1:08:08	21.1	5.6	15.8	...	12901	9.657	3
1401+0114	14:01:31.8	+1:14:14	21.6	6.0	16.7	...	7482	9.184	9
1404+0226	14:04:48.6	+2:26:50	24.0	4.1	19.1	4
1405+0122	14:05:17.3	+1:22:24	23.5	12.0	17.8	...	14871	9.682	10
1405+0006	14:05:57.8	+0:06:34	20.6	6.2	15.2	...	7518	9.729	3
1407-0100	14:07:21.9	-1:00:15	20.1	5.9	14.6	...	7423	...	3
1408-0023	14:08:25.7	-0:23:46	23.4	4.9	18.5	4
1408+0056	14:08:56.8	+0:56:03	24.0	5.6	18.7	5
1408-0259	14:08:57.3	-2:59:08	18.5	5.2	13.2	...	8904	...	3
1409-0049	14:09:06.4	-0:49:02	23.3	5.8	18.2	5
1409-0020	14:09:44.2	-0:20:06	24.0	8.1	18.2	10
1409+0130	14:09:47.3	+1:30:24	20.5	9.3	14.9	...	7324	...	3
1411-0247	14:11:46.4	-2:47:57	22.8	11.7	16.4	...	1853	...	6

Table A.1: Continued

Name (1)	RA (2)	Dec (3)	$\mu_B(0)$ (4)	r_{eff} (5)	m_B (6)	$B-V$ (7)	v_{hel} (8)	Log M_H (9)	T (10)
1428-0226	14:28:51.6	-2:26:56	23.6	5.8	18.6	7
1429-0146	14:29:08.3	-1:46:18	21.1	7.6	16.1	...	16008	...	5
1430+0215	14:30:34.2	+2:15:21	21.8	6.6	17.4	...	31501	...	5
1430+0214	14:30:39.3	+2:14:39	22.2	6.5	17.6	...	32502	...	5
1430-0049	14:30:46.9	-0:49:56	23.5	6.9	18.2	6
1430+0005	14:30:53.3	+0:05:57	22.3	13.9	16.4	...	10300	...	10
1431+0142	14:31:20.5	+1:42:24	25.8	24.2	17.4	...	1829	8.300	10
1431+0146	14:31:41.8	+1:46:33	23.9	11.6	18.1	...	8584	9.064	9
1431+0149	14:31:48.8	+1:49:32	23.2	8.9	17.7	...	9192	9.306	5
1432+0214	14:32:11.3	+2:14:08	24.5	4.6	19.6	5
1433+0255	14:33:04.8	+2:55:26	24.2	7.9	17.8	10
1433+0249	14:33:18.2	+2:49:23	23.5	15.1	16.8	...	1557	8.033	10
1433+0304	14:33:30.3	+3:04:06	19.1	3.1	15.0	...	8497	...	5
1434+0020	14:34:04.9	+0:20:00	22.9	7.6	17.5	...	9030	...	-5
1434+0155	14:34:44.2	+1:55:25	24.4	4.2	19.6	5
1434-0221	14:34:53.1	-2:21:28	23.8	5.2	18.8	3
1434-0055	14:34:55.3	-0:55:33	23.8	6.8	18.4	-5
1435-0129	14:35:16.3	-1:29:34	25.3	5.1	19.6	10
1435-0118	14:35:29.4	-1:18:23	24.8	4.2	19.9	8
1436+0011	14:36:13.1	+0:11:14	24.3	4.8	19.3	7
1436+0119	14:36:13.4	+1:19:50	21.2	7.5	16.2	...	23686	...	5
1436+0043	14:36:33.8	+0:43:22	22.4	9.1	16.5	...	9932	...	9
1437-0005	14:37:06.6	-0:05:18	23.8	11.8	17.4	...	1939	8.583	9
1437+0001	14:37:25.8	+0:01:38	24.2	7.6	18.5	10
1438-0006	14:38:22.2	-0:06:17	21.5	29.7	13.4	...	1798	...	3
1438+0049	14:38:30.2	+0:49:56	22.4	12.5	17.0	...	2837	8.297	10
1439-0135	14:39:09.2	-1:35:40	23.2	20.0	15.8	...	1654	...	7
1439+0053	14:39:15.4	+0:53:56	22.7	15.2	15.3	...	1891	8.533	7
1440-0008	14:40:11.9	-0:08:21	20.8	9.9	14.7	0.49	1703	8.458	10
1440-0010	14:40:26.3	-0:10:17	23.1	10.4	16.8	...	1744	7.916	10
1440-0104	14:40:41.2	-1:04:21	23.9	5.3	19.0	3
1441+0144	14:41:58.2	+1:44:06	21.3	9.3	15.5	0.60	1474	7.659	4
1442+0137	14:42:27.5	+1:37:06	22.0	6.3	16.5	...	10007	...	5
1442+0026	14:42:51.7	+0:26:38	24.1	5.0	16.7	4
1443+0209	14:43:07.8	+2:09:50	23.8	11.7	18.5	-5

Table A.1: Continued

Name (1)	RA (2)	Dec (3)	$\mu_B(0)$ (4)	r_{eff} (5)	m_B (6)	$B-V$ (7)	v_{hel} (8)	Log M_H (9)	T (10)
1443-0052	14:43:46.1	-0:52:45	22.1	18.9	16.6	...	8459	...	10
1443-0138	14:43:55.8	-1:38:57	24.3	8.8	17.7	10
1443+0058	14:43:58.7	+0:58:07	24.1	5.0	19.1	5
1444-0210	14:44:26.9	-2:10:36	23.5	15.3	17.1	9
1446-0031	14:46:22.2	-0:31:13	22.9	6.9	17.7	...	8415	9.377	5
1446+0231	14:46:27.2	+2:31:15	23.4	6.7	18.0	...	10261	9.635	9
1446+0238	14:46:30.8	+2:38:35	21.8	9.5	16.0	...	10281	9.733	5
1446-0041	14:46:34.9	-0:41:45	22.2	8.2	16.6	...	8325	...	5
1446-0121	14:46:48.4	-1:21:10	23.7	7.1	17.9	10
1449+0100	14:49:43.4	+1:00:30	24.0	3.9	19.4	5
1450+0230	14:50:53.3	+2:30:22	23.9	5.5	18.6	4
1451-0055	14:51:49.2	-0:55:38	23.1	13.8	17.0	10
1452+0121	14:52:10.4	+1:21:51	24.1	9.2	17.8	-5
2247+0036	22:47:49.6	+0:36:50	24.2	14.8	17.5	0.62	17861	...	10
2250+0059	22:50:22.1	+0:59:59	24.1	3.9	19.4	8
2251+0124	22:51:00.3	+1:24:25	23.5	12.2	17.2	0.49	4963	8.899	9
2252+0156	22:52:18.6	+1:56:22	22.7	11.4	16.9	...	7731	9.373	9
2253-0128	22:53:51.5	-1:28:27	23.9	13.2	17.3	10
2254-0158	22:54:09.8	-1:58:24	24.1	4.3	19.4	8
2254-0243	22:54:33.2	-2:43:06	22.4	14.7	15.6	-0.10	2575	...	10
2254-0245	22:54:36.0	-2:45:24	21.8	6.2	16.4	...	4606	...	3
2254-0246	22:54:58.2	-2:46:08	23.1	20.5	15.4	...	2770	...	9
2257+0025	22:57:22.1	+0:25:12	24.2	6.0	18.9	7
2257-0253	22:57:24.5	-2:53:42	24.3	4.7	19.4	5
2300+0137	23:00:48.2	+1:37:01	22.2	11.5	15.5	...	5362	9.258	6
2301-0302	23:01:04.4	-3:02:43	19.3	8.3	14.3	0.85	9284	...	9
2301+0046	23:01:07.6	+0:46:25	21.2	7.8	15.4	...	12198	...	9
2303-0006	23:03:57.8	-0:06:02	20.9	13.7	14.2	0.49	7468	9.711	9
2304+0155	23:04:45.0	+1:55:14	21.3	13.6	14.8	0.33	5244	9.574	5
2309-0122	23:09:46.8	-1:22:01	22.7	13.9	16.5	5
2310-0237	23:10:17.0	-2:37:14	23.6	14.8	16.3	0.50	30414	...	10
2311-0200	23:11:39.0	-2:00:02	20.4	5.3	15.4	...	12352	...	3
2311-0258	23:11:52.1	-2:58:14	21.4	10.1	13.7	...	3413	...	9
2311-0002	23:11:59.4	-0:02:08	20.6	8.2	14.3	...	4392	8.950	1
2312+0107	23:12:16.9	+1:07:02	21.3	6.1	16.0	...	4739	...	3

Table A.1: Continued

Name (1)	RA (2)	Dec (3)	$\mu_B(0)$ (4)	τ_{eff} (5)	m_B (6)	$B-V$ (7)	v_{hel} (8)	Log M_H (9)	T (10)
2312-0011	23:12:27.9	-0:11:58	20.7	5.5	15.6	...	15380	9.977	3
2313+0008	23:13:09.3	+0:08:40	20.8	10.6	14.7	0.61	8667	9.758	3
2314+0230	23:14:05.8	+2:30:06	23.5	5.9	18.2	5
2314-0230	23:14:15.3	-2:30:01	23.9	6.3	18.8	9
2314-0046	23:14:44.8	-0:46:08	23.7	4.6	18.8	5
2315-0003	23:15:33.0	-0:03:10	22.1	4.9	17.1	3
2315-0000	23:15:41.9	-0:00:43	20.8	12.3	15.0	...	8938	9.705	5
2317+0112	23:17:03.8	+1:12:21	21.0	10.1	14.5	...	9046	9.742	3
2317+0056	23:17:18.3	+0:56:39	21.8	8.8	16.4	...	8872	...	5
2317-0037	23:17:33.4	-0:37:24	21.7	9.4	15.7	9
2317-0034	23:17:47.3	-0:34:44	22.4	7.5	16.7	5
2318+0033	23:18:07.6	+0:33:08	23.4	10.8	17.6	6
2318+0214	23:18:16.4	+2:14:21	22.8	13.6	16.4	...	4026	9.130	9
2318+0236	23:18:34.0	+2:36:35	20.5	7.7	15.0	...	3933	9.347	5
2319+0010	23:19:00.5	+0:10:23	22.1	8.4	16.4	5
2319-0057	23:19:17.9	-0:57:52	21.1	9.2	15.0	...	7140	...	3
2319+0112	23:19:31.8	+1:12:23	21.4	7.7	15.6	...	8816	9.728	4
2320+0110	23:20:19.9	+1:10:05	21.0	6.5	15.1	...	8951	9.910	3
2320-0118	23:20:24.3	-1:18:09	23.7	4.5	18.9	5
2320+0107	23:20:26.7	+1:07:55	21.1	5.5	15.7	...	8868	9.839	3
2322-0216	23:22:03.7	-2:16:21	22.0	31.6	14.8	...	5246	...	21
2322-0016	23:22:28.2	-0:16:32	21.6	22.6	14.8	...	10147	9.999	21
2327-0007	23:27:52.0	-0:07:09	21.9	19.4	15.0	0.74	5207	8.985	5
2327-0244	23:27:58.2	-2:44:18	20.0	18.5	14.1	0.71	9521	...	5
2328-0011	23:28:13.3	-0:11:23	23.1	7.0	17.7	4
2328+0004	23:28:34.9	+0:04:14	23.6	3.9	18.9	6
2328+0143	23:28:41.6	+1:43:36	23.3	16.1	16.5	0.41	3642	9.072	5
2329-0204	23:29:06.8	-2:04:36	22.8	13.3	16.7	5
2329+0203	23:29:15.5	+2:03:47	21.6	9.2	15.8	0.50	5176	8.988	5
2329-0225	23:29:19.4	-2:25:56	21.3	14.9	14.6	0.33	2775	...	4
2329+0145	23:29:24.9	+1:45:53	22.2	6.0	17.0	5
2329+0050	23:29:32.4	+0:50:31	23.3	9.1	17.8	-5
2329+0148	23:29:38.2	+1:48:37	22.7	6.2	17.3	-5
2330-0258	23:30:41.6	-2:58:44	20.6	13.7	13.8	...	2158	...	9
2331-0003	23:31:26.8	-0:03:43	22.8	9.9	17.2	9

Table A.1: Continued

Name (1)	RA (2)	Dec (3)	$\mu_B(0)$ (4)	r_{eff} (5)	m_B (6)	$B-V$ (7)	v_{hel} (8)	Log M_H (9)	T (10)
2331+0118	23:31:31.3	+1:18:24	22.9	9.4	16.2	7
2332-0056	23:32:11.1	-0:56:57	22.9	6.2	17.6	-5
2332+0055	23:32:19.8	+0:55:51	24.0	10.9	17.9	10
2332-0014	23:32:40.0	-0:14:03	21.9	16.0	15.5	0.57	5290	9.320	5
2333+0025	23:33:22.7	+0:25:37	22.7	9.9	16.7	9
2333+0017	23:33:28.7	+0:17:26	23.7	5.0	18.8	6
2333+0132	23:33:55.8	+1:32:36	22.5	5.5	17.0	-5
2334+0128	23:34:11.2	+1:28:06	23.9	10.9	17.4	...	7241	9.248	10
2334+0020	23:34:13.3	+0:20:47	22.4	9.0	16.6	9
2334-0235	23:34:32.7	-2:35:22	22.2	8.7	16.4	...	10226	...	6
2334-0157	23:34:40.0	-1:57:34	21.2	13.1	15.0	...	16052	...	5
2335+0101	23:35:13.7	+1:01:23	22.3	10.9	16.3	5
2335-0044	23:35:37.2	-0:44:23	22.1	7.9	16.3	7
2339-0122	23:39:11.5	-1:22:08	23.5	5.2	18.6	5
2339+0237	23:39:28.7	+2:37:43	23.3	3.8	18.7	3
2339-0244	23:39:32.2	-2:44:17	22.2	13.7	16.0	0.38	6699	...	6
2339+0051	23:39:43.4	+0:51:25	24.6	9.4	17.5	-5
2341-0012	23:41:21.5	-0:12:06	24.4	8.6	18.2	7
2341-0010	23:41:48.3	-0:10:53	22.0	10.0	16.0	0.51	6630	9.360	5
2342+0213	23:42:58.0	+2:13:23	23.6	4.0	19.1	6
2343+0025	23:43:49.8	+0:25:46	23.8	5.7	18.8	4
2344+0139	23:44:47.4	+1:39:20	20.6	11.6	14.5	0.58	5234	9.222	5
2345-0247	23:45:17.1	-2:47:34	23.4	4.2	18.7	4
2347+0136	23:47:35.8	+1:36:45	23.9	5.5	18.8	5
2348+0044	23:48:28.8	+0:44:26	23.5	5.2	18.4	4
2349+0248	23:49:17.0	+2:48:14	20.6	15.6	14.3	0.45	5324	9.793	4
2349+0028	23:49:19.1	+0:28:34	21.8	20.9	15.9	...	11279	9.590	21
2351+0212	23:51:01.9	+2:12:43	23.7	5.0	18.6	10

REFERENCES

- Aaronson, M., Bothun, G., Mould, J., Huchra, J., Schommer, R. A., & Cornell, M. E. 1986, *ApJ*, 302, 536
- Aaronson, M., Huchra, J., & Mould, J. 1979, *ApJ*, 229, 1
- Aaronson, M. & Mould, J. 1983, *ApJ*, 265, 1
- Allen, R. J. & Shu, F. H. 1979, *ApJ*, 227, 67
- Arp, H. C. 1965, *ApJ*, 145, 402
- Arp, H. C. 1966, *ApJS*, 14, 1
- Bernstein, G. M., Guhathakurta, P., Raychaudhury, S., Giovanelli, R., Haynes, M. P., Herter, T., & Vogt, N. P. 1994, *AJ*, 107, 1962
- Binggeli, B., Sandage, A., & Tammann, G. A. 1985, *AJ*, 90, 1681
- Binggeli, B., Sandage, A., & Tammann, G. A. 1988, *ARA&A*, 26, 509
- Binggeli, B., Tarenghi, M., & Sandage, A. 1990, *A&A*, 228, 42
- Blair, M. & Gilmore, G. 1982, *PASP*, 94, 742
- Boroson, T. A. 1980, Ph.D. thesis, Univ. of Arizona
- Bosma, A. & Freeman, K. C. 1993, *AJ*, 106, 1394
- Bothun, G. D. 1982, *ApJS*, 50, 39
- Bothun, G. D., Aaronson, M., Schommer, B., Mould, J., Huchra, J., & Sullivan III, W. T. 1985a, *ApJS*, 57, 423
- Bothun, G. D., Beers, T. C., Mould, J. R., & Huchra, J. P. 1985b, *AJ*, 90, 2487
- Bothun, G. D., Beers, T. C., Mould, J. R., & Huchra, J. P. 1986, *ApJ*, 308, 510
- Bothun, G. D., Heckman, T. M., Schommer, R. A., & Balick, B. 1984, *AJ*, 89, 1293

- Bothun, G. D., Impey, C. D., & Malin, D. F. 1991, *ApJ*, 376, 404
- Bothun, G. D., Impey, C. D., Malin, D. F., & Mould, J. R. 1987, *AJ*, 94, 23
- Bothun, G. D. & Mould, J. R. 1987, *ApJ*, 313, 629
- Bothun, G. D., Schombert, J. M., Impey, C. D., & Schneider, S. E. 1990, *ApJ*, 360, 427
- Bothun, G. D., Schombert, J. M., Impey, C. D., Sprayberry, D., & McGaugh, S. S. 1993, *AJ*, 106, 530
- Broadhurst, T. J., Ellis, R. S., & Shanks, T. 1988, *MNRAS*, 235, 827
- Burstein, D., Faber, S. M., Gaskell, C. M., & Krumm, N. 1984, *ApJ*, 287, 586
- Burstein, D. & Heiles, C. 1982, *AJ*, 87, 1165
- Buta, R. 1990, in *Morphology and Physical Classification of Galaxies*, ed. G. Longo, M. Capaccioli, & G. Busarello (Dordrecht: Kluwer), 1
- Cawson, M. G. M., Kibblewhite, E. J., Disney, M. J., & Phillipps, S. 1987, *MNRAS*, 224, 557
- Cellone, S. A., Forte, J. C., & Geisler, D. 1994, *ApJS*, 93, 397
- Christian, C. A., Adams, M., Barnes, J. V., Butcher, H., Hayes, D. S., Mould, J. R., & Siegel, M. 1985, *PASP*, 97, 363
- Coleman, G. D., Wu, C.-C., & Weedman, D. W. 1980, *ApJS*, 43, 393
- Colless, M., Ellis, R. S., Taylor, K., & Hook, R. N. 1990, *MNRAS*, 244, 408
- Davies, J. I. 1993, in *The Environment and Evolution of Galaxies*, ed. J. M. Shull & H. A. Thronson, Jr. (Dordrecht: Kluwer), 105
- Davies, J. I., Disney, M. J., Phillipps, S., Boyle, B. J., & Couch, W. J. 1994, *MNRAS*, 269, 349

- Davies, J. I., Phillipps, S., & Disney, M. J. 1988, MNRAS, 231, 69p
- Davies, J. I., Phillipps, S., & Disney, M. J. 1990, MNRAS, 244, 385
- Davis, M. & Huchra, J. 1982, ApJ, 254, 437
- de Jong, R. S. & van der Kruit, P. C. 1994, A&AS, 106, 451
- de Vaucouleurs, G. 1959, in Handbuch der Physik, Astrophysics IV. Stellar Systems, ed. S. Flügge (Berlin: Springer-Verlag), 275
- de Vaucouleurs, G., de Vaucouleurs, A., & Corwin, Jr., H. G. 1976, Second Reference Catalog of Bright Galaxies, (Austin, Texas: University of Texas)
- Dekel, A. & Silk, J. 1986, ApJ, 303, 39
- Disney, M. & Phillipps, S. 1983, MNRAS, 205, 1253
- Disney, M. J. 1976, Nature, 263, 573
- Disney, M. J. 1980, in ESO/ESA Workshop on Dwarf Galaxies, ed. M. Tarenghi & K. Kjar (Geneva: ESO/ESA), 151
- Djorgovski, S., De Carvalho, R., & Han, M.-S. 1988, in ASP Conf. Ser. No. 4, The Extragalactic Distance Scale: Proceedings of the ASP 100th Anniversary Symposium, ed. S. van den Bergh & C. J. Pritchet (San Francisco: ASP), 329
- Efstathiou, G., Bernstein, G., Katz, N., Tyson, J. A., & Guhathakurta, P. 1991, ApJ, 380, L47
- Efstathiou, G., Ellis, R. S., & Peterson, B. A. 1988, MNRAS, 232, 431 (EEP)
- Felten, J. E. 1976, ApJ, 207, 700
- Ferguson, H. C. & Sandage, A. 1988, AJ, 96, 1520
- Fish, R. A. 1964, ApJ, 139, 284

- Fisher, J. R. & Tully, R. B. 1981, *ApJS*, 47, 139
- Freeman, K. C. 1970, *ApJ*, 160, 811
- Fukugita, M., Okamura, S., Tarusawa, K., Rood, H. J., & Williams, B. A. 1991, *ApJ*, 376, 8
- Giovanelli, R., Haynes, M. P., Salzer, J. J., Wegner, G., Da Costa, L. N., & Freudling, W. 1994, *AJ*, 107, 2036
- Haynes, M. P. & Giovanelli, R. 1984, *AJ*, 89, 758
- Heckman, T. M., Balick, B., & Sullivan III, W. T. 1978, *ApJ*, 224, 745
- Hoffman, Y., Silk, J., & Wyse, R. F. G. 1992, *ApJ*, 388, L13
- Holmberg, E. 1958, *Med. Lunds Astron. Obs.*, II, No. 136
- Hubble, E. 1925, *ApJ*, 62, 409
- Hubble, E. 1926, *ApJ*, 63, 236
- Huchra, J. & Brodie, J. 1987, *AJ*, 93, 779
- Impey, C. & Bothun, G. 1989, *ApJ*, 341, 89
- Impey, C., Bothun, G., & Malin, D. 1988, *ApJ*, 330, 634
- Impey, C. D., Irwin, M. J., Sprayberry, D., & Bothun, G. D. 1995, *ApJ*, (in preparation)
- Irwin, M. J., Davies, J. I., Disney, M. J., & Phillipps, S. 1990, *MNRAS*, 245, 289
- Kennicutt, R. 1989, *ApJ*, 344, 685
- Kent, S. M. 1984, *ApJS*, 56, 105
- Kent, S. M. 1985, *ApJS*, 59, 115
- Kent, S. M. 1986, *AJ*, 91, 1301

- Kent, S. M. 1987, *AJ*, 93, 816
- Kibblewhite, E. J., Bridgeland, M. T., Bunclark, P. S., & Irwin, M. J. 1984, in NASA Conf. Pub. No. 2317, *Astronomical Microdensitometry Conference*, ed. D. A. Klinglesmith (Washington, D. C.: NASA), 277
- Knezek, P. M. 1993, Ph.D. thesis, Univ. of Massachusetts
- Koo, D. C., Gronwall, C., & Bruzual A., G. 1993, *ApJ*, 415, 21L
- Lacey, C., Guiderdoni, B., Rocca-Volmerange, B., & Silk, J. 1993, *ApJ*, 402, 15
- Lacey, C. & Silk, J. 1991, *ApJ*, 381, 14
- Landolt, A. U. 1992, *AJ*, 104, 340
- Lauer, T. R. & Postman, M. 1994, *ApJ*, 425, 418
- Lilly, S. J., Cowie, L. L., & Gardner, J. P. 1991, *ApJ*, 369, 79
- Longair, M. S. 1978, in *Observational Cosmology: Eighth Advanced Course of the Swiss Society of Astronomy and Astrophysics* (Sauverny, Switzerland: Geneva Observatory), 125
- Longmore, A. J., Hawarden, T. G., Goss, W. M., Mebold, U., & Webster, B. L. 1982, *MNRAS*, 200, 325
- Loveday, J., Peterson, B. A., Efstathiou, G., & Maddox, S. J. 1992, *ApJ*, 390, 338
- Marzke, R. O., Geller, M. J., Huchra, J. P., & Corwin, Jr., H. G. 1994a, *AJ*, 108, 437
- Marzke, R. O., Huchra, J. P., & Geller, M. J. 1994b, *ApJ*, 428, 43
- Massey, P., Strobel, K., Barnes, J. V., & Anderson, E. 1988, *ApJ*, 328, 315
- McGaugh, S. S. 1994, *Nature*, 367, 538
- McGaugh, S. S. & Bothun, G. D. 1994, *AJ*, 107, 530

- McLeod, B. A. 1994, Ph.D. thesis, Univ. of Arizona
- Meurs, E. J. A. & Wilson, A. S. 1984, *A&A*, 136, 206
- Mo, H., McGaugh, S. S., & Bothun, G. D. 1994, *MNRAS*, 267, 129
- Morris, S. L., Weymann, R. J., Dressler, A., McCarthy, P. J., Smith, B. A., Terile,
R. J., Giovanelli, R., & Irwin, M. 1993, *ApJ*, 419, 524
- Mould, J. 1978, *ApJ*, 220, 434
- Mould, J., Han, M.-S., & Bothun, G. 1989, *ApJ*, 347, 112
- Nilson, P. N. 1973, *Uppsala General Catalog of Galaxies*, (Uppsala, Finland:
Uppsala Astronomical Observatory)
- Odewahn, S. C., Bryja, C., & Humphreys, R. M. 1992, *PASP*, 104, 553
- Osterbrock, D. E. 1977, *ApJ*, 215, 733
- Pierce, M. J. & Tully, R. B. 1988, *ApJ*, 330, 579
- Pierce, M. J. & Tully, R. B. 1992, *ApJ*, 387, 47
- Press, W. P. & Schechter, P. 1974, *ApJ*, 187, 425
- Quirk, W. 1972, *ApJ*, 176, L9
- Rao, S. & Briggs, F. 1993, *ApJ*, 419, 515
- Rix, H.-W. R. 1991, Ph.D. thesis, Univ. of Arizona
- Roberts, M. S. 1975, in *Stars and Stellar Systems* (Chicago: Univ. of Chicago Press),
309
- Roberts, M. S. & Haynes, M. P. 1994, *ARA&A*, 32, 115
- Romanishin, W., Krumm, N., Salpeter, E., Knapp, G., Strom, K. M., & Strom,
S. E. 1982, *ApJ*, 263, 94
- Romanishin, W., Strom, K. M., & Strom, S. E. 1983, *ApJS*, 53, 105

- Rubin, V. C., Whitmore, B. C., & Ford, Jr., W. K. 1988, *ApJ*, 333, 522
- Sandage, A., Tammann, G. A., & Yahil, A. 1979, *ApJ*, 232, 352 (STY)
- Schechter, P. 1976, *ApJ*, 203, 297
- Schmidt, M. 1968, *ApJ*, 151, 393
- Schombert, J. M. & Bothun, G. D. 1988, *AJ*, 95, 1389
- Schombert, J. M., Bothun, G. D., Impey, C. D., & Mundy, L. G. 1990, *AJ*, 100, 1523
- Schombert, J. M., Bothun, G. D., Schneider, S. E., & McGaugh, S. S. 1992, *AJ*, 103, 1107
- Sprayberry, D., Impey, C. D., Irwin, M. J., McMahon, R. G., & Bothun, G. D. 1993, *ApJ*, 417, 114
- Steidel, C. C. & Dickinson, M. 1994, in *Proceedings of the 35th Herstmonceux Conference, Wide Field Spectroscopy and the Distant Universe*, ed. S. J. Maddox & A. Aragón-Salamanca (Singapore: World Scientific), in press
- Szomoru, A., Guhathakurta, P., van Gorkum, J. H., Knapen, J. H., Weinberg, D. H., & Fruchter, A. S. 1994, *AJ*, 108, 491
- Talbot, R. J., J. & Arnett, W. D. 1975, *ApJ*, 197, 551
- Tully, R. B. & Fisher, J. R. 1977, *A&A*, 54, 661
- Tully, R. B. & Fouqué, P. 1985, *ApJS*, 58, 67
- Tyson, J. A. 1988, *AJ*, 96, 1
- van der Hulst, J. M., Skillman, E. D., Smith, T. R., Bothun, G. D., McGaugh, S. S., & de Blok, W. J. G. 1993, *AJ*, 106, 548
- van der Kruit, P. C. 1987, *A&A*, 173, 59

- Weir, S., Djorgovski, S., Fayyad, U., Doyle, R., & Roden, J. 1992, in ASP Conf. Ser. No. 43, *Sky Surveys: Protostars to Protogalaxies*, ed. B. T. Soifer (San Francisco: ASP), 135
- Whitmore, B. C., Forbes, D. A., & Rubin, V. C. 1988, *ApJ*, 333, 542
- Yoshii, Y. 1993, *ApJ*, 403, 552
- Zaritsky, D. & Lorrimer, S. 1993, in NASA Conf. Pub. No. 3190, *The Evolution of Galaxies and Their Environment*, ed. D. Hollenbach, H. Thronson, & J. M. Shull (Moffet Field, CA: NASA Ames Research Center), 82
- Zucca, E., Pozzetti, L., & Zamorani, G. 1994, *MNRAS*, 269, 953